An Analysis of Large Pulse Events in Sudbury Neutrino Observatory Photo-multiplier Tubes

by

Edward P. Korpach

A thesis submitted to the Department of Physics
in conformity with the requirements for
the degree of Master of Science

Queen's University
Kingston, Ontario, Canada
September, 1999

To my parents,

Peter and Theresa.

Abstract

The Sudbury Neutrino Observatory is a Cerenkov neutrino detector that uses 1000 tonnes of heavy water to measure the solar neutrino energy spectrum. Surrounding the D_2O are nearly 10,000 photo-multiplier tubes that are used to detect the Cerenkov radiation produced by electrons emitted from neutrino interactions.

It has previously been proposed to use the PMT pulse height in order to identify $\beta\gamma$ decays occurring inside the PMT glass. An analysis of the current PMT pulse height calibration is presented here along with an alternate calibration method. The pulse height distribution of events in the SNO detector was examined as a method of identifying charged particles in the PMT glass in data before the detector was filled with water and has been compared to Monte Carlo simulations. It has been found that the simulations were unable to recreate the number of large pulse events in the data, at an excess rate of approximately 36 Hz per tube. Finally the data has been compared to similar measurements of the PMT pulse height spectrum after the detector had been filled with water. There were many fewer large pulse height events after water-fill compared to air-fill, an equivalent drop in rate of 36 Hz per PMT.

Acknowledgements

I would like to thank the following people without whose support, I would not have been able to complete this thesis.

First I would like to thank my parents, Peter and Theresa, and my sisters, Carolyn and Lisa. Their support and help throughout the years have been invaluable.

I would especially like to thank my supervisor, Barry Robertson. His guidance through the research, writing and editing was essential and much appreciated. I would also like to thank Aksel Hallin, Peter Skensved and Fraser Duncan for their informative discussions throughout the past two years.

Finally I would like to thank all the people who helped, supported, guided or simply made my time at Queen's much more enjoyable; Lorne, Annie, Mark, Chris, Andre, Bryce, Richard, Matt, Kats, and Andrea.

Contents

List of Tables

List of Figures

List of Acronyms

ADC	Analog to Digital Converter
AECL	Atomic Energy Canada Limited
AV	Acrylic Vessel
ECA	Electronics Calibration
Esum	Sum of all analog PMT pulses
FEC	Front End Card
g/g	grams per gram of
GT	Global Trigger
GTID	Global Trigger Identification Number
ND	Neutral Density
Nhit	Number of Hits (PMTs that fired)
PCA	PMT Calibration
pe	Photo-electrons
PGT	Pulsed Global Trigger
PMT	Photo-multiplier Tube
PMTic	PMT Interface Card
Qhl	High gain long integrate charge measurement

Qhs	High gain short integrate charge measurement
Qlx	Low gain long integrate charge measurement
PSUP	PMT Support Structure
SNO	Sudbury Neutrino Observatory
SNODB	SNO Database
SNOMAN	SNO Monte Carlo and Analysis Program
SNP	Solar Neutrino Problem
WIMP	Weakly Interacting Massive Particle

1 Introduction

The Sudbury Neutrino Observatory is a heavy water Cerenkov detector built more than 2 km below the surface of the earth. The main function of this detector is to measure the energy spectrum of ^8B neutrinos from the sun. Several other neutrino experiments have found that the number of neutrinos detected from the sun to be much less than the number predicted by calculation. The standard model predicts that all neutrinos produced in the sun are of the electron neutrino type, ν_e, and previous experiments have primarily been sensitive only to the ν_e. Theories have been suggested to explain the deficit of observed neutrinos, one of which is that neutrinos oscillate from one type to another. SNO will be the first experiment to be sensitive to both the electron neutrino flux as well as the total solar neutrino flux allowing a direct comparison between the two.

The detector contains 1000 tonnes of heavy water located in a spherical acrylic vessel. Surrounding the heavy water is an array of nearly 10,000 photo-multiplier tubes (PMTs) that detect interactions between the neutrinos and the D_2O. The results of the interactions are relativistic electrons that produce Cerenkov radiation as they travel through the water. The timing, position and number of photons detected by the array of photo-multipliers surrounding the D_2O give information on position, energy, and direction of the electron. From this a spectrum of the flux of solar neutrinos will be measured.

Due to the low interaction rate of neutrinos in the detector, expected to be only $\sim$10 per day, one of the largest concerns is backgrounds. Radioactive decays that produce γ rays, β particles or neutrons can imitate a neutrino interaction with the deuterium and even a few of these events per day is enough to provide a significant background to the neutrino signal. The detector has been made out of materials specially selected and manufactured to have extremely low quantities of radioactive elements. As well, several meters of ultra pure light water shield the detector from radiation produced in the cavity wall and other materials in the detector that may be sources of even small amounts of radiation.

The photo-multiplier tubes contain glass made under strict clean conditions. Still, with a low concentration of only $3 \cdot 10^{-8}$ g of Uranium and Thorium per gram of glass, this is relatively high when compared to other materials in the detector such as the D_2O itself which is expected to have less than 10^{-14} g/g of U & Th. The PMTs are separated from the D_2O volume by 2.5 m of light water to shield from radiation originating from the PMTs and other construction materials. Calculations of the energy and range of the radiation emitted from the PMTs have been made and it is not expected to be a significant background for the range of neutrino energy that will be detected. However, experimental verification has not yet been done. If the energy spectrum of these radioactive decays has even a small tail above the energy threshold of observed neutrinos it could affect the neutrino signal.

One concern is that the γ ray produced inside the glass can exit the PMT and travel towards the D_2O. If the γ ray is simultaneously detected with energy above the threshold and reconstructed as having occurred inside the D_2O volume the event will appear to be a neutrino interaction. Or if the γ ray reaches the D_2O volume, an interaction with the deuteron may occur which is indistinguishable from a neutrino interaction. However the β particle emitted in the decay produces Cerenkov radiation inside the PMT glass. Due to the number of Cerenkov photons produced relatively close to the photo-cathode of the PMT in which the decay occurred, a large pulse may be produced - much larger than from almost any neutrino interaction in the D_2O. Events containing a single PMT with a large pulse may be useful as a way of identifying PMT $\beta\gamma$ events.

In chapters two and three a general overview of neutrino theory is supplied followed by a description of the Sudbury Neutrino Observatory Detector. Proper charge calibration is essential for using the charge as a method of identifying PMT $\beta\gamma$ events. An analysis of the current method of charge calibration is reviewed in chapter 4 and in chapter 5 an alternate method is proposed. In chapter 6 particles, such as β particles in the PMT glass or Compton scattered electrons from γ ray interactions with the glass, expected to produce large PMT pulses are analyzed. This is then compared to similar measurements after the detector had been filled with water and the rock wall γ rays had been shielded from the PMTs.

2 Solar Neutrinos

2.1 Neutrinos

For many years it has been known that a class of radioactive decays consist of a nucleus emitting a particle with the charge and mass of an electron. However the emitted particle and the energy left in the nucleus does not conserve energy and momentum. This led Wolfgang Pauli in 1931 to propose that this "β" decay is actually a three body process, with the third particle carrying away the missing energy. The third particle in the decay, named the "little neutral one," or neutrino (ν), was believed to have little or no mass and was very hard to detect. It was not until 1953 that neutrinos were first detected [1]. Using a liquid scintillator and a flux of anti-neutrinos ($\overline{\nu}$) from a nuclear detector, the $\overline{\nu}$ interacted with a proton creating a neutron and positron which were subsequently detected, proving that neutrinos did exist.

Since then three families of leptons - electron, muon, and tauon, have been identified each having a charged particle and a corresponding neutrally charged neutrino:

$$\begin{pmatrix} e \\ \nu_e \end{pmatrix} \quad \begin{pmatrix} \mu \\ \nu_\mu \end{pmatrix} \quad \begin{pmatrix} \tau \\ \nu_\tau \end{pmatrix}$$

as well as corresponding anti-particles.

Sources of Neutrinos

Neutrinos are only created during interactions governed by the weak nuclear force. The two most common examples of this are by proton decay to a neutron (bound in a nucleus), or a neutron decay to a proton (bound or unbound).

For example, in a nucleus of an atom this process, known as β decay, may occur. A nucleon in a heavy nucleus goes through one of two following processes:

$$\begin{aligned} n &\rightarrow p^+ + e^- + \overline{\nu_e} \\ p^+ &\rightarrow n + e^+ + \nu_e \end{aligned}$$

which decreases the number of neutrons by one and increases the number of protons in the nucleus (or vice versa for the second type of decay). The β particle (e^- or e^+) and neutrino are emitted from the nucleus with most of the energy released in the reaction. The β can be detected and has a continuous energy spectrum from zero to the total energy released. Since the ν interacts only through the weak nuclear force it is rarely detected.

Another common example is fusion. In a general case two protons fuse together into deuteron (d^+):

$$p^+ + p^+ \rightarrow d^+ + e^+ + \nu_e$$

and since this is the starting point of fusion in the sun it will be discussed in more detail in the next section.

Although there are many other reactions which emit neutrinos, these are the two reactions are the the most relevant examples for this thesis. The latter describes the method in which solar neutrinos are produced, and the former is the channel in which PMT $\beta\gamma$'s are created.

2.2 Solar Neutrinos

There is a chain of fusion reactions that elements go through inside the sun in which light elements under high gravitational pressure are fused into heavier particles (figure 2.1). Many of these fusion processes include the release of a ν, all of them of the electron family, or "electron flavour". Also it can be seen from the chain shown that none of the processes release an anti-neutrino, $\overline{\nu_e}$. The energy spectra in figure 2.2 shows the energy of neutrinos produced in the sun, which ranges from 0 to 18.77 MeV.

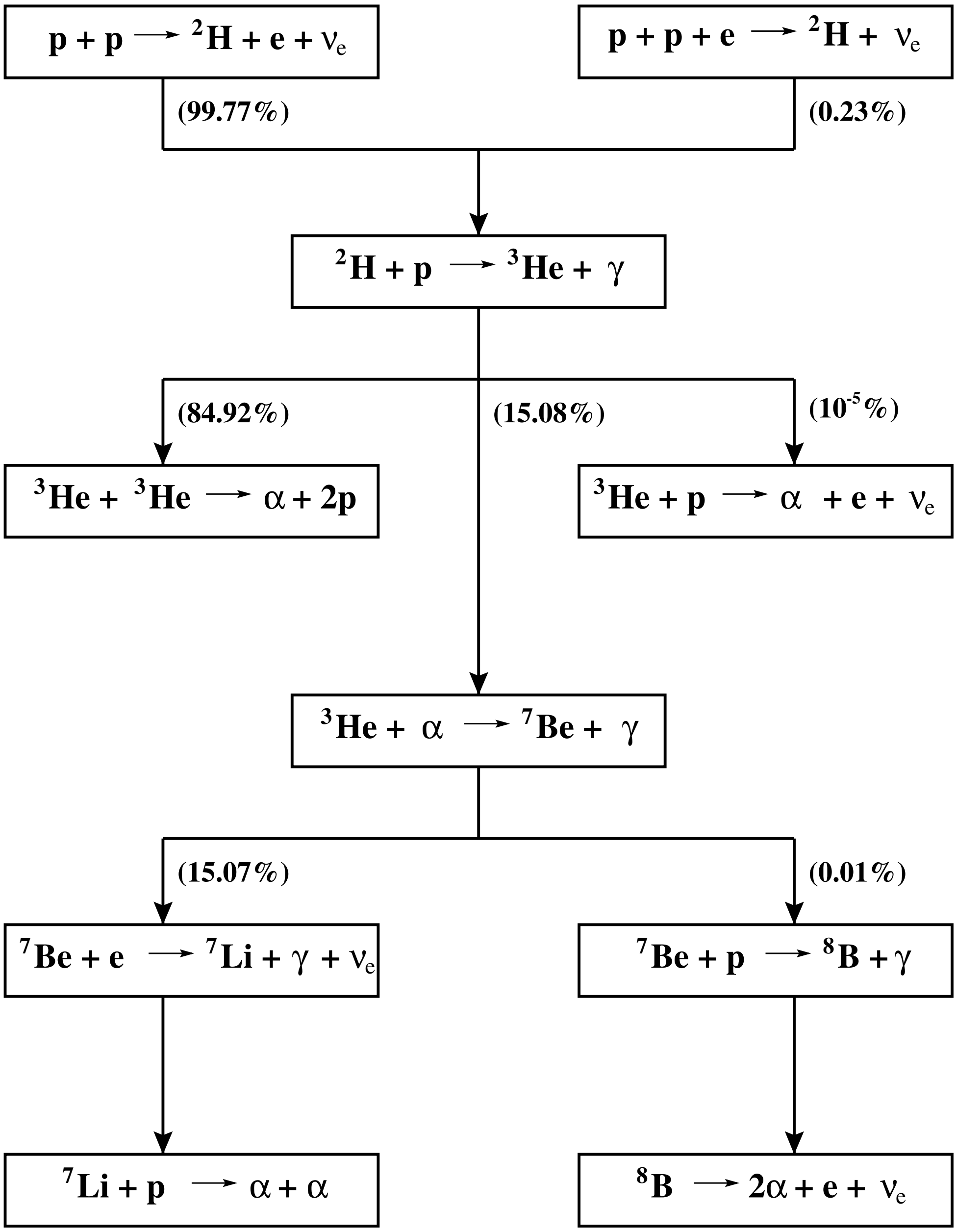

Figure 2.1: pp chain of solar neutrino production. Branching ratios from [2].

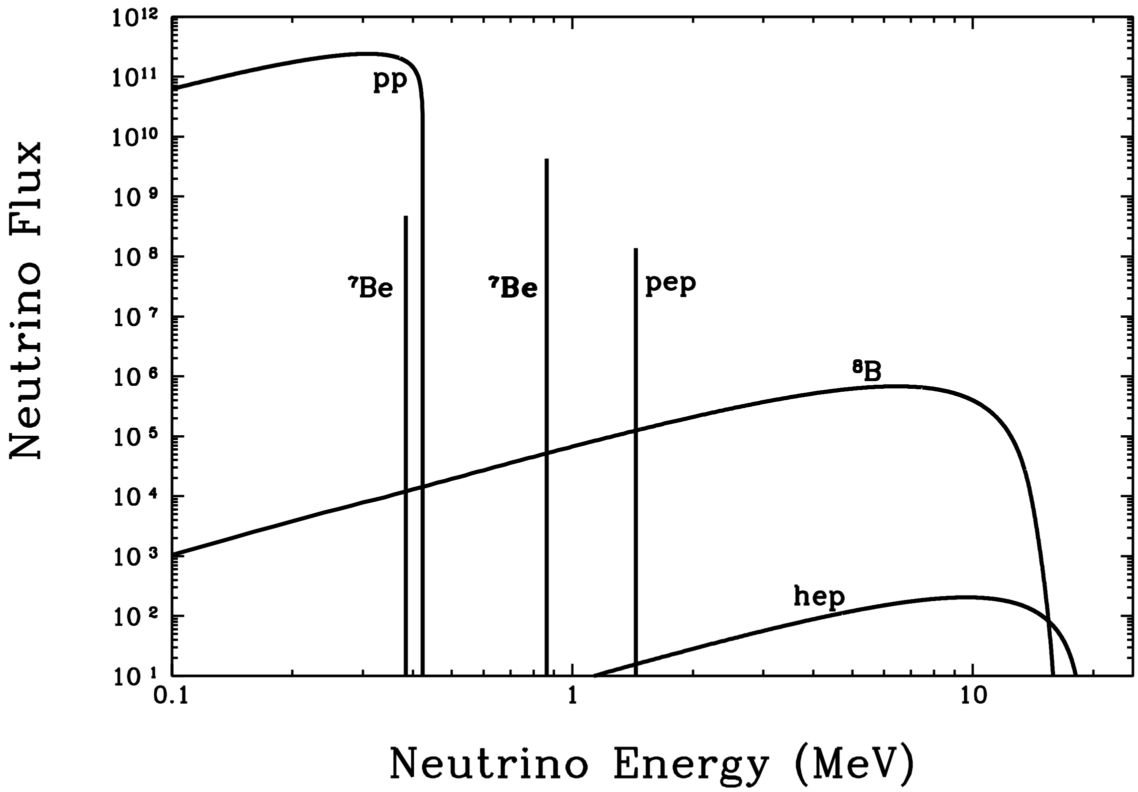

Figure 2.2: Standard solar model prediction of energy spectrum for the pp chain shown in figure 2.1. Units from continuum sources are in $cm^{-2}s^{-1}MeV^{-1}$ at one astronomical unit. Line fluxes are in $cm^{-2}s^{-1}$. [3]

Solar Neutrino Problem

Several neutrino experiments have attempted to measure the ν_e flux from the sun. The range of ν energy sampled has varied but in each case the flux seen by the detectors has been lower than theoretical calculations by a factor of about 2 to 3 [2]. This has led to what is called the Solar Neutrino Problem (SNP).

Using measurements such as the sun's luminosity and temperature at the surface of the sun a set of calculations have been made to predict the solar neutrino flux. The ability to measure this flux by earth-based neutrino observatories and compare it to theory relies on two things. The first is that the measurements made from the properties at the surface of the sun can accurately describe the types and magnitude of nuclear processes occurring throughout the sun. Any incorrect assumptions may lead to errors in predicting the flux of neutrinos originating from inside the sun. The second is that we correctly understand the particle properties of neutrinos, how they interact with matter and how they evolve as they travel through space and time to reach the earth-based observatories.

Nonstandard Solar Model

The low values of the measured neutrino flux by the various experiments has lead to the proposal of two possible solutions to explain the discrepancies. One is that the standard solar model is incorrect. The fusion rates in the sun are directly calculated using observations of the surface of the sun such as radius, mass, temperature, surface chemical composition and photon luminosity. From these measurements calculations of particle interactions inside the sun have been made which in turn produce the expected neutrino flux and energy spectrum. In order to change the solar model to explain the SNP the processes in which neutrinos are created must be decreased without changing the observables at the surface of the sun.

There have been several attempts to create non-standard solar models with varying success. Some nonstandard models suggest changes to the basic constants. For example a suggested solution to the SNP is that the interior temperature of the sun is lower than has been calculated, therefore a lower than expected fusion rate. In order for the luminosity from the sun to be what we observe at this lower internal temperature there must be a smaller concentration of heavy elements in the core of the sun which would mean a lower opacity than has been calculated. This would explain the lower neutrino flux while the surface luminosity and temperature would remain constant. Other theories include such possibilities as the existence of weakly interacting massive particles (WIMPs) in the core that can export energy from the interior to the surface of the sun. Similar to the above theory, the neutrino production rate would then be lower because of a cooler than expected core while still maintaining the luminosity we currently see on the surface of the sun since more of the energy created inside is able to reach the surface. [4]

However, to date there has not been any variation of the standard solar model that has been able to explain the discrepancies from all the solar neutrino observatories while maintaining all observables.

Neutrino Oscillations

The previous section discussed how the predicted flux of neutrinos may be incorrect. The other explanation for the SNP is that our understanding of the properties of neutrinos, how they evolve in time and how they interact with other particles, is incorrect or incomplete.

The popular hypothesis is that the neutrino is able to change from one flavour to another. The sun only produces electron neutrinos but there is a possibility that the neutrino can change to another flavour during the flight from the sun to the earth. Although this is theoretically possible, it may only occur if the neutrino has mass. Currently there is no proof that the neutrino has mass, previous experiments have only been able to set an upper limit on the neutrino mass - perhaps as little as a few eV for the electron neutrino [5]. If it can be demonstrated that $\nu_e s$ are changing flavour between the earth and the sun, it would be proof that they are not massless particles.

If one assumes that when the neutrino leaves the sun the neutrino is of the electron flavor, in the vacuum of space the probability that the neutrino remains an ν_e [4] is

$$P_{\nu_e} \;=\; 1 \;-\; sin^2(2\theta_V)sin^2\left(\frac{\pi R}{L_V}\right) \tag{2.1}$$

where θ_V is a constant called the mixing angle and must be found by direct observations. R is the distance the neutrino has traveled between its origin and the detector. $L_V \;=\; 4\pi E/\Delta m^2$ where E is the neutrino energy. Called the mass squared difference, $\Delta m^2 \;=\; |m_1^2 - m_2^2|$, where m_1 is the mass of the original neutrino and m_2 is the mass of the neutrino into which it oscillates. For solar neutrinos this other neutrino can either be a ν_μ, a ν_τ, or represented as a linear combination of the two. In the case that all the neutrinos are massless or the mixing angle between the neutrino types is zero oscillations can not occur.

An effect on neutrino oscillations, called the MSW or matter oscillations, occurs when the neutrino travels through a medium with electrons. Charged current reactions between electrons and ν_e's introduce a correction term into the mass eigenstate matrix which is dependent on the density of electrons in the medium through which the ν_e travels. The result is an effective increase of the mass of the ν_e. Since this is not a constant, but a variable that depends on the density of electrons in the media, this correction term changes as the neutrino moves from the dense interior to the relatively lower density near the surface of the sun.

There is a density of electrons where oscillations are at a maximum. This resonance occurs when the mass matrix of the electron neutrino matches that of another type of neutrino. The resonance density at which the match occurs depends on Δm^2 and θ_V as well as the energy of the neutrino. If the neutrino passes through a portion of the sun that is a resonance density the probability of oscillation is at a maximum. The result is that a significant fraction of the flux of electron neutrinos started near the centre of the sun may oscillate to another flavour before they even reach the surface of the sun.

Either of these scenarios, vacuum or matter oscillations, could potentially explain the lack of detectable ν_e from the sun since most of the experiments have only been sensitive to detecting this flavour of neutrino.

2.3 Neutrino Detection

There are three main sources of neutrinos that have been used in detection experiments - man made, atmospheric, and solar. Man-made sources, such as nuclear reactors, have been used but the flux of neutrinos can be relatively low. Atmospheric neutrinos created by cosmic rays interacting in the atmosphere are useful due to the relatively high attainable energies. The incident flux of this type of neutrino source is also rather low.

The solar neutrinos have a lower energy than the atmospheric neutrinos but the flux is orders of magnitude higher. Since SNO's main function is as a solar neutrino detector (although atmospheric neutrinos will also be detected but at a much lower rate) this discussion will be limited to detecting solar neutrinos.

Neutrino interaction with other particles is governed only by the weak nuclear force. In an interaction, the neutrino and other particle exchange one of three bosons, either a $W^{\pm}$ or a Z^0. Due to the very low cross section of neutrinos with other particles, the neutrino signal for any experiment will naturally be small.

Solar Neutrino Detectors

Solar neutrino detectors can be split into two categories - radiochemical and Cerenkov. In radiochemical detectors a chemical compound containing an element with a relatively large cross section to neutrino interaction is placed in a large tank shielded from cosmic rays by being built underground. For example the Homestake [7] detector uses the reaction:

$$\nu_e \ + \ ^{37}Cl \ \rightarrow \ e^- \ + \ ^{37}Ar,$$

while SAGE [8] and GALLEX [9] use:

$$\nu_e + {}^{71}Ga \rightarrow e^- + {}^{71}Ge.$$

These experiments can expect about one neutrino interaction per day and they count over long periods of time. Several times each year the chemical mixture is measured and an assay of the number of the daughter products from the expected neutrino interaction is taken. Although they have an energy threshold as low as 0.2332 MeV they are only sensitive to ν_e.

The second type of neutrino detector being used are Cerenkov detectors, such as Kamiokande and Super Kamiokande. A large volume of water is also built underground for shielding purposes, but this time instead of measuring the chemical remnants of a neutrino interaction they make real time measurements of neutrino scattering with electrons in the water:

$$\nu_e + e^- \rightarrow \nu_e + e^-$$

The neutrino goes through a scattering processes by exchanging a Z^0 or W^+ boson with the electron. The relativistic electron will produce Cerenkov radiation as it travels through the water. Cerenkov radiation occurs when a charged particle moves through a medium faster than the speed of light in that medium. For an electron in water the kinetic energy must be greater than 0.262 MeV. The Cerenkov radiation is in the visible spectrum and is emitted in a cone of angle 41° with respect to the direction of motion. In the detector an array of photo-multiplier tubes surrounds the water. This allows the direction of the incident neutrino to be determined allowing any events not originating from the direction of the sun to be identified as background events. An energy spectrum may be produced since the number of of Cerenkov photons emitted is proportional to the neutrino energy.

Super Kamiokande, a Cerenkov neutrino detector, expects 46.4 events per day above their threshold of 6.5 MeV assuming standard solar model fluxes [10]. Although they can detect all types of ν interaction, they are primarily sensitive to ν_e interaction and can not distinguish between the different types of neutrinos.

Interaction of the Sudbury Neutrino Observatory

The Sudbury Neutrino Observatory (SNO) has at its core 1000 tonnes of heavy water. It will utilize the relatively high cross section between ν and the deuteron to measure both the total ν flux and the ν_e flux.

There are three neutrino interactions to which SNO will be sensitive. The first is a charged current reaction. A W^+ boson is exchanged between the ν_e and the neutron in the deuteron;

$$\nu_e + d^+ \rightarrow p^+ + p^+ + e^-$$

The energetic electron will then produce Cerenkov radiation in the water. The amount of energy the electron has is directly dependent on the incident energy of the neutrino and the number of Cerenkov photons emitted is directly dependent on the energy of the electron. Therefore a measurement of the energy of the neutrino can be made by the number of Cerenkov photons that are detected.

The direction that the resulting electron travels is correlated to the direction of the incident neutrino. Also, this method is sensitive to only electron neutrinos.

The second type of interaction, the neutral current reaction, is similar to the first except instead of a W boson being exchanged between the deuteron and the neutrino, a Z^0 boson is exchanged;

$$\nu_x + d^+ \rightarrow p^+ + n + \nu_x$$

In this case the neutrino remains intact and leaves the heavy water after transferring enough energy via a Z^0 boson to split the nucleus of the deuteron apart. The free neutron may then be detected by capture on D_2O or other additives to the D_2O, or by proportional counters distributed throughout the heavy water. This reaction occurs independent of neutrino flavor and allows a measurement of the total neutrino flux coming from the sun.

The final interaction is independent of the deuteron nucleus. Here electron scattering occurs, leaving the neutrino intact and scattering the electron;

$$\nu_x + e^- \rightarrow \nu_x + e^-$$

Again this interaction is independent of neutrino flavor but the cross section for ν_e interaction is 6 times larger than the other types of neutrinos. This reaction is expected to occur at a rate of about 1/10th of the charged current reaction.

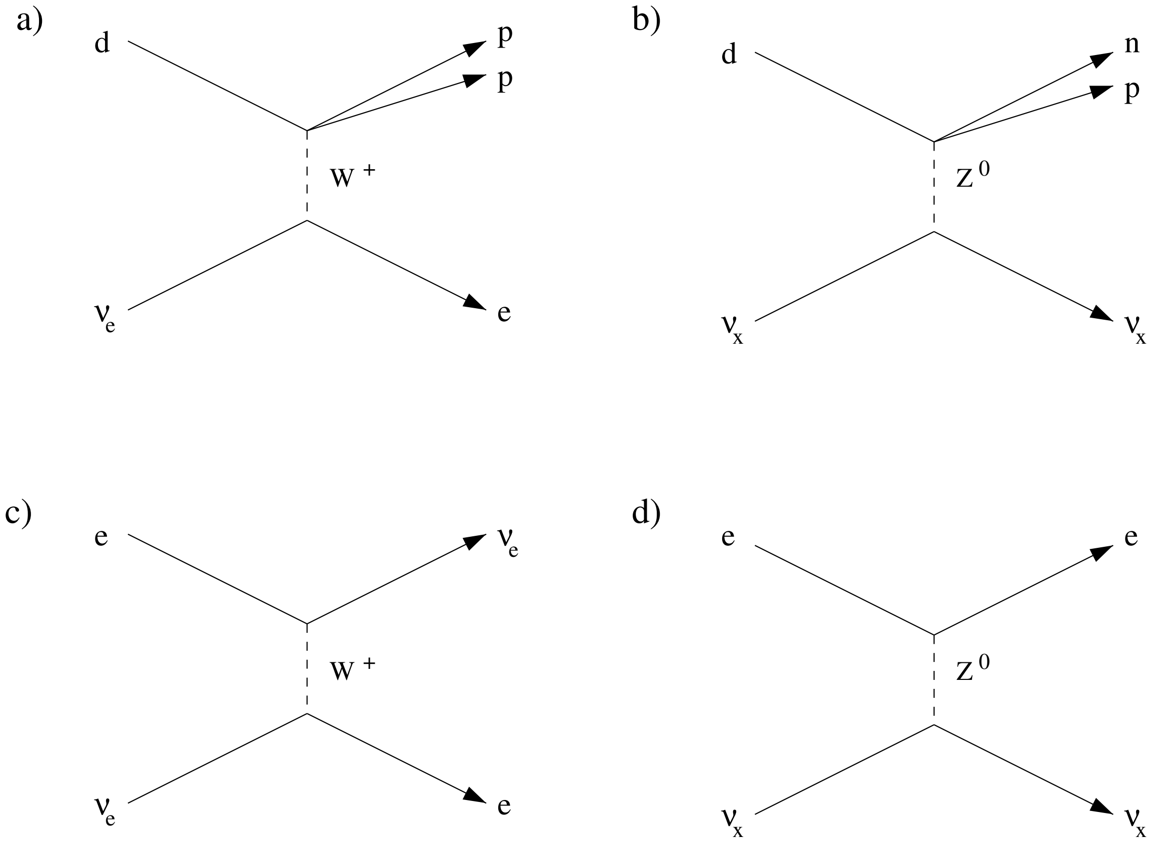

Figure 2.3: Feynman diagrams of neutrino interactions in SNO; a) charged current, b) neutral current, c) and d) electron scattering. Time is from left to right on the horizontal axis and space is on the vertical axis.

lower energy neutrino and an energetic electron.

3 The Sudbury Neutrino Observatory

The Sudbury Neutrino Observatory is a heavy water Cerenkov neutrino detector located at the 6800 foot level of INCO's Creighton mine near Sudbury, Ontario, Canada. [12]

Located 4000 horizontal feet from the the mine shaft is the main cavity which holds the detector (figure 3.1). The cavity is barrel-shaped with a maximum diameter of 22m. The cavity walls have been sprayed with a special low radioactive, waterproof urylon coating to seal the rock. At 27m above the cavity floor a deck has been built to suspend the acrylic vessel and D_2O, hold the electronics and provide access to the cavity. Rooms adjacent to the deck contain a water purification system, a control room, cleaning area, and personnel area.

3.1 The Detector

In the centre of the detector is a flask-shaped vessel that holds 1006.5 tonnes of heavy water. Made of acrylic, this 12 m diameter spherical vessel is suspended from the deck above by 10 support ropes. A 1.5 meter diameter neck extends 6.8 m up to the deck in order to allow access to the interior of the vessel to fill and empty the detector

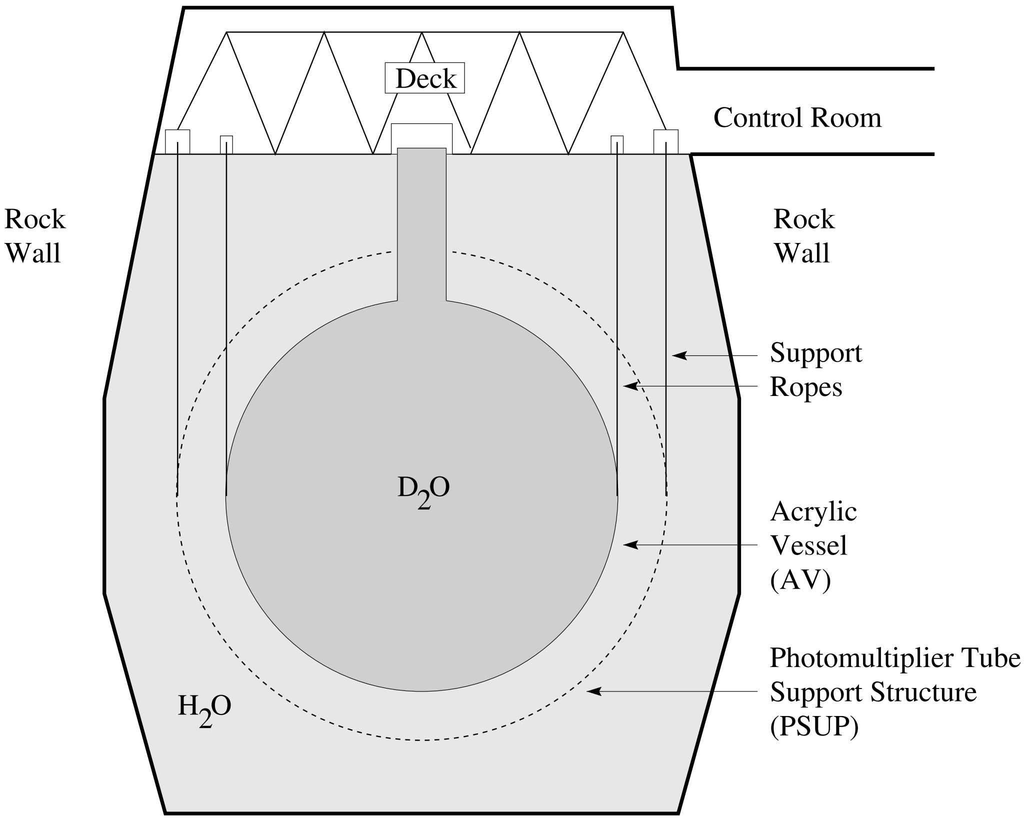

Figure 3.1: Sketch of the Sudbury Neutrino Observatory Detector.

as well as to lower calibration sources into the water. The 122 acrylic panels that make the vessel were brought underground piece by piece and bonded in the cavity to form the 916 m^3 volume to hold the heavy water.

The 1006.5 tonnes of D_2O has been borrowed from Atomic Energy of Canada Limited (AECL) in order to do this experiment. With a purity of 99.92%, with the remainder being HDO, the heavy water is purified through SNO's water systems to better than 10^{-14} grams of Uranium and Thorium per gram of water (g/g U & Th).

Surrounding the acrylic vessel is a 889 cm radius geodesic structure which is used to support the photo-multiplier tubes. This PMT support structure (PSUP) was supported by 15 stainless steel wire ropes until water fill. After water fill the PSUP becomes buoyant and is therefore cabled to the cavity floor.

The PSUP is divided into 751 panels, each panel housing from 7 to 21 photo-multiplier tubes for a total of 9456 facing the D_2O (inward pacing PMTs). The PSUP also holds 91 PMTs facing outward from the structure that will be used for detection of backgrounds such as cosmic ray muons. In addition to suspending the PMTs, the panels and PSUP struts act as a barrier between the inner and outer parts of the light water. Due to the difficulty in keeping the outer areas clean during construction, it acts as a water barrier by keeping the water from the outer volume from mixing with the inner volume. Also it functions as a light barrier to keep the significantly high levels of light generated from the radioactivity of the rock walls from entering the inner volume.

Ultra pure light water fills the volume between the acrylic vessel and the PSUP and the area between the PSUP and the cavity wall. The light water not only shields the D_2O from γ rays from radioactive decays in the rock wall and PMTs, but is also held at a constant temperature of 10° C to cool the PMTs and thereby lowering their noise rate.

The light water will be maintained at a level of cleanliness of less than 10^{-14} g/g U & Th for the 1300 tonnes of water inside the PSUP and 10^{-13} g/g U & Th for 5700 tonnes between the PSUP and cavity wall to reduce sources of background. In addition to filters and reverse osmosis the light water goes through a process using UV light to kill any bacteria and is de-gassed to suppress any biological growth in the water.

3.2 Photo-multiplier Tubes

The photo-multiplier tubes in this experiment have been chosen using very strict specifications. They had to be operational under a maximum of 22m of light water. The failure rate had to be low enough not to affect the expected lifetime of the experiment, about 10 years, and they had to retain this low failure rate with no maintenance once the detector was filled with water. After these considerations were made, the materials used in their construction were limited to low radioactivity in order to keep the PMTs from introducing backgrounds to the experiment.

The photo-multiplier tubes used in SNO are 20 cm Hammamatsu R1408 PMTs, shown in figure 3.2. The 9456 inward-facing tubes provide a photo-cathode solid angle coverage of 31%. Each PMT has a 14 cm radius aluminized light concentrator attached, increasing the area covered to 64%.

The PMTs have a Venetian blind style dynode structure, with a timing resolution of 1.50ns (rms). Having a mean noise rate of 2300 Hz at 20° C, they are expected to

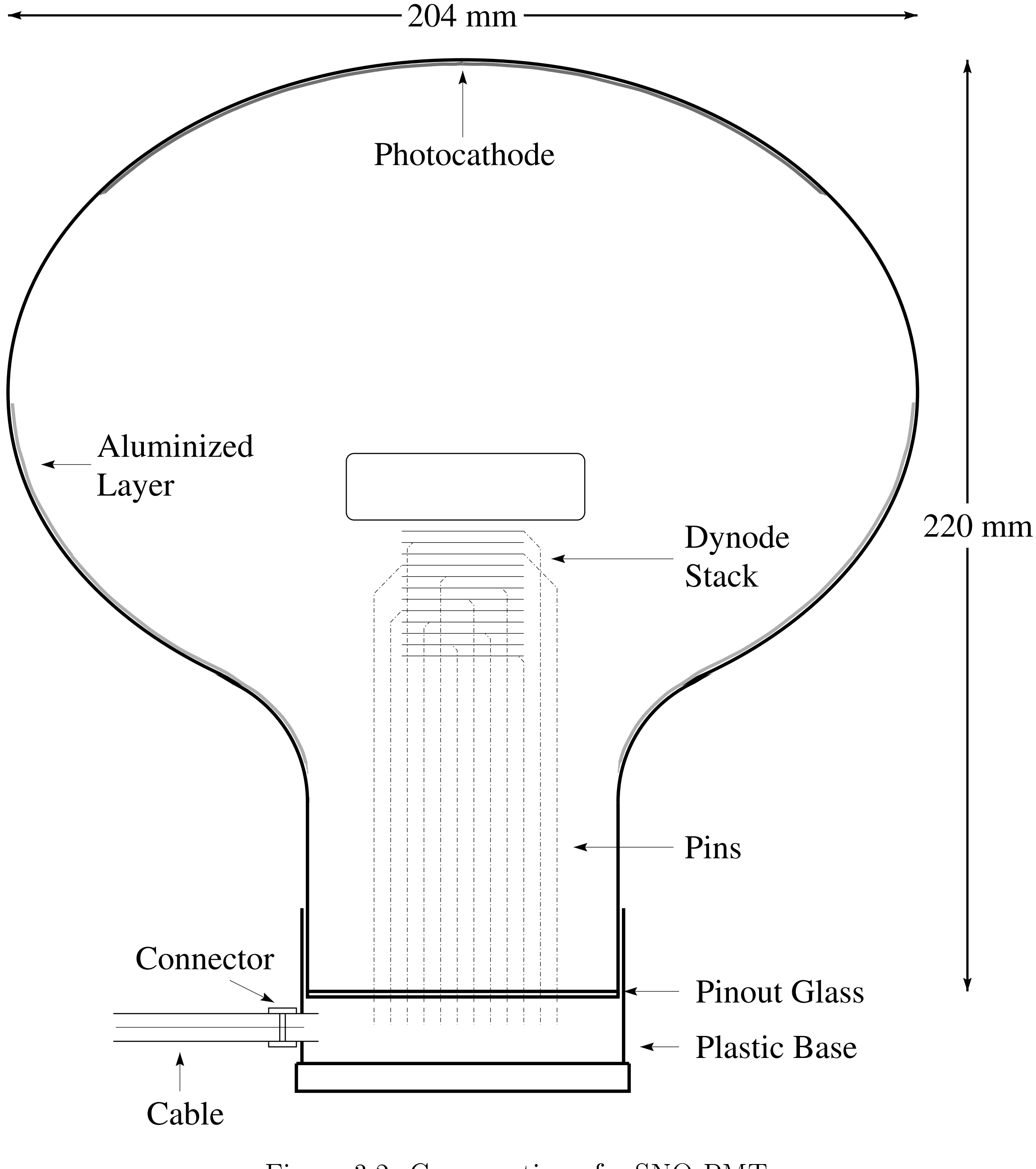

Figure 3.2: Cross section of a SNO PMT.

function under normal running conditions at a noise rate of 1000 Hz when cooled to 10° C. The PMTs have a nominal operation voltage that range from 1700 V to 2100 V with a mean of 1875V.

The glass envelopes for the PMTs were made by Schott Glaswerke using strict cleaning procedures in order to keep uranium and thorium levels to a minimum. The bulb has a diameter of $20.4 \pm .2$cm and a thickness that ranges from 1.5 mm to 4.0 mm.

The high voltage/signal cables run from the PMTs in the PSUP to the deck above where the SNO electronics are located.

3.3 SNO Electronics

Electronic Crates

The PMT cables from the cavity are fed up through the deck to 19 electronics crates, each crate holding up to 512 PMT channels.

The electronics in each crate are divided into 16 motherboards, called front end cards (FECs). The PMT cables and FECs are joined together by PMT interface cards (PMTics). Thirty-two PMT cables plug into a single PMTic which connects directly into a FEC. Relays to apply voltage on the PMTic allow PMTs to be turned on or off in groups of 8 and are computer controlled.

The PMT signal is fed into one of 8 4-channel discriminator chips on the FEC. If the signal passes the discriminator threshold the signal is split into 2 branches, one into a low gain integrator and one into a high gain integrator. To measure the height of the pulse from the PMT there are 3 sets of 16 storage capacitor cells for each PMT. The low gain signal is stored on one cell of one of the sets of capacitor and the high gain signal is stored twice, once on the second set of storage cell after an integration time of 60 ns and once on the third set of storage cells after 400 ns of integration time. Having 16 cells per charge signal is to accommodate short periods of high event rates such as in the case of neutrino detection from a supernova when event rates can be higher than the electronic readout can handle. During an event for regular running conditions the charge is deposited on one of the 16 capacitors and it is read out before the next event arrives.

A fourth array of 16 capacitors is used to measure the time a PMT fires. A charged capacitor starts discharging once a PMT signal passes the discriminator and stops when it receive a global trigger (see "Trigger System" below), or resets itself after a set timeout period. If a system-wide global trigger (GT) is received before the timeout period the amount of charge remaining on the timing capacitor is read, as well as the three pulse height capacitors. A global trigger identification number (GTID) is stored in memory as well as the 4 analog pulses for each PMT that fires.

The signals stored in memory are in turn read out by a 12 bit, 2 μs analog to digital converter. The information is then read out crate by crate by the data acquisition system and the events are reconstructed off line using the GTID. Memory storage is sufficient to handle short burst rates of 1 MHz possible from a supernova.

Trigger System

Each PMT fires independently of the rest of the system and will be expected to do so at a noise rate of 1000 Hz under normal operating conditions. Also, the PMTs will detect many events due to low-energy backgrounds that will be below the threshold of the overall detector. To keep the system from becoming overwhelmed from background and noise events a global trigger must be received by the PMT within a preset time length after the PMT pulse crosses the discriminator threshold or else the information for that PMT is ignored and all electronics for that PMT are reset. The GT is sent from a master trigger card to each crate under several possible conditions; a preset number of PMTs in the detector fire relatively close in time to each other, the total charge detected by the PMTs is above a certain threshold or a software or calibration device can produce a GT to signal that a calibration event is occurring.

The number of PMTs that fire (Nhits) is an indirect measurement of the amount of energy a particle in the detector has. A charged particle emitting Cerenkov radiation as it travels in the water is expected to produce roughly 10 Nhits per MeV of kinetic energy. This is expected to be the main triggering system of the detector. A secondary trigger system, called the Esum, is implemented by summing all of the analog signals from the PMTs to produce a trigger based on the total charge detected by all the PMTs in the detector. A software or exterior source can also be used to trigger the detector. The type(s) of trigger that initiate the global trigger is included with the data for each event.

A schematic for the Nhit and Esum triggers is shown in figure 3.3. The Nhit trigger pulse is generated by summing logic pulses from all PMT channels. When a PMT passes the discriminator threshold a 100 ns long square pulse is produced on the FEC. The FEC then sums any coincident 100 ns pulses from the other 31 PMT channels on that same FEC board. The total pulse from the FEC is then summed with the 15 other FECs at the crate level and the pulse is sent to a master trigger card which in turn sums the Nhit signals of the 19 crates. A GT is then sent out if

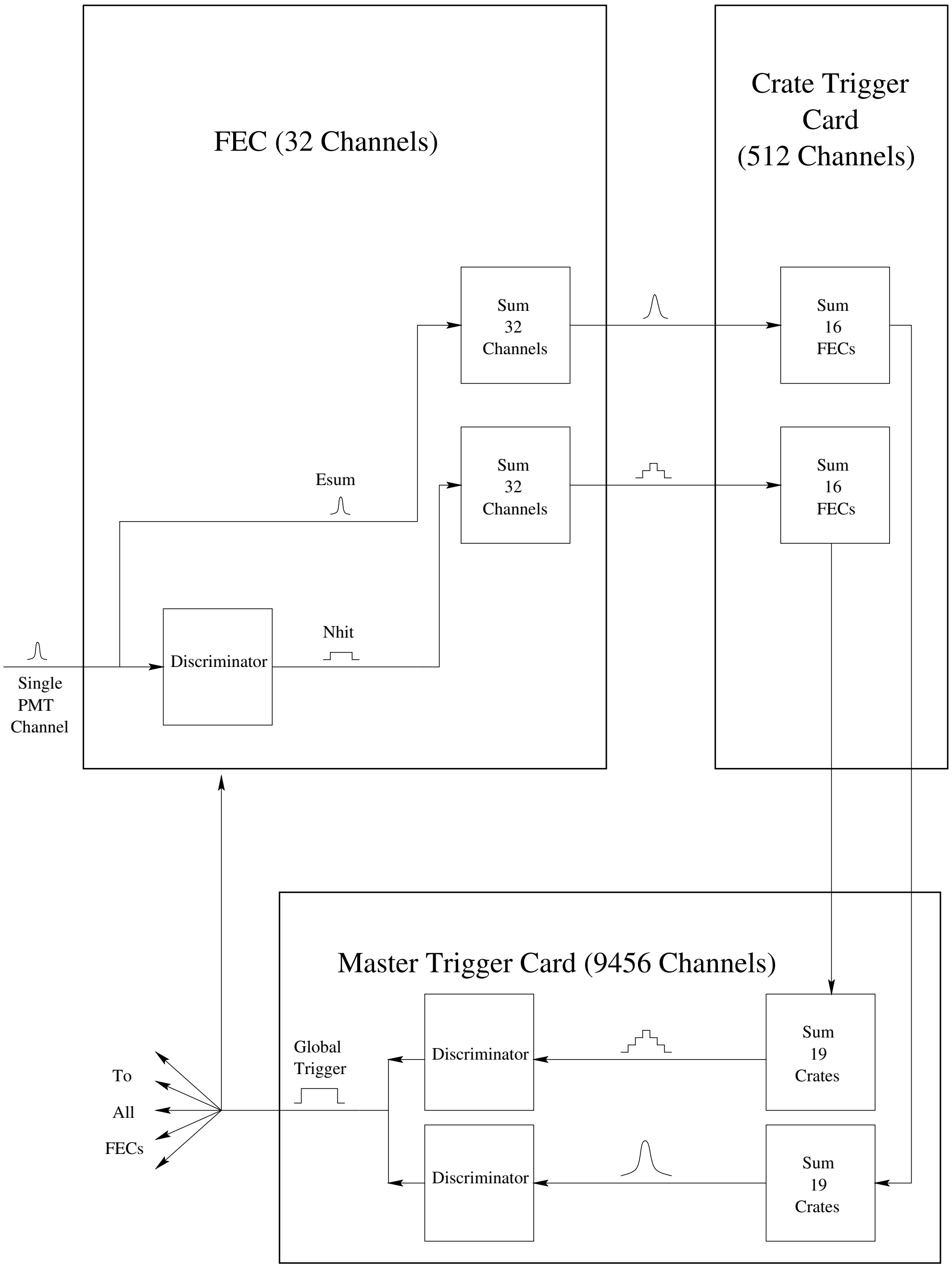

Figure 3.3: Schematic of SNO trigger system.

the summed pulse passes a certain predetermined threshold. This relies on the PMT discriminators firing at or near the same time otherwise the summed pulse will not be high enough to pass the GT threshold. A parallel system sums the analog pulses from the PMTs to create the Esum trigger.

Similar independent triggers are implemented for the outward looking tubes. This can create a global trigger for the whole detector for such events as a muon which passes through the water outside of the PSUP in order to identify these types of events.

Finally there are several software triggers independent of the PMTs. The pulsed global trigger (PGT) is a periodic trigger that is sent to the detector. The frequency can be set anywhere from 0.04 Hz to 390 kHz [13] and is convenient for sampling the detector. Another trigger is set up to receive input from an external source, such as a calibration device. A signal generated by the calibration source is timed to be received by the master trigger card at the same time that the calibration source produces an event.

The window of time relative to the GT that is considered an event can be adjusted by software and is set to approximately 400 ns and any PMT that fires within this time window is included in the event. There is a minimum of about 430 ns in between global trigger events. A 10 MHz clock is used to place a date and time stamp on an event while a more precise 50 MHz clock is used to determine the event to event time.

3.4 Calibration

There are many levels of calibration, from a single PMT, to the electronics, to calibrations of the detector as a whole. Many calibration tools have been built into the electronics, as well several external sources have been built to determine such things as energy and optical calibrations.

At the electronics levels, the PMT charge capacitors must be calibrated in order to obtain a conversion from ADC counts to number of photo-electrons (pe) detected. This is a two step process, an offset and gain must be applied. First the zero offset (pedestal) is measured. This is done by taking a reading of the pulse height after electronically firing the discriminator and is a measurement of the capacitor charge when no PMT pulse is present. The next step is done by injecting a known amount of charge onto the capacitor and firing the discriminator in order to find the charge vs ADC slope for the capacitors. These steps are done for each of the 16 cells of the three capacitor cell arrays for every PMT in the detector.

This part of the calibrations only relies on the characteristics of the electronics. At this point there is still a PMT to PMT variance due to individual characteristics. A calibration factor is introduced so that the average pulse height for a single photon is the same for each PMT.

The timing capacitor requires a pedestal measurement similar to the charge capacitors. The timing slope is then found by sending a pulse to fire the PMT discriminator, then firing the global trigger a known delay time after triggering the PMT. From this a time vs. ADC slope can be made to calibrate times.

A nitrogen-dye laser system has been built to do several calibrations [6]. A 600 ps wide mono-energetic light pulse is produced using a nitrogen laser which is then pumped through one of a selection of dyes in order to produce light of different wavelengths. The light is transferred to an isotropic diffuser ball (laser-ball) via an optical fiber and the intensity of the output light is varied using neutral density filters. The laser-ball can be used to do such calibrations as attenuation of light in D_2O and H_2O, single photon efficiency, timing calibration and charge calibration.

Several radioactive sources have been made to calibrate the energy of the detector. Many of these sources have tags to identify a decay has occurred - for example a β quickly followed by a γ ray or neutron. The detection of the β in the calibration source is used to create a global trigger in order to cleanly detect the subsequent γ ray or neutron.

3.5 SNOMAN & Analysis

The SNO Monte Carlo and Analysis (SNOMAN) code is a hybrid of existing simulation code and code written by the SNO collaboration members specific to this experiment. Based mainly on FORTRAN, the code uses CERNLIB's ZEBRA package to handle data which is processed through several independent external processors. SNOMAN also uses SNODB, based on CERNLIB's HEPDB, to handle all calibration constants and detector status at the time of running.

The Monte Carlo geometry has been created by collaboration members. Simulation of particle transport uses tracks and vertices. A track is the path a photon or particle takes through the detector. When it interacts with another particle or changes boundaries in the geometry a vertex point is defined at that position, at which time a new path is initiated for the new or scattered particle or for the original particle moving past the boundary through the new material. Electron and gamma simulation is handled using the EGS4 code [14].

Data from the SNO data acquisition program is packed in ZEBRA banks. The data is prepared for analysis using a processor in SNOMAN which unpacks the data and uses the constants from SNODB to calibrate the information. The data is then exported to disk using CERNLIB's HBOOK format which can be analyzed using such programs as PAW.

Another analysis tool used is ROOT [15], an alternative to the HBOOK format. The SNOMAN processor unpacks the data banks and calibrates the data and then another processor packs the data in a ROOT "tree" structure. That is, each run is split into a series of events, each event split into a series of the PMTs that fired, each PMT split into the individual measurements. The advantage to using this analysis package, other than a more organized hierarchal structure for the data, is that analysis can be done using C++ and object oriented programming. A set of standard analysis tools to view the data has been created and individuals can create their own analysis tools by a combination of writing their own code and linking to the standard libraries. All data analysis in this thesis uses the ROOT analysis program after the data has been processed with SNOMAN.

3.6 Neutrino Detection in SNO

The neutrino interactions for the SNO detector, described in section 2.3, liberate two types of detectable particles - electrons and neutrons. It is these particles that are subsequently detected and supply information about the neutrinos.

The charged current and electron scattering interaction of neutrinos with D_2O emit a highly energetic electron. Traveling close to the speed of light, the velocity of the electron is higher than the speed of light in D_2O. With an index of refraction of n=1.333 [2] for D_2O, an electron will produce Cerenkov radiation above a kinetic energy of 0.262 MeV. One of the characteristics of Cerenkov radiation is that it is emitted in a forward direction in a cone [11] with an opening angle θ such that

$$cos\theta = \frac{1}{\beta n} \tag{3.1}$$

where β is the electron's speed relative to the speed of light. In D_2O the Cerenkov light will be emitted at an angle of 41°. The electron emits approximately 358 photons per cm of travel in the wavelength range at which the PMTs are sensitive (λ = 300 to 650 nm), and it travels about 0.45 cm per MeV in D_2O [2].

The PMT array is used to detect the photons from Cerenkov radiation. The number of PMTs hit in an event is approximately proportional to the energy of the electron. The position and direction of the electron is fit using an algorithm that make use of the relative times that the PMTs fire and the position of the PMT. Using the fit position, direction of electron travel, and energy of the electron, the neutrino energy spectrum for the charged current reaction can be inferred. The fit position is used to identify background events (i.e. events that occur outside the acrylic vessel such as radioactive decay).

For the neutral current reaction the deuteron receives enough energy from the neutrino to split apart the nucleus and the free neutron can be detected. Neutron capture on deuterium will be the initial detection method. Capture results in a mono-energetic γ ray at 6.25 MeV [2].

To increase the sensitivity to neutron detection two techniques will be used. The first is to introduce $MgCl_2$ into the heavy water. Neutron capture on the Cl emits a cascade of γ rays with a total energy of 8.6 MeV which in turn can then be detected through Compton scattered electrons in the water.

The second method of increasing neutron detection will be to use proportional counters that take advantage of the high neutron capture cross section on ^3He. Ninety-six of these 5.08 cm diameter tubes of varying lengths will be set up in an lattice array throughout the D_2O in order to improve neutron detection.

3.7 Backgrounds

Any γ ray with an energy greater than a few MeV or any neutron entering the heavy water vessel can imitate a neutrino interaction with D_2O. Because of this, not only was shielding a great concern but special care had to be made to ensure that the materials used had sufficiently low concentrations of radioactive materials in them.

The first background consideration for this type of experiment is the reason the detector is placed underground - to block cosmic rays. At the 6800' level where the detector has been built the only cosmic rays able to penetrate are muons and neutrinos. At this depth only 24 muons are expected to enter the D_2O volume per day [2]. These can easily be removed from the data due to the characteristics of these interactions. The muon will produce Cerenkov radiation as it passes through the detector emitting much more light than a neutrino event. Any spallation products of the muon can be removed by rejecting any data for several hundred milliseconds after a muon event is detected.

The other type of background arises from naturally occurring radioactive elements found in varying concentration in all materials on earth. Decay chains such as ^{232}Th and ^{238}U (fig. 3.4) can emit α, β, and γ particles. The α particles may interact with light elements to release neutrons or high energy γ rays. The neutrons may then be captured releasing a γ ray. Gamma rays, from decay of excited nuclear states or through subsequent neutron capture, can have enough energy to photo-disintegrate a deuteron in the heavy water, appearing to be a neutral current neutrino interaction. The γ rays can also Compton scatter off electrons to produce a high energy electron similar to the charged current or electron scattering neutrino interactions.

The rock walls are a strong source of these decay products. To shield from them H_2O is filled in the space between the walls and acrylic vessel. This light water is a minimum of 2.5 m from the wall to the PSUP. The few γ rays that travel through the light water into the PSUP volume and interact between there and the heavy water can further be removed from data by removing events that reconstruct outside of the acrylic vessel.

All materials that have been used in the detector have been specially chosen and tested to ensure that they have low enough levels of U and Th. Also, leaching rates of the materials over long term submersion in water has been considered to limit the rate at which the construction materials increase the radioactivity levels in the water.

Although the PMTs have glass that was specially made by Schott Glaswerke to be much cleaner than normal, the glass still has the highest concentrations of U and Th

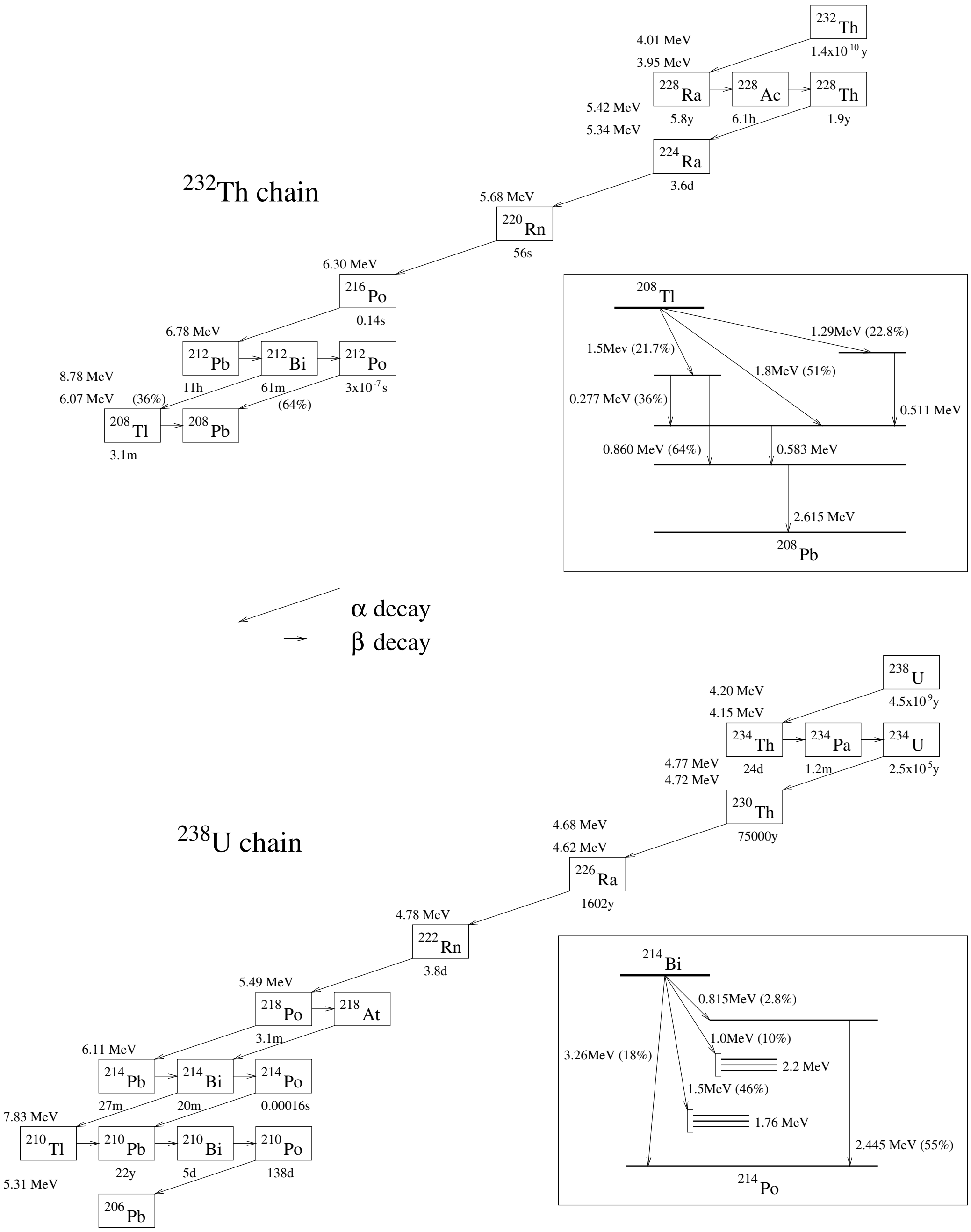

Figure 3.4: ^{232}Th and ^{238}U decay chain. Insets show high energy β particles and γ rays in the chain.

of any of the materials used inside the PSUP at $3 \cdot 10^{-8}$ g/g U & Th. This contributes a very significant part of the low energy background and will be discussed in more detail in later chapters.

By keeping the environment and materials used in the detector construction extremely clean, backgrounds above a few MeV have been kept to a minimum.

In figure 3.5 a Monte Carlo energy spectrum of the expected rates for each background is shown and compared to the energy spectrum for neutrino interactions. These include electron scattering (ES), charge current (CC), and neutral current (NC) neutrino interactions. The charged current reaction and electron scattering rates calculated assume one third the standard solar model neutrino flux and full standard solar model for the neutral current reaction. The backgrounds included are from PMT $\beta\gamma$ decays, $\beta\gamma$ decays in the D_2O (internal $\beta\gamma$), free neutrons (NC background) and γ rays from PSUP and cavity radiation. These calculations assume that NaCl is being used in order to increase the neutral current detection.

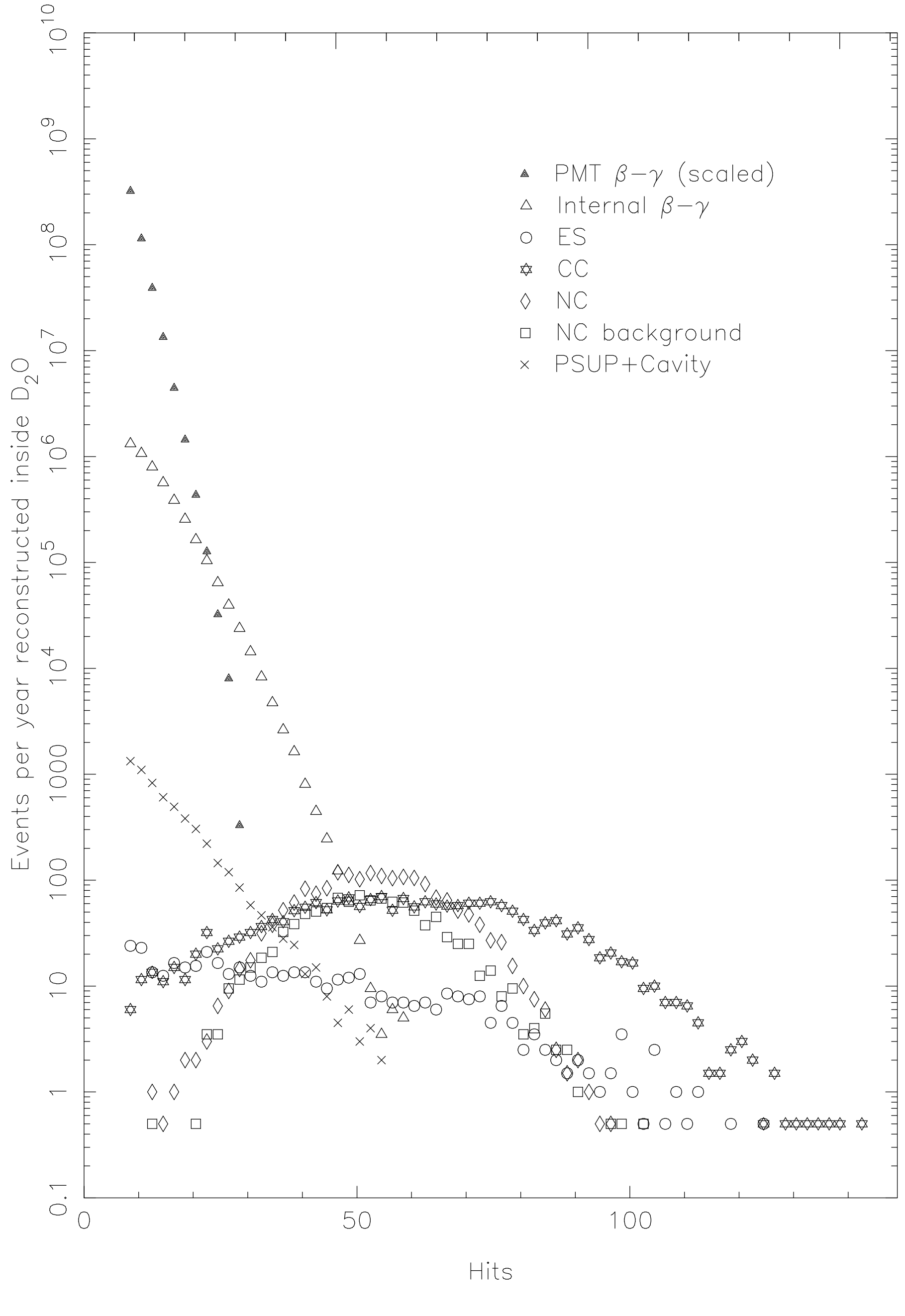

Figure 3.5: Energy (Hits) spectrum of expected number of events per year for the neutrino interactions in SNO, including electron scattering (ES), charge current (CC), and neutral current (NC). The backgrounds due to PMT $\beta\gamma$ decays, $\beta\gamma$ decays in the D_2O (internal $\beta\gamma$), free neutrons (NC background) and γ rays from PSUP and cavity radiation are also included. [16]

4 SNOMAN Charge Calibration

The photo-multiplier tubes in SNO are sensitive enough to detect single photons. A photon strikes the photo-cathode and releases a single photo-electron (pe). After multiplication through the dynode chain the single photo-electron is converted into a pulse of 10^7 electrons. This pulse is then sent to the electronics and the pulse height is measured. The charge measurement has two main roles in SNO - it is used to improve the measurement of the relative time that the light reaches the PMT and is a tool to identify background events.

The PMT discriminator fires when the leading edge of the pulse is above a threshold. However the time at which this occurs depends on the size of input pulse. Since there is a statistical variation during the electron multiplication in the dynode, the pulse height from a single photon may vary in range. A large pulse from a single photon will fire the discriminator several nanoseconds earlier than a smaller pulse from a similar single photon. A correction to the time must be made depending on the size of the pulse. This improves the reconstruction of the event, which depends heavily on the time the photon arrives at the PMT. The timing correction of this effect depends on proper charge calibration.

As a diagnostic tool, charge can be used to remove events that are caused by electronic noise. If several PMTs fire due to electronic pickup which creates a global trigger, the average charge per PMT will be much less than 1 pe since most of the discriminators will have fired without a pulse from the PMT.

Finally, a large pulse may be an indication of a $\beta\gamma$ decay in the glass (discussed in detail in chapter 6). The β particle released in a decay produces Cerenkov radiation inside the PMT glass. The proximity of the charged particle to the photo-cathode may result in multiple photons being detected, producing a large pulse that may be used as a method of identifying this type of background event.

In order to use PMT pulse amplitude as a method of identifying PMT $\beta\gamma$ decays the measurement of the pulse must be calibrated. The charge measured on the PMT pulse storage capacitor is in unknown units and must be converted to photo-electrons. Once this is done a pulse height can be set that will be used to identify that a $\beta\gamma$ decay has occurred in the PMT. It is important that the calibration be correct or there is the risk of mis-identifying a neutrino interaction as a background event. Therefore an analysis of the efficiency of the charge calibration is necessary. In this chapter the current method of charge calibration is discussed and analyzed.

4.1 SNOMAN Charge Calibration

The electronics in SNO measure the amplitude of each PMT pulse three times. The pulse is split into a high and low gain signal (see section 3.3 for a description). The high gain signal, Qhs (high gain short integrate charge), is measured after an integration time of about 60 ns. The same signal is measured gain, called Qhl (high gain long integrate), after an integration time 400 ns. Qlx (low gain) is the low gain signal which is also measured after an integration time of 400 ns.

There are three steps to the standard calibration for charge; a zero offset then an amplitude conversion for the storage capacitors, followed by a gain correction due to individual PMT characteristics. The first two steps are electronics calibrations (ECA) and the final is a PMT calibration (PCA) and all are done using SNOMAN routines.

There are two versions of ECA calibration in SNOMAN written independently of each other, dubbed the "old" and "new" methods. Both versions of the code use the same general techniques to calibrate charge with slight differences.

The first step is to subtract the charge offset or "pedestal". The charge on a storage capacitor is read by a 4096 channel analog to digital converter (ADC) and is read as "ADC counts". However the ADC does not necessarily read a value of 0 when a PMT pulse is absent from the storage capacitor. This pedestal is usually in the order of ~600 ADC counts. This offset must be found for each of the storage capacitors and subtracted from the measurement.

The second step is to calculate the ratio of charge on the capacitor to charge read by the ADC. To find these calibration values known amounts of charge are injected onto the capacitor and read by the ADC. Using this, data slopes of charge vs. ADC counts are made. Although not the actual units, for convenience the units after pedestal and slope calibrations have been called pC. This is where the old and new ECA techniques differ. The old ECA fits a function to all the calibration points to find the best value of injected charge vs. ADC counts. For the new ECA instead of fitting a function to the calibration data, all the data points are packed into a compressed format and recorded. When calibrating a PMT event, the calibration data is unpacked and the ADC value is used to find a corresponding value for charge injection.

All of these calibration results are kept in the SNO database, SNODB. There are slight differences in values for each storage capacitor so each charge type has its own set of calibrations in the database. Each PMT has 48 storage capacitors (16 per charge measurement) and there are pedestal offsets and slope entries for each storage capacitor in SNODB.

After electronics calibration there is still a tube by tube variance due to individual PMT characteristics. The final step in the calibration process is to change pC to pe's. This is done with PCA calibration by dividing the pulse measurement by the relative gain of the tube. The gain values are also in SNODB but there is only one entry for each PMT since the value is dependent on PMT characteristics, not electronics. A low intensity laser-ball run is used so that most PMTs only receive a single photon at a time. Histograms are made for each PMT and the peak of each is found and calibrated such that each peak corresponds to 1 pe.

4.2 Qhl and Qhs

The data that will be discussed is from laser-ball run 1018 taken on August 8th, 1998 before the detector was filled with water. The intensity of light output was set such that the fraction of PMTs in the detector that fired during an event (occupancy) was less than 6%, a mean Nhit of about 500 with 8500 PMTs online. At this low occupancy it is expected there would rarely be more than one photon received by each PMT that fired. The wavelength of the output light from the laser-ball was 365 nm. Due to problems with the ADCs in two of the FECs all data from PMTs in crate 4, FEC 1 and crate 16, FEC 5 have been removed from the analysis.

Qhl vs Qhs has been looked at for the three steps of the calibration series using the old ECA. Figure 4.1 shows the pulse height spectrum with pedestal-corrected values. All charge values are in ADC counts. Figure 4.2 has both pedestal and slope correction, but no PCA corrections and therefore has the pseudo-units of pC. The final set of plots, figure 4.3, are complete calibrations, and these values are in photoelectrons. For each step in the calibration there are two plots. The upper plots are simply histograms of Qhs and Qhl to compare the two charge spectra. The lower plots are scatter plots of Qhs vs Qhl, one entry time a PMT fired.

In figure 4.1 it can be seen that the Qhl has a slightly larger tail than Qhs but the two measurement are similar. However on the scatter plot, below 800 ADC counts one can see that there are several events that are scattered away from the main set of events. Many of these appear to be linear, as if for some PMTs Qhs is scaled larger than Qhl.

Figure 4.2 has both pedestal and slope calibrations. Now one can see that there is a much worse agreement between Qhl and Qhs. The two charge types appear to have a ratio of Qhs/Qhl of approximately 1.5.

The events in figure 4.3 have the complete charge calibration. The are still a number of events scattered away from the main grouping of data points and the two measurements still have a 1.5:1 ratio.

Figure 4.4 is a similar plot as those above, this time with the complete calibration using the new ECA method. Features similar to the old ECA are seen here. The ratio of charges Qhs/Qhl is also around 1.5. Also, as seen in the previous plots, there

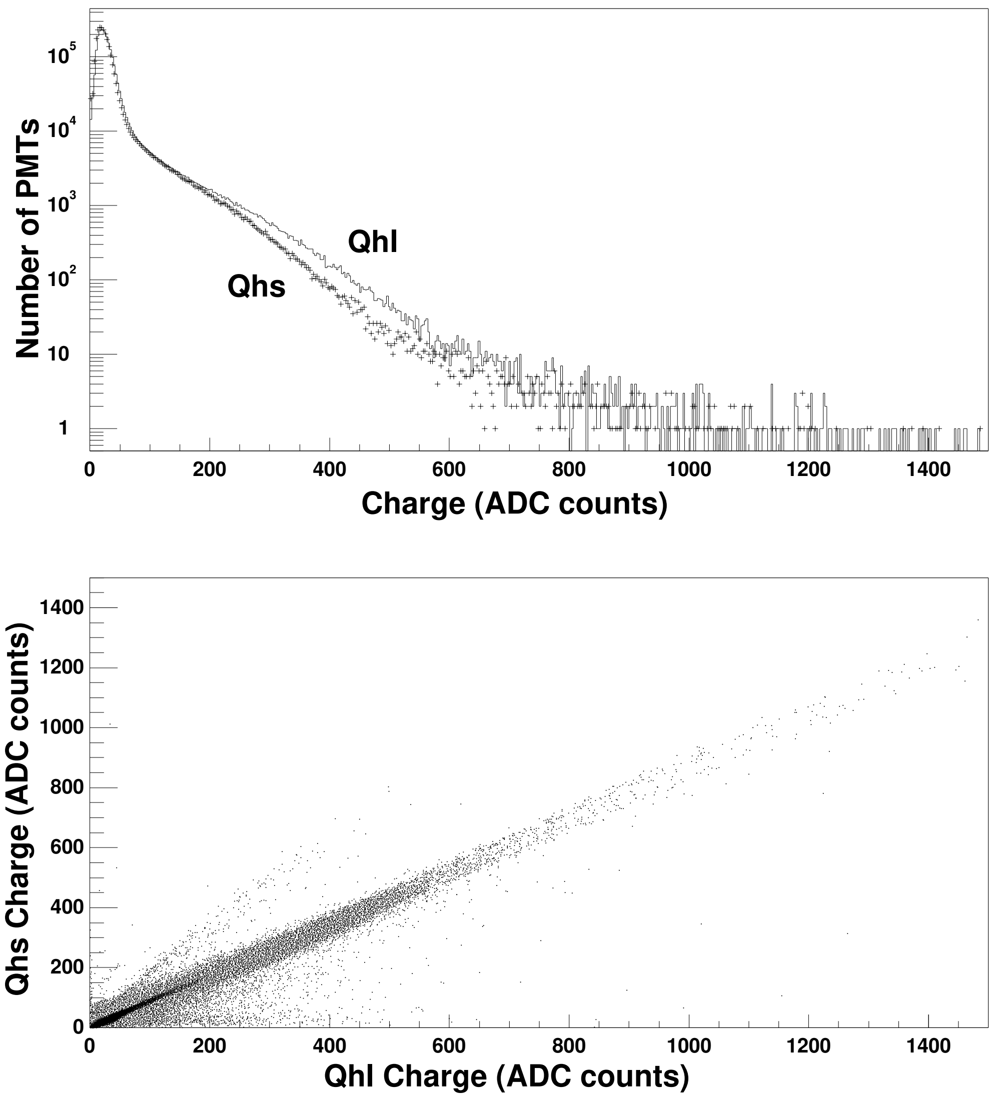

Figure 4.1: Qhl vs Qhs - Pedestal corrected (Old ECA).

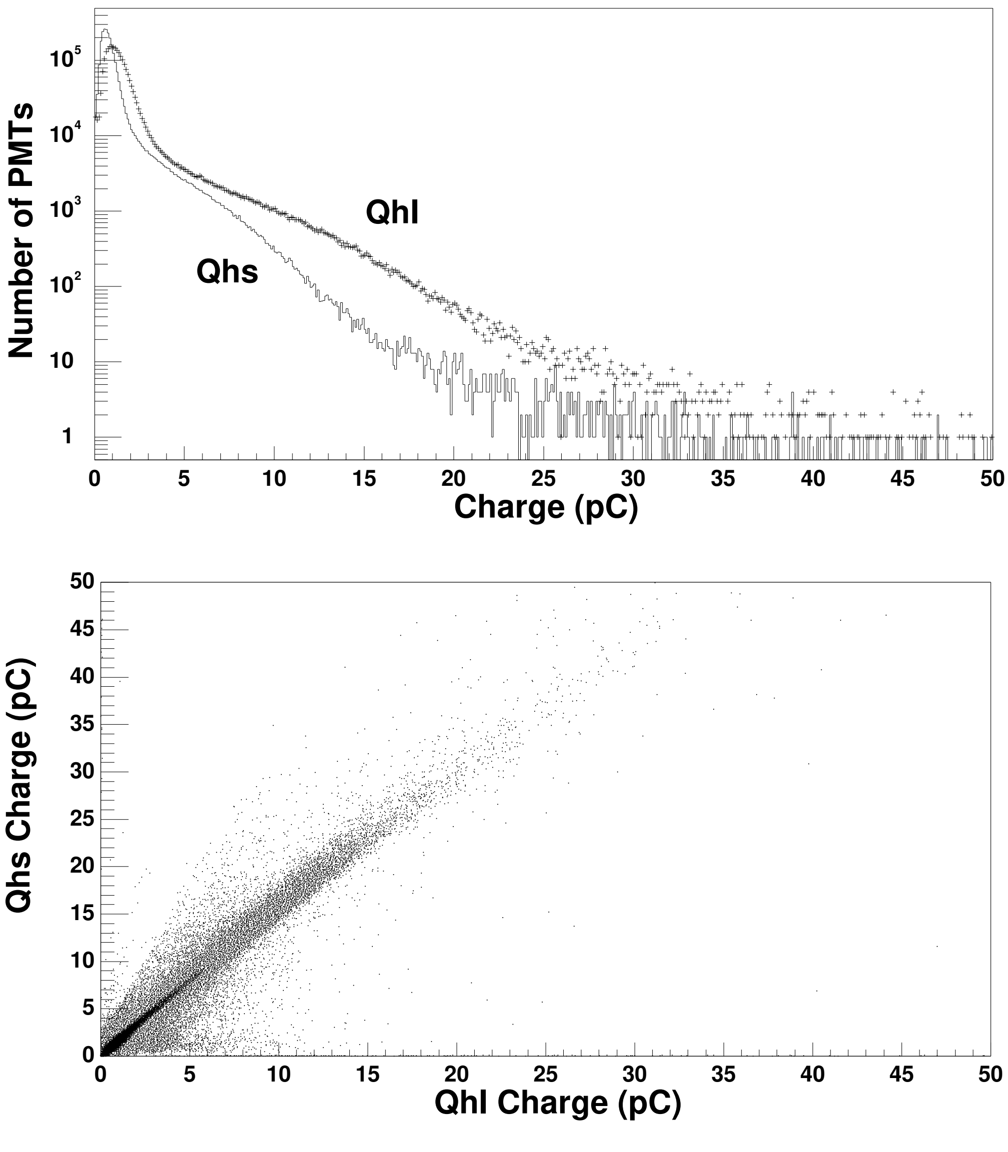

Figure 4.2: Qhl vs Qhs - Pedestal and Slope corrected (Old ECA).

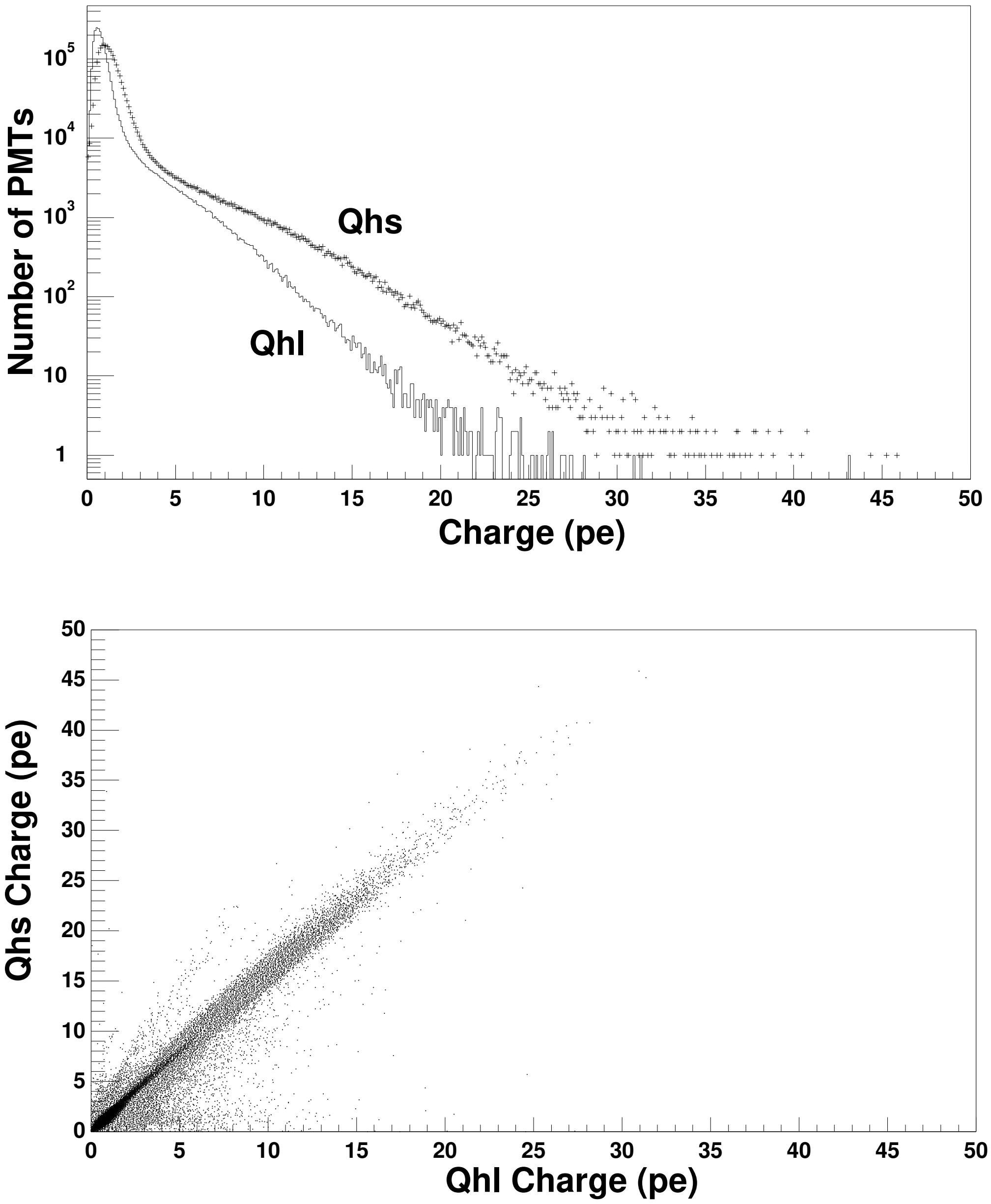

Figure 4.3: Qhl vs Qhs - Complete Calibration (Old ECA).

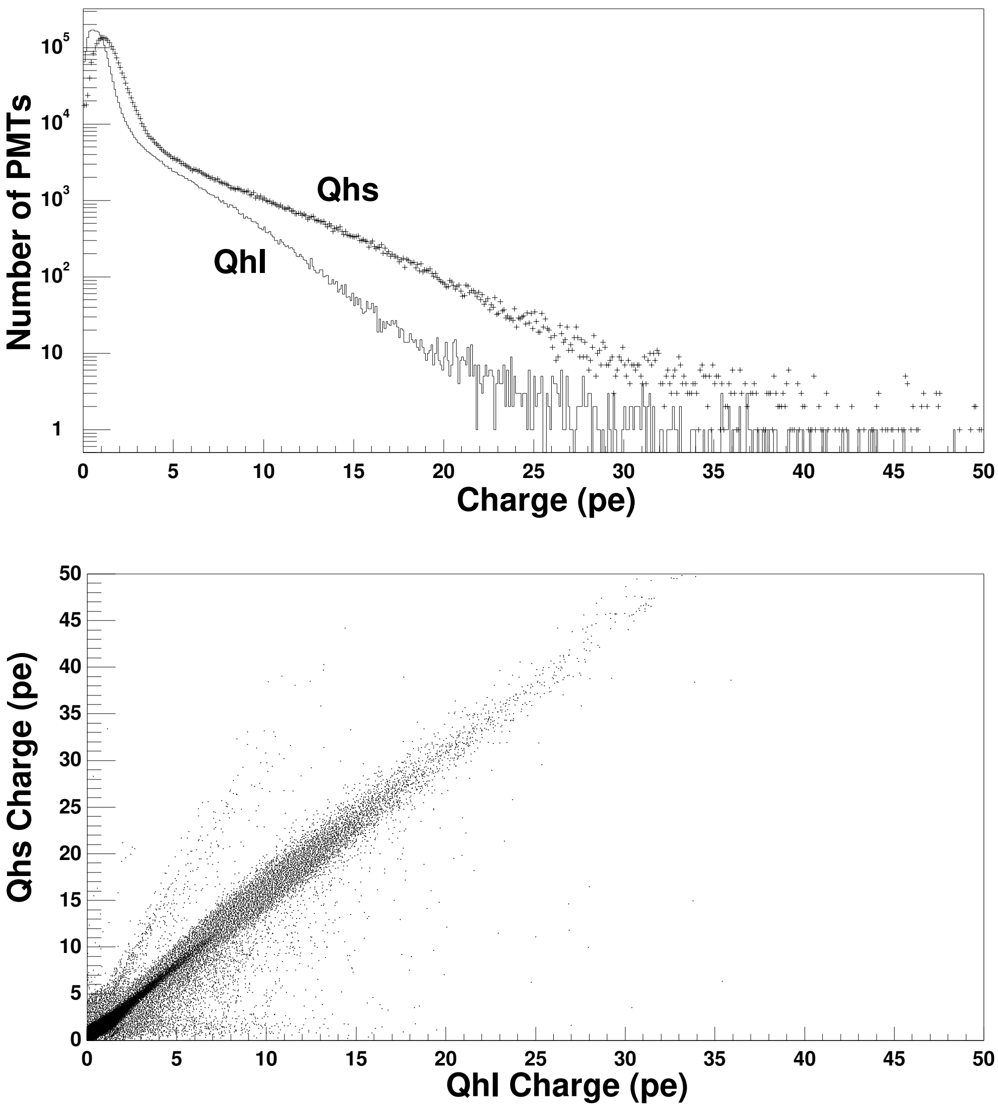

Figure 4.4: Qhl vs Qhs - Complete calibration (New ECA).

are several events scattered away from the bulk of the events including several events that lie in a line with Qhs larger than Qhl.

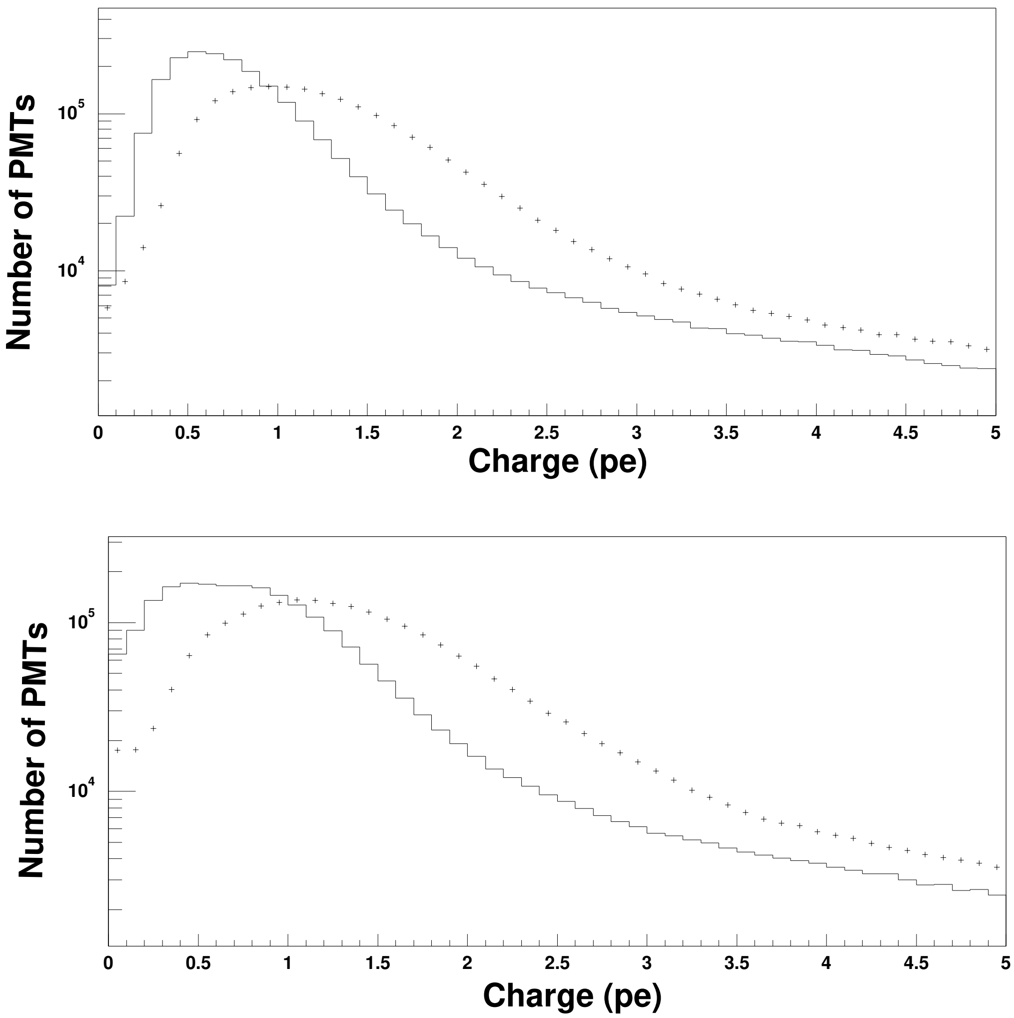

Figure 4.5: Qhl (solid line) & Qhs (crosses) spectra for low pe - Complete calibration: top - old ECA, bottom - new ECA.

Figure 4.5 shows two histograms of Qhs and Qhl with the lower part of the charge spectra magnified. The upper plot shows Qhl and Qhs for the new ECA while the lower plot shows the old ECA. In both cases the single pe peaks for Qhl and Qhs do not match, also showing about a 1:1.5 ratio, a similar discrepancy to the high charge tail events show on the previous plots.

In order to discover whether the problems are detector or calibration related two areas of interest have been chosen. Ignoring the 1.5:1 ratio of charges for the moment, the events that occur scattered away from the rest of the events on the Qhl vs. Qhs scatter plots have been identified. Most of the points lie within a band with slope of Qhs $= 1.5 \cdot$ Qhl. The two regions outside of this band have been investigated. Those events with Qhs larger than 1.5·Qhl + 5 pe are represented by the left two histograms in figure 4.6. Events where Qhs is less than 1.5·Qhl - 5 pe are represented in the right two plots of figure 4.6. There is one bin per PMT and the value in that bin represents the number of times that PMT contributes to the charge in the respective regions. Pmtn refers the the PMT number defined by:

$$Pmtn \;=\; 512 \cdot crate + 32 \cdot FEC + channel.$$

The top two plots in figure 4.6 are for new ECA and the lower two for the old ECA. In both calibration types the events where Qhs are much larger than Qhl (left plots) several of the same pmts contribute to most of these events. This suggests a problem with a few electronic channels where Qhs is read at a much higher value than Qhl. However for Qhl larger than Qhs (right two plots) it seems to occur throughout the detector. These events are probably due to the much longer integration time of

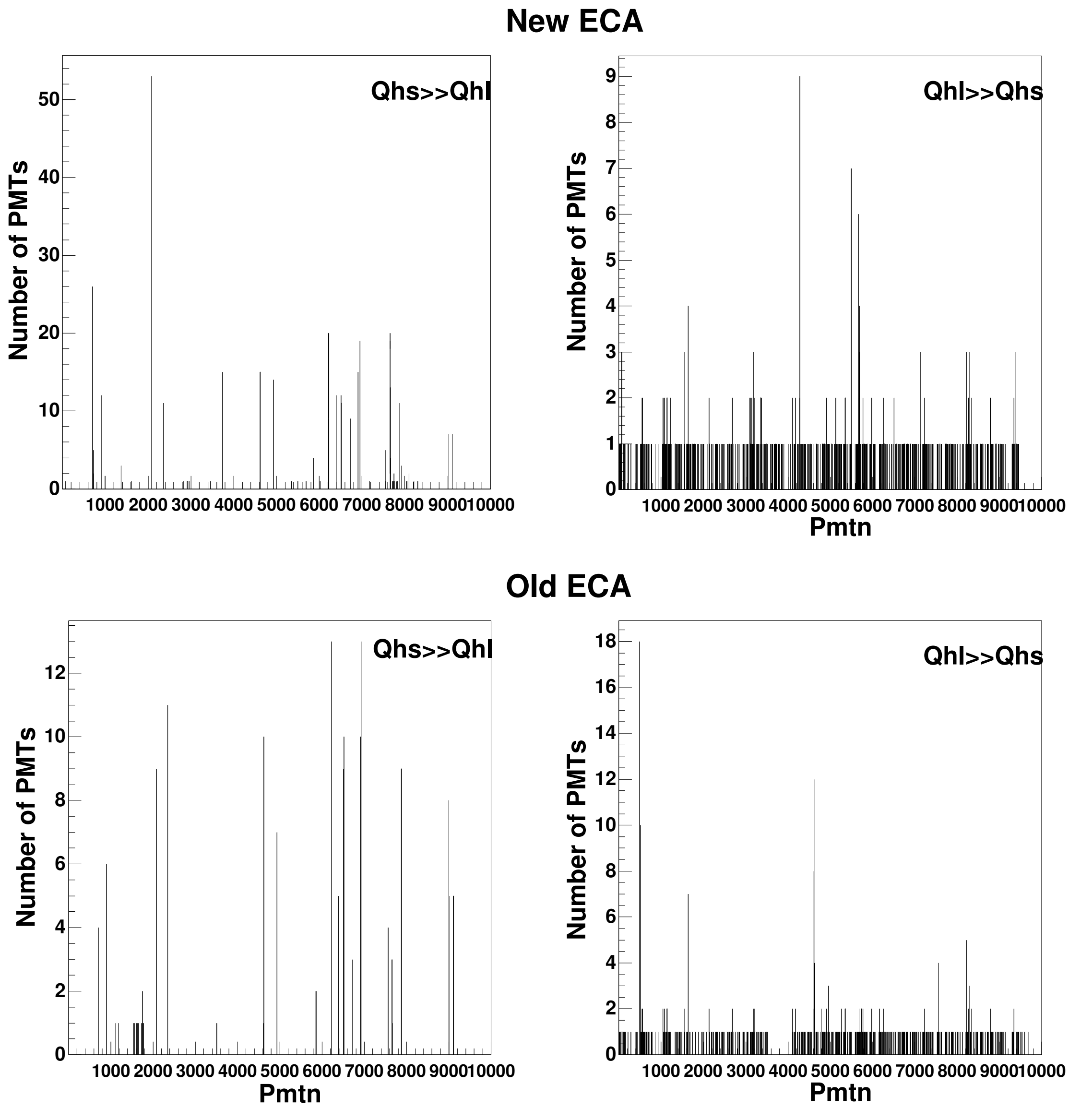

Figure 4.6: Histograms of PMTs with abnormal Qhs vs Qhl. Top - New ECA, bottom - Old ECA. Left - larger Qhs, right - larger Qhl.)

Qhl where it is possible for both direct and reflected light to be detected by the same PMT, therefore the occasional larger measurement of Qhl.

4.3 Qhl and Qlx

A second comparison, Qhl vs Qlx, has been done for the same events of the laser-ball run. Similar plots are made of the two different SNOMAN calibration methods.

In Figure 4.7 the new ECA calibration method was used. In the upper histogram, the single photon spectrum appears to have a broad peak for Qlx, with a sharp peak at 5 pe. There is poor agreement between the two charge measurements on the scatter plot. For comparison, in figure 4.8 the old ECA has been used. Again one can see that the charge measurements appear to be at a 1.5:1 ratio but there is much less scattering than the previous plot. In both plots there is poor agreement at low pe. This is likely due to the low gain nature of the Qlx, since the single pe peak is near the pedestal it is not expected to have very accurate resolution below about 10 pe.

4.4 Sono-ball

In order to rule out any effects that may be introduced by the laser-ball itself a similar comparison is done using the sono-ball [12]. This light producing calibration source has a small bubble at the centre of a water filled flask that is vibrated using piezoelectric transducers connected to the flask. The vibrating bubble emits light in a very sharp time peak (less than 100 ps) with a light spectrum similar to Cerenkov photons.

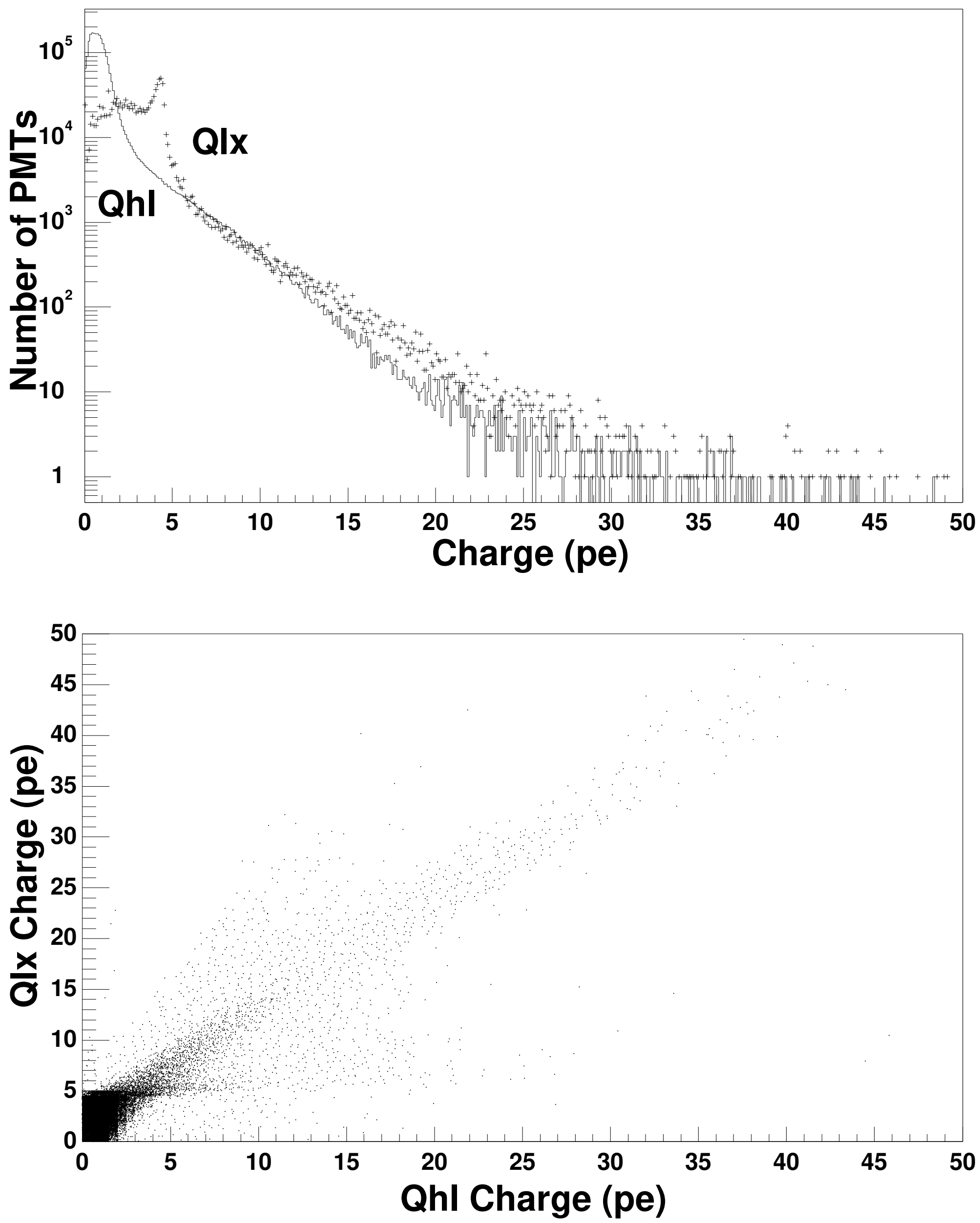

Figure 4.7: Qhl vs Qlx - Complete calibration, (New ECA)

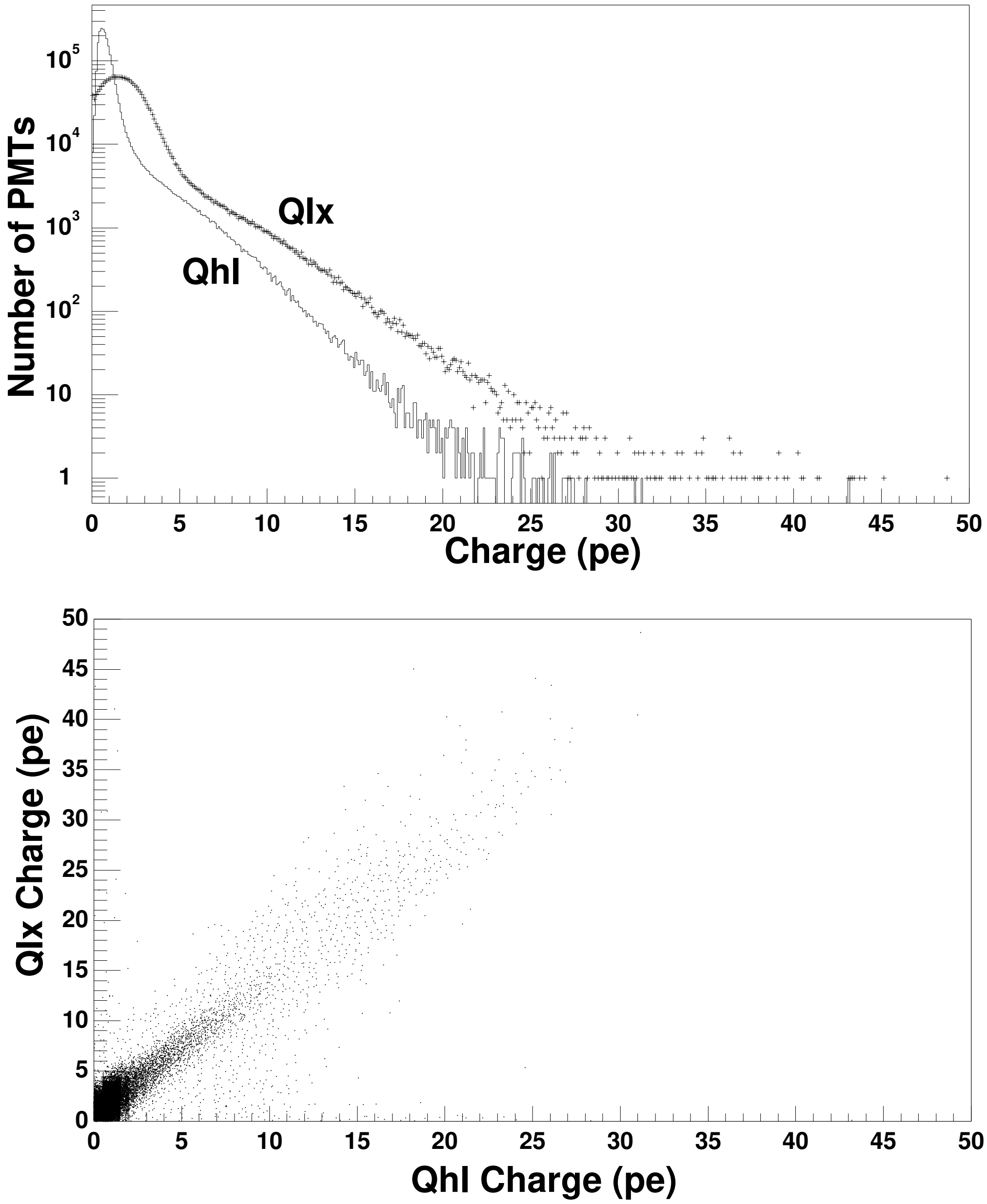

Figure 4.8: Qhl vs Qlx - Complete calibration, (Old ECA)

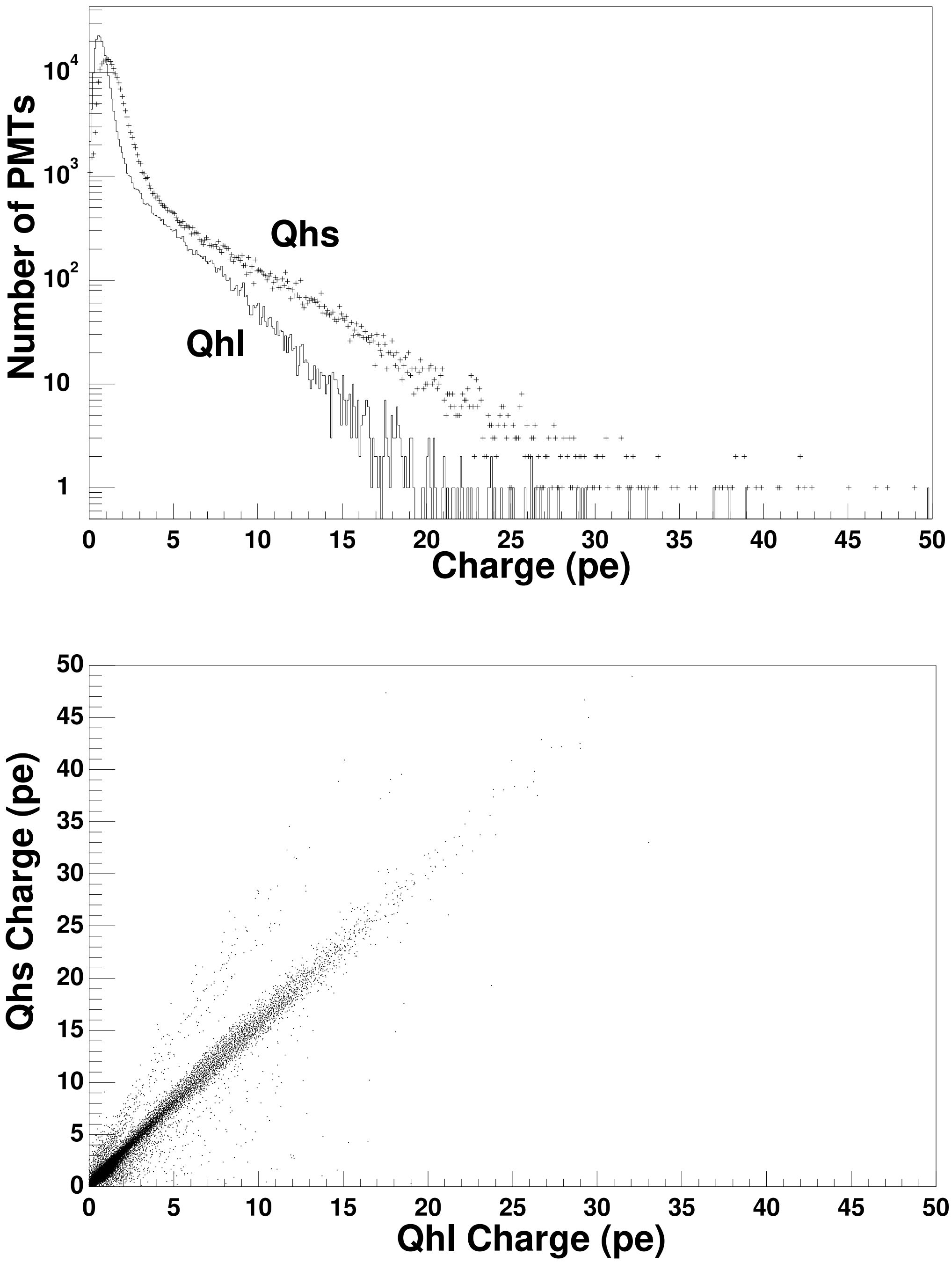

Figure 4.9: Qhl vs Qhs for a low intensity sono-ball run - complete calibration (New ECA).

There is a possibility of flouresence in the optical fibers that transfer the light from the laser to the diffuser ball. This would cause a broadened light output for several ns rather than the light being emitted in a relatively sharp time peak. This would not occur in the sono-ball since the light is created within the D_2O volume. The drawback to using the sono-ball is that the light intensity is much higher. In order to create a single photon spectrum the sono-ball was masked and small holes were made where the light could pass. Several bandpass filters were then placed in front of these holes in order to decrease the intensity of light. However this means that only a few PMTs were illuminated since the sono-ball did not move throughout the run and the hole where the light that emerges was always facing the same PMTs.

Sono-ball run 1268 was used. Most of the events occurred in about 110 PMTs with a few events for the others due to noise and reflected photons. Figure 4.9 shows the results of the run. Although there are subtle differences, the problems observed in the laser-ball run are evident here. The ratio of the Qhs/Qhl is still 1.5 and there are a significant number of charge measurements that are scattered away from the main set. The main set of values seems to have less of a spread, but this is likely due to having all the measurements from so few PMTs.

4.5 ECA Data

In figure 4.10 the data from run 996, a charge calibration run, is shown. In this run charge was injected on the capacitors and read by the ADCs. This is the type of data run that was used to find the charge slopes used to calibrate the laser-ball and sono-ball data in the previous plots. The top histograms show what was read when charge

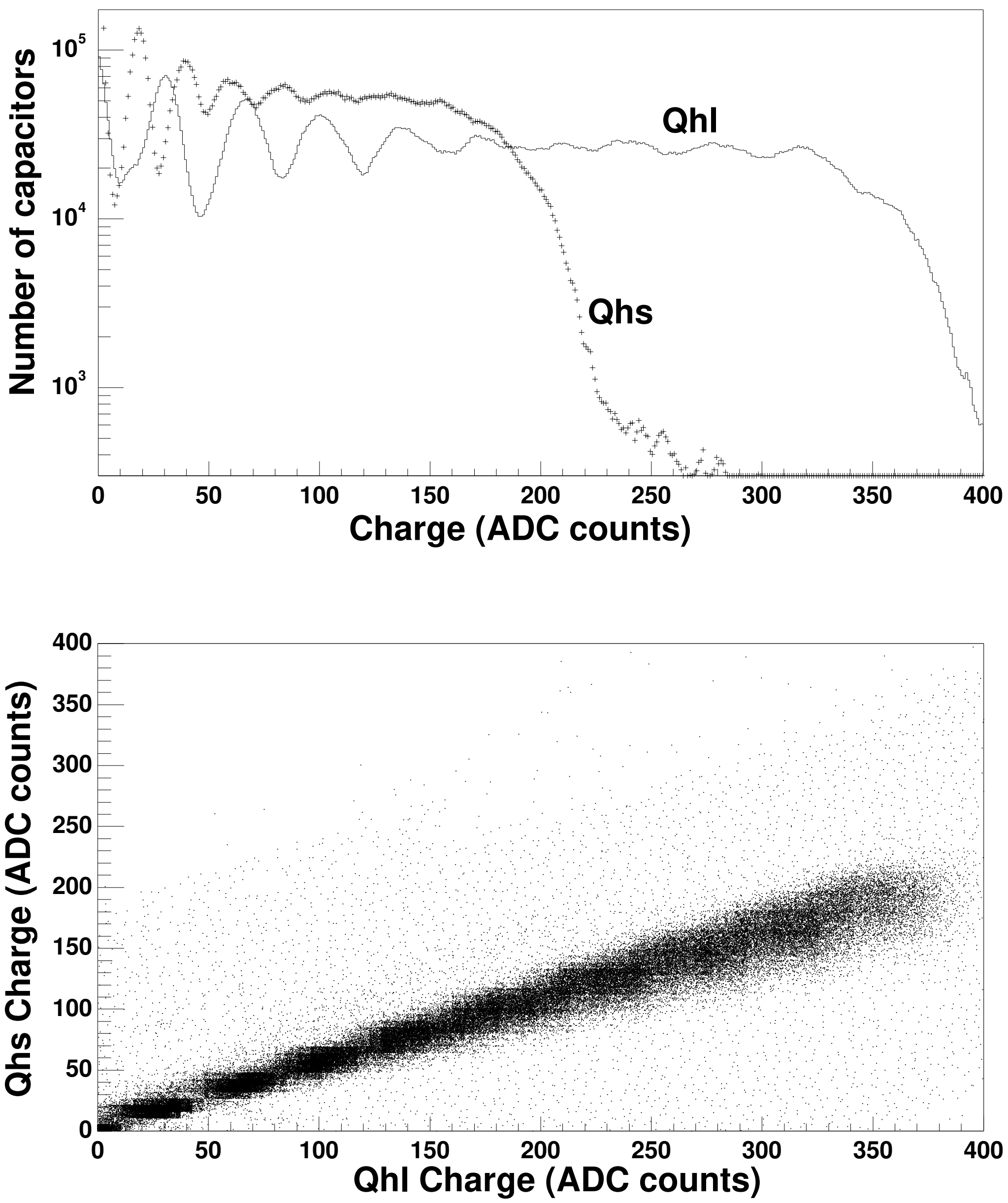

Figure 4.10: Qhl vs Qhs for ECA data - Pedestal Corrected (ADC counts)

pulses of different sizes were injected onto the capacitors. At lower ADC values one can distinguish between the different size of injected pulses. At large injected pulse size the resolution is much worse. It is not evident whether this is due to variations of the size of injected pulse or what the ADCs read.

On the scatter plot of Qhs vs. Qhl it is evident that the Qhs measurement is much lower than the Qhl measurement on an event by event basis. This would explain the Qhs to Qhl ratio of 1.5 in the previous data. During the calibration run the number of ADC counts per pC is much higher for Qhl than Qhs. Therefore if it is assumed that when measuring a real PMT pulse Qhl and Qhs are approximately the same (as was seen in the pedestal corrected single photon data in figure 4.1), after converting from ADC counts to pC Qhl will be much lower than Qhs.

It is not known why this discrepancy during calibration occurs, however one possibility is that the injected pulse is longer that 60 ns. If this is so, Qhs, which stops integrating after 60 ns, would only integrate part of the pulse while Qhl would receive the full pulse.

4.6 Summary

The analysis shows that the calibrations introduces a ratio of Qhs/Qhl of approximately 1.5 for single photon laser-ball runs. This discrepancy is introduced during the calibration step using charge vs ADC counts slopes found by injecting charge onto the storage capacitor and reading the values.

Events with a higher charge for Qhl than Qhs are likely explained by the longer integration time of Qhl. A second pulse from the PMT, from noise or light reflections, may be received by the electronics. What can not be explained is when Qhs has a much higher value than Qhl as can be seen in several plots in this chapter.

Qlx has similar problems but the severity depends on which SNOMAN calibration code is used.

Finally the sono-ball run was looked at to rule out any effects the laser-ball may have introduced. Although the sono-ball was focussed on only a small subset of the PMTs, indications are that the discrepancies between charges are not limited to the laser-ball events.

Finally it was shown that there is a discrepancy between Qhl and Qhs for the data used to calibrate the charge slopes of the capacitors.

The results of this chapter has lead to the development of an alternate method of charge calibration that does not use charge injection but instead uses various intensities of light output from the laser-ball in order to calibrate charge.

5 Charge Calibration using Nitrogen Laser System

In the previous chapter it was shown that the current method of charge calibration results in a large discrepancy between different charge measurements of the same photo-multiplier event. It is still unknown why this discrepancy occurs and has prompted an alternative method of charge calibration.

Charge calibration using the laser-ball can be done by using Poisson statistics to calculate the average number of photoelectrons detected in each PMT per event. By altering the intensity of the laser-ball, thereby altering the expected number of pe per PMT, a photo-electron vs. ADC count calculation can be made.

Laser-ball runs 996 to 1006 from August 8th, 1998 will be used in this analysis. The data was taken before filling the detector with water and using a light wavelength of 386 nm with the laser-ball near the center of the detector.

5.1 High Intensity Runs

Neutral Density Filters

The intensity of the laser-ball is varied by using several neutral density (ND) filters in series. The intensity of light through a neutral density filter is defined as I $=$

$I_0 10^{-ND}$ where ND is the neutral density of the filter used for the run. The initial intensity, I_0, is unknown for the laser-ball but by using the occupancy of the detector for low intensity runs a calibration of the expected number of detected photo-electrons can be made for any neutral density.

For each laser event pedestal corrected Qhl was summed for all PMTs and the mean value for each run was found. This mean value, in ADC counts above pedestal, is plotted against the neutral density of the filters used for the run and is shown in figure 5.1. This is a way of comparing average total detected charge for each neutral density filter setting. The fit line is $I = I_0 10^{-ND}$ and is fit to the three highest ND filters. It is obvious that the neutral density filters are not calibrated correctly. Several filters were combined together to create the ND values quoted, however these values were never meant to be an absolute value but rather a rough guide for the operators when running the laser. Therefore the ND values can not be used to gauge light intensities from the laser-ball.

However the laser-ball has a small PMT inside it that was not yet operational at the time of these runs and can be used in the future to calibrate the overall intensity of each ND setting. This would remove any questions of the calibration of the neutral density filters and possible inconsistencies in the laser output from run to run. But for now the only way of determining the number of pe/PMT is by using the relative occupancy (the fraction of operational PMTs that fire in each laser event) of the run.

Expected Number of Photo-Electrons per Laser Event

A calculation of the number of photo-electrons per PMT per laser event must be made in order to compare to the measured ADC count for that run. From this a

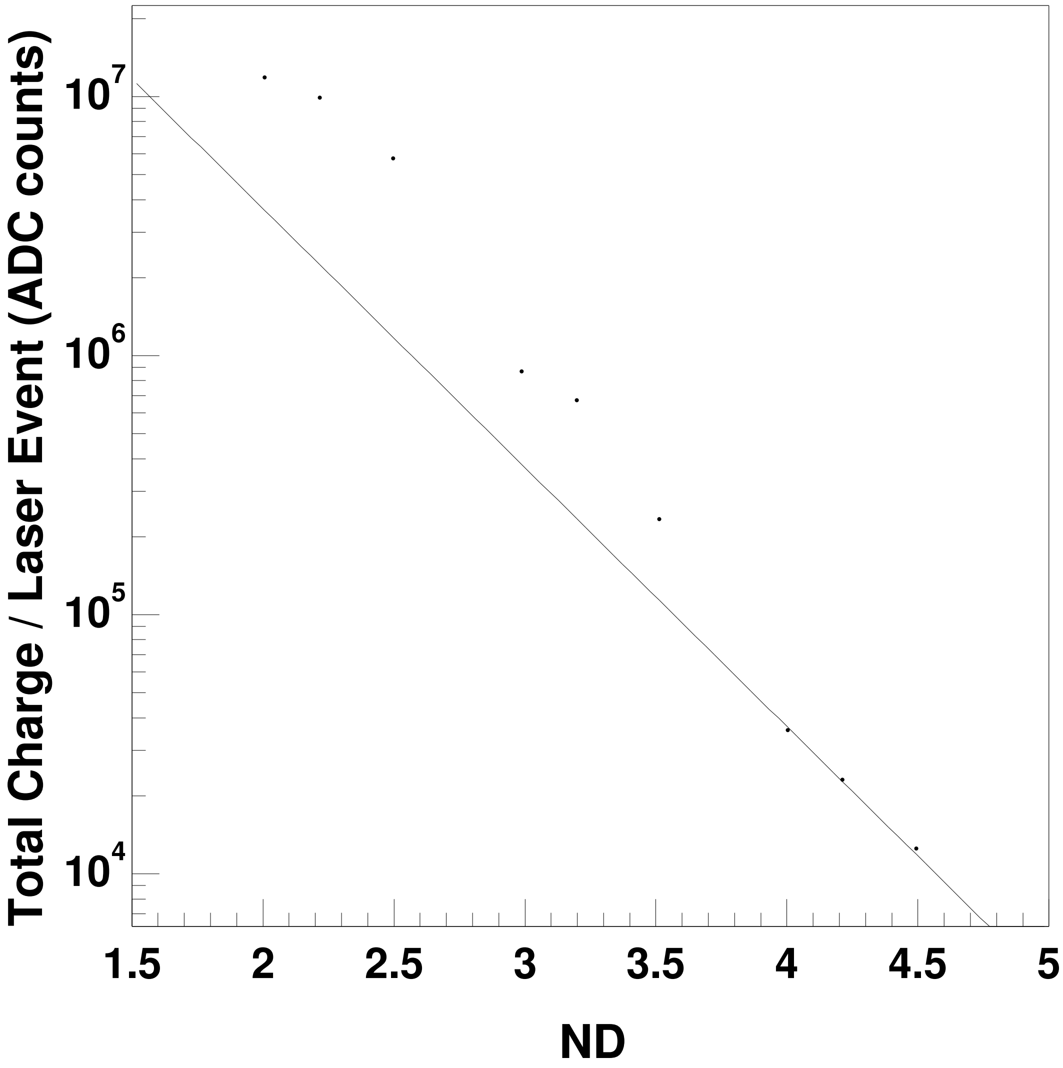

Figure 5.1: Mean summed Qhl (pedestal corrected ADC counts) per laser event vs. neutral density.

slope of ADC vs. number of pe can be made for each PMT. At the time the data was taken there were approximately 8500 functioning channels online. To determine this, a low intensity run was used to find a mean number of times that a PMT fires. A PMT had to have been triggered at 50% or more of the mean rate. This keeps the PMTs that are off-line and may have triggered the discriminator only a couple of times due to noise pickup from being included in the total.

Poisson statistics may be used to calculate the number of photons that each PMT is expected to detect in an event. Using the mean Nhit for each run a relative occupancy for each run can found.

The general Poisson equation states that if the average result of all trials in a random distribution is μ, the probability of getting a value of n in any single trial is:

$$P(n, \mu) = \frac{\mu^n}{n!} e^{-\mu}. \tag{5.1}$$

In this analysis μ is the average number of photo-electrons detected per PMT per laser event and n is the number of photo-electrons detected (0, 1, 2, ...) any time that a PMT fires.

In order to solve for μ it us useful to use the number of PMTs that did *not* get hit by photons since the fraction of active tubes that did not fire reduces to the following equation:

$$P(0, \mu) = 1 - \frac{<Nhit>}{Ch} = e^{-\mu} \tag{5.2}$$

where $< Nhit >$ is the average Nhit for the run and Ch is the number of active channels for the run (8500 PMTs). Then from this the number of pe/PMT when the

PMT *does* fire (μ_f) is found by the equation:

$$\mu_f = \frac{\sum_{n=1}^{\infty} \frac{\mu^n}{n!} e^{-\mu} n}{\sum_{n=1}^{\infty} \frac{\mu^n}{n!} e^{-\mu}}. \tag{5.3}$$

Due to the high setting of the PMT discriminators, approximately 0.5 pe [17], there will be many instances where a photon hits the PMT but the PMT does not fire. Since the pulse measured for a single photon can range from 0 to several photoelectrons due to statistical fluctuations during electron multiplication in the dynode structure, many single photon events can produce a pulse that is not detected because it is below the discriminator threshold. This is much more likely to happen at low intensity since if the mean number of pe per PMT in an event is ~ 5 or so, it is unlikely that the pulse will fail to pass the discriminator threshold. Therefore the probability that a tube does not fire becomes a sum of the probability that the PMT does not get hit by a photon plus the probability that if it does, the resulting pulse is not large enough to fire the discriminator:

$$P(0,\mu') = 1 - \frac{<Nhit>}{Ch} = e^{-\mu'} + P(1\rightarrow 0)\cdot \mu' e^{-\mu'} \tag{5.4}$$

where the second term on the right hand side of the equation is the Poisson term for a single incident photon multiplied by $P(1\rightarrow 0)$, the fraction of those pulses that will not pass the discriminator threshold.

In order to calculate $P(1\rightarrow 0)$ the charge height spectrum is approximated to be a Gaussian. In order to find μ', μ found using equation 5.2 is used. The value of σ is found by fitting a Gaussian to the charge spectrum in each run and can be expressed relative to μ (i.e. for run 996, $\sigma = 1.3\mu$). From this we get the fraction of events that are below the PMT trigger thresholds:

$$P(1\rightarrow 0) = \frac{1}{\sigma\sqrt{2\pi}}\int_0^{0.5} e^{-\frac{1}{2}(\frac{x-\mu}{\sigma})^2}dx \tag{5.5}$$

After finding the values for μ and $P(1\rightarrow 0)$ we are then able to find a value of μ' for each run by using these constants in equation 5.4 and numerically solving for μ'.

Two things should be noted at this point. First, this compensation for high discriminator settings is done for a single photon creating a pulse but not firing the discriminator. Since there is the possibility of more than one photon in a single PMT in these runs, there is also a possibility of a double photon (or triple, etc) producing pulses that do not fire the discriminator. But as the number of incident photons increases there is less chance that the resulting pulse will be below the discriminator threshold, so the correction terms for more than one photon striking the tube and not firing the discriminator become less important and have not been included (i.e. $P(2\rightarrow 0) \sim 0,\ P(3\rightarrow 0) \sim 0, \ldots$).

The second point is that this is actually an iterative process. We use μ to calculate $P(1\rightarrow 0)$ and use these values to find the more precise value μ'. From this μ' should then be used to recalculate $P(1\rightarrow 0)$. However subsequent corrections will be much smaller so only the first order correction needs to be applied here.

A summary of all the constants and corrections used is displayed in the following table. The constants are those that have been previously defined except for μ'_f which is the mean number of pe detected per pmt per laser event when a pmt fires for the various runs.

Run	ND	$<Nhit>$	μ	μ_f	$P(1\rightarrow 0)$	μ'	μ'_f
996	4.5	328	.040	1.02	13%	.045	1.02
997	4.2	599	.073	1.04	13%	.084	1.04
998	4.0	940	.115	1.06	13%	.132	1.07
999	3.5	4452	.752	1.42	10%	.832	1.47
1002	3.2	7490	2.13	2.39	6%	2.44	2.58
1003	3.0	7995	2.82	3.07	4%	3.16	3.25

Table 5.1: Values used to find number of expected photo-electrons per PMT.

5.2 Charge Slopes

For each run the average pedestal corrected ADC count was calculated for each PMT. PMT events which were above 4000 raw ADC counts or below -300 pedestal corrected ADC counts were cut from the data to remove non-physics events. Data files of each run were created with the average charge ADC count and σ for each pmt. The average ADC count was plotted vs. the calculated expected pe for the six runs described in the table above and a straight line was fit to the data. From this the slope and offset of the line were used to convert from ADC counts to photo-electrons.

A typical example of the calibration is for the PMT in crate 0, card 0, channel 1 (shown in figure 5.2). Only statistical error is shown on the graph and the fit line is $ADC = slope \cdot pe + offset$. Histograms of the results of the calibrations for all PMTs are shown in figure 5.3. Each PMT has 1 entry included in each histogram. There is one set of calibrations for each charge type; Qhl, Qhs, and Qlx. The top left plot

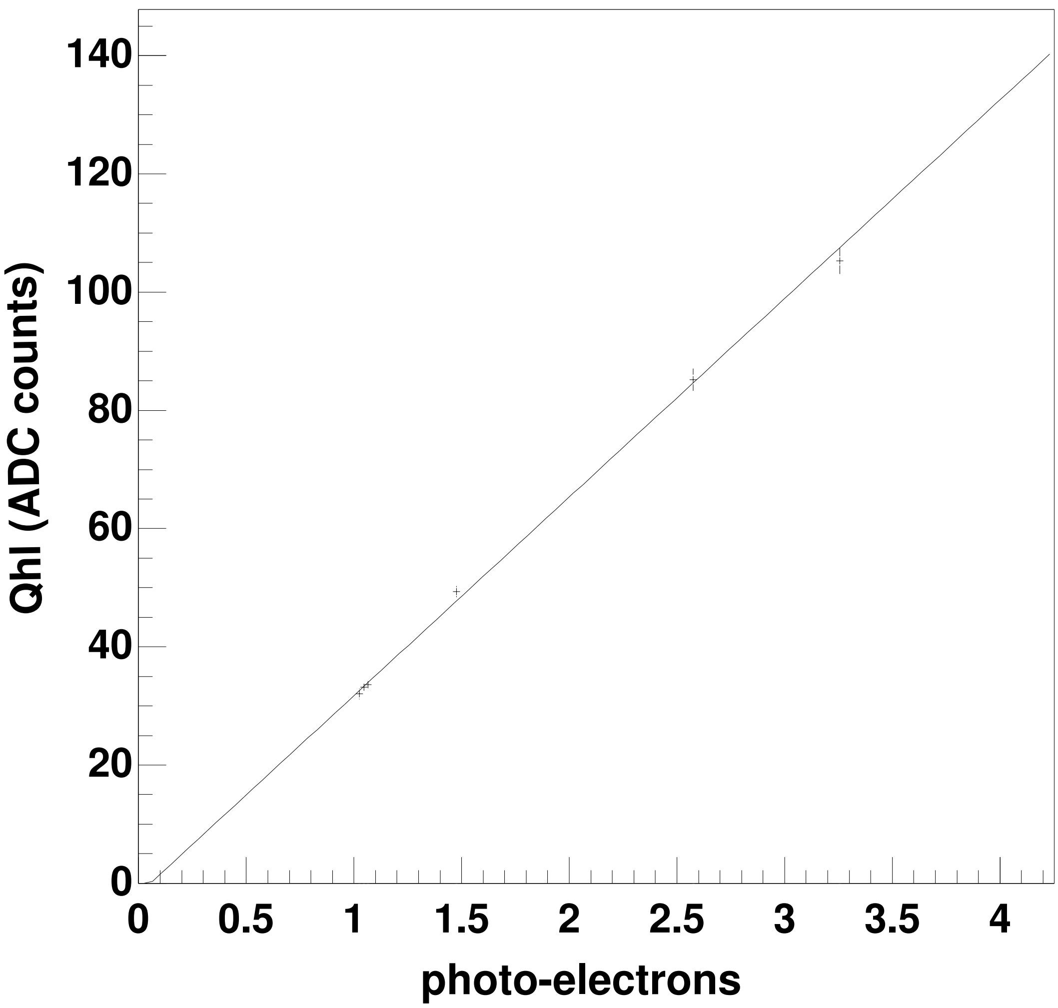

Figure 5.2: Sample charge calibration slope for a typical PMT in SNO.

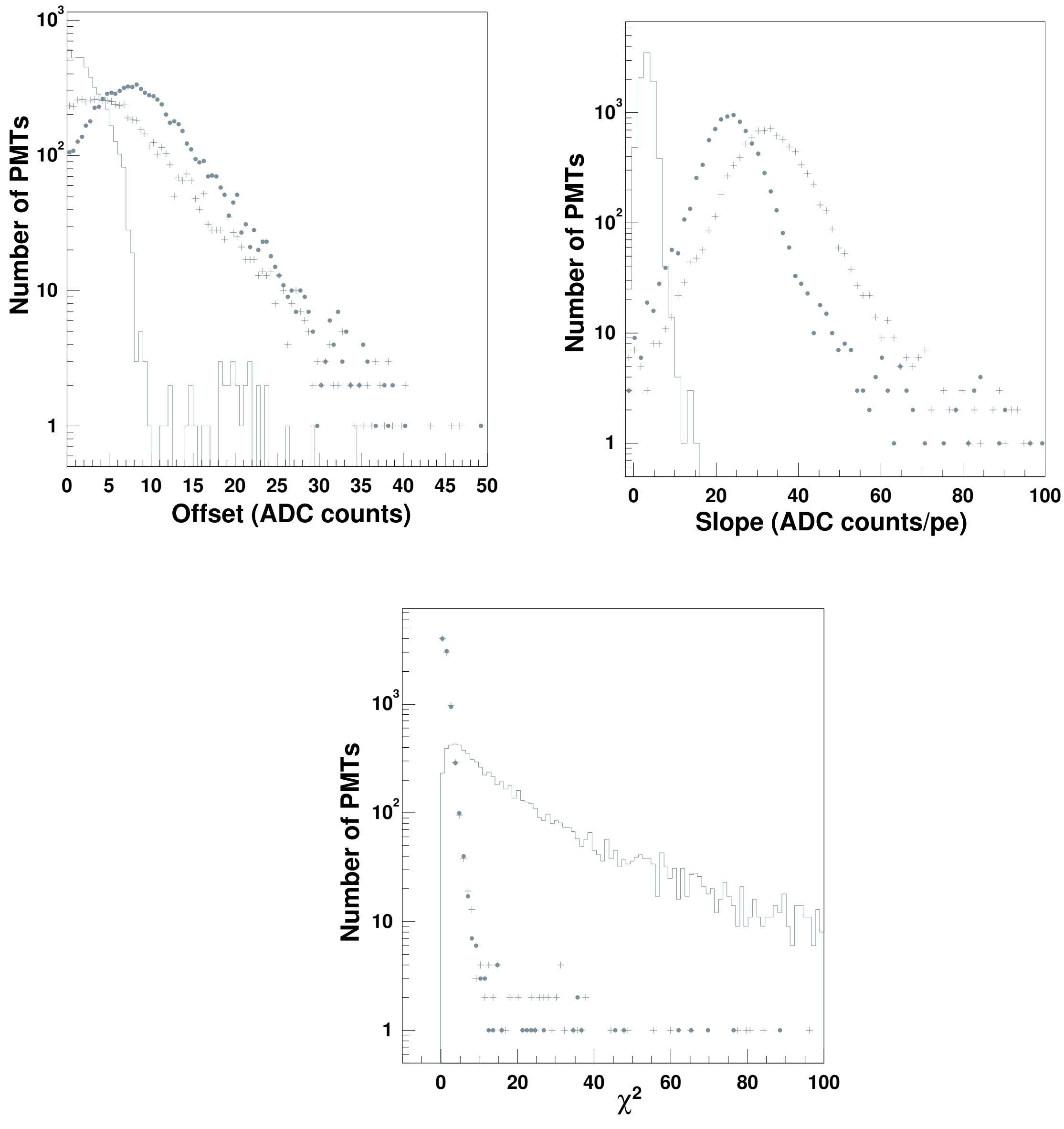

Figure 5.3: Histograms of the PMT charge calibration offsets, slopes and χ^2. There is one entry in each histogram for each PMT. Qhl - crosses. Qhs - dots. Qlx - solid line.

shows the offsets of the 3 different charges and the top right displays the slopes. The bottom histogram show the χ^2 per degree of freedom of the fits.

Although the χ^2 of the fits are excellent for Qhs and Qhl, with a steep drop off even on a log plot, the fits are not nearly as good for Qlx. Each PMT has 48 storage capacitor cells, 16 for each high gain measurements and 16 for the low gain measurements. For this calibration, measurements of the pedestal values were subtracted from the raw ADC values before the slope fits were made, and this pedestal correction was done on a cell by cell basis. For the high gain capacitors, variation between cells is minimal compared to the variation in gain from PMT to PMT therefore it is unnecessary to do the slope calibration for each cell and an average calculation is done for the 16 storage cells in each PMT. However since the gain for Qlx is much lower than Qhl and Qhs, it is much more sensitive to the small cell by cell variations and to properly calibrate it a slope calibration must be done for each cell. However this was unnecessary at this time since the main focus of this thesis and other analysis relies on the high gain charges.

When fitting a line to the data both a slope and offset are found. An offset would seem to be unnecessary since the pedestal has already been subtracted from this data, therefore zero ADC counts should equal zero pe. However it was later found that there was problems with the electronics. Charge is injected onto the storage capacitor at a steady rate to compensate for voltage drooping over time so that overall the voltage is constant. For some runs the wrong values of the injected charge rates were loaded into the electronics by the data acquisition software which would explain the slight shift of the pedestal values. This problem has since been corrected and any calibration done after the commissioning stage should have slopes that pass through zero. This is not expected to result in a large error since the offsets are on the order of 1/4 of a pe.

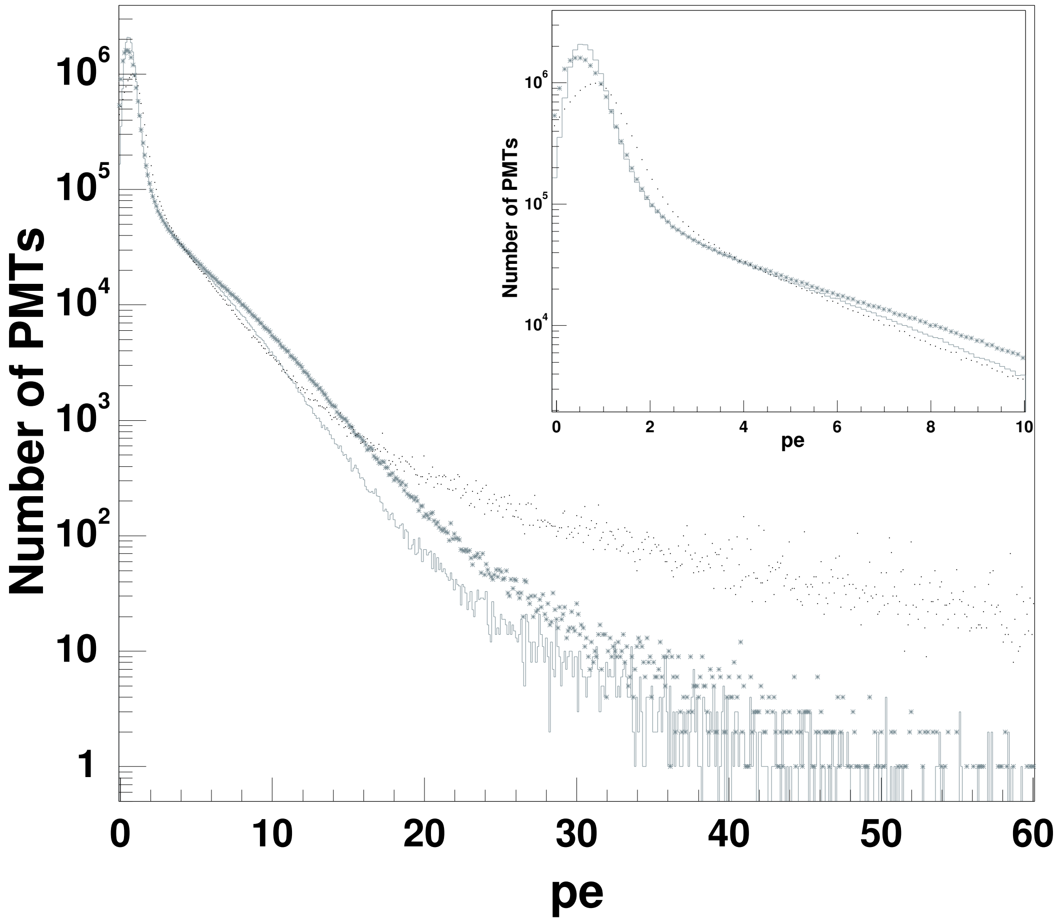

Figure 5.4: Calibration of run 998 with current charge calibration. The histograms are Qhl (line), Qhs (stars) and Qlx (dots). Inset is an enlargement of the low pe section of the spectrum.

In figure 5.4 a plot of the single photon laser-ball run 998 using the new charge slope calibration is shown. There is a sharp decrease of the χ^2 up to a value of 10 for

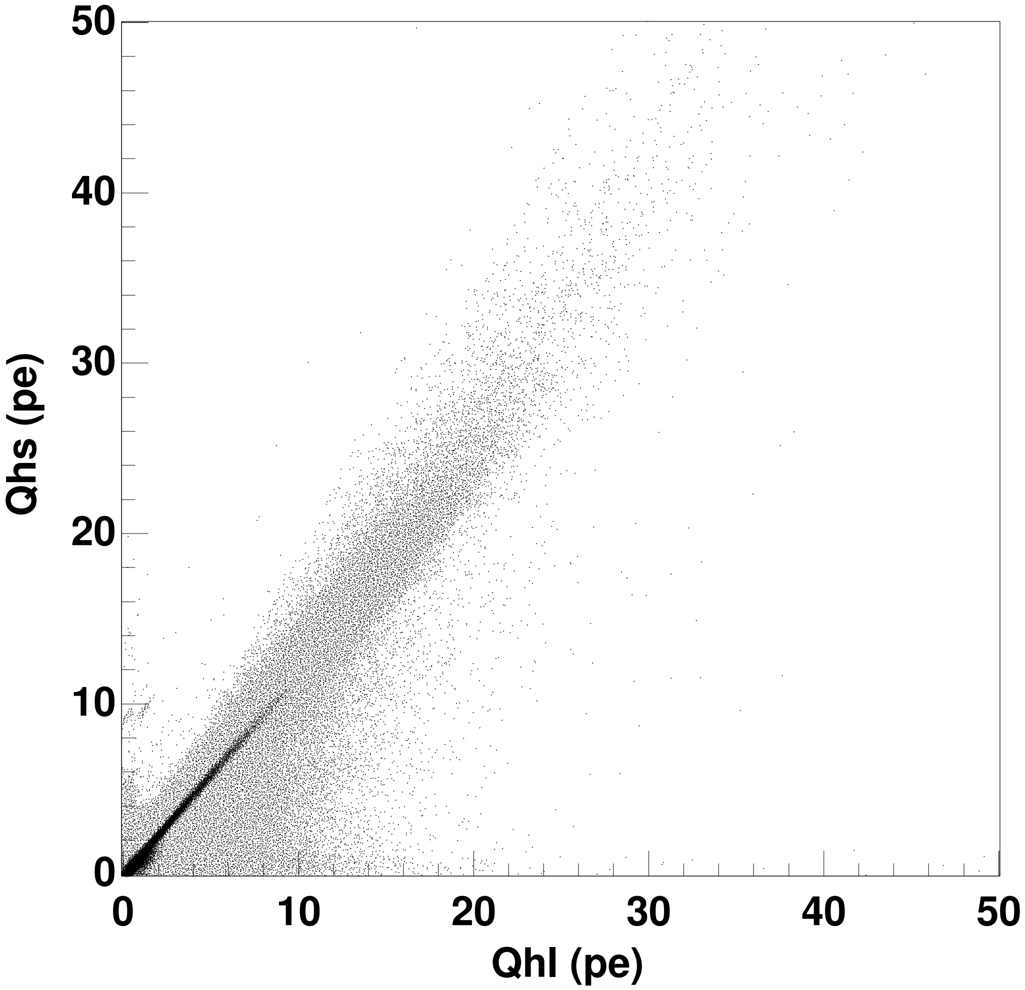

Figure 5.5: Scatter plot of Qhl and Qhs calibrated with current calibration method.

PMTs.

The pulse height spectra for the high gain charges have single pe peaks that match very closely and a small discrepancy between the high charge tail, but much less than is introduced by the calibration methods discussed in chapter 4. Despite the poor fits for Qlx and high tail of the charge spectrum, the single photon peak has much better resolution than previous methods of charge calibration. A scatter plot of Qhl vs. Qhs is shown in figure 5.5. There appears to be much more scattering than previous calibration methods but the ratio of the bulk of events is much closer to 1:1.

5.3 Discussion

This method of charge calibration results in Qhl and Qhs spectra that match each other much more closely than those in chapter 4. Also the single photon peak for Qlx is much sharper. Up to this point only statistical error has been taken into account and systematic errors must be investigated.

A systematic uncertainty that must be looked into is variation in the intensity of light received by the PMTs. Generally the laser-ball is an isotropic light source [17] and with the laser-ball in the centre of the detector all PMTs in the PSUP should receive the same amount of photons. Measurements of the laser-ball light intensity near the neck of the diffuser ball is lower which may cause a lower than expected average ADC count for PMTs directly above it. A scatter plot of the calibration slope vs. height of the PMT in the PSUP is shown in figure 5.6 where zero is the centre of the PSUP. PMTs at the top of the PSUP do seem to have slightly lower slope values than the mean. Also there are other patterns such as several PMTs with

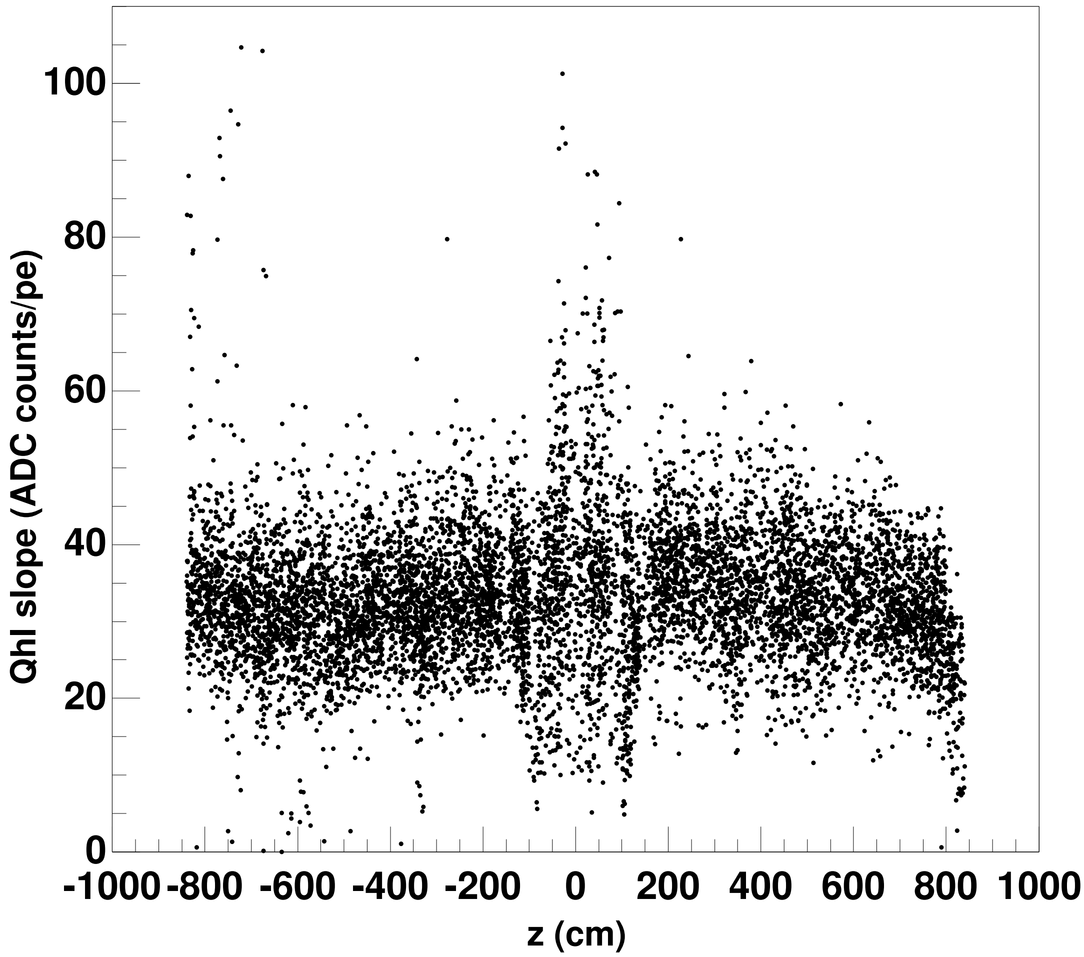

Figure 5.6: Qhl slopes of each PMT vs the PMT height relative to the centre of the PSUP.

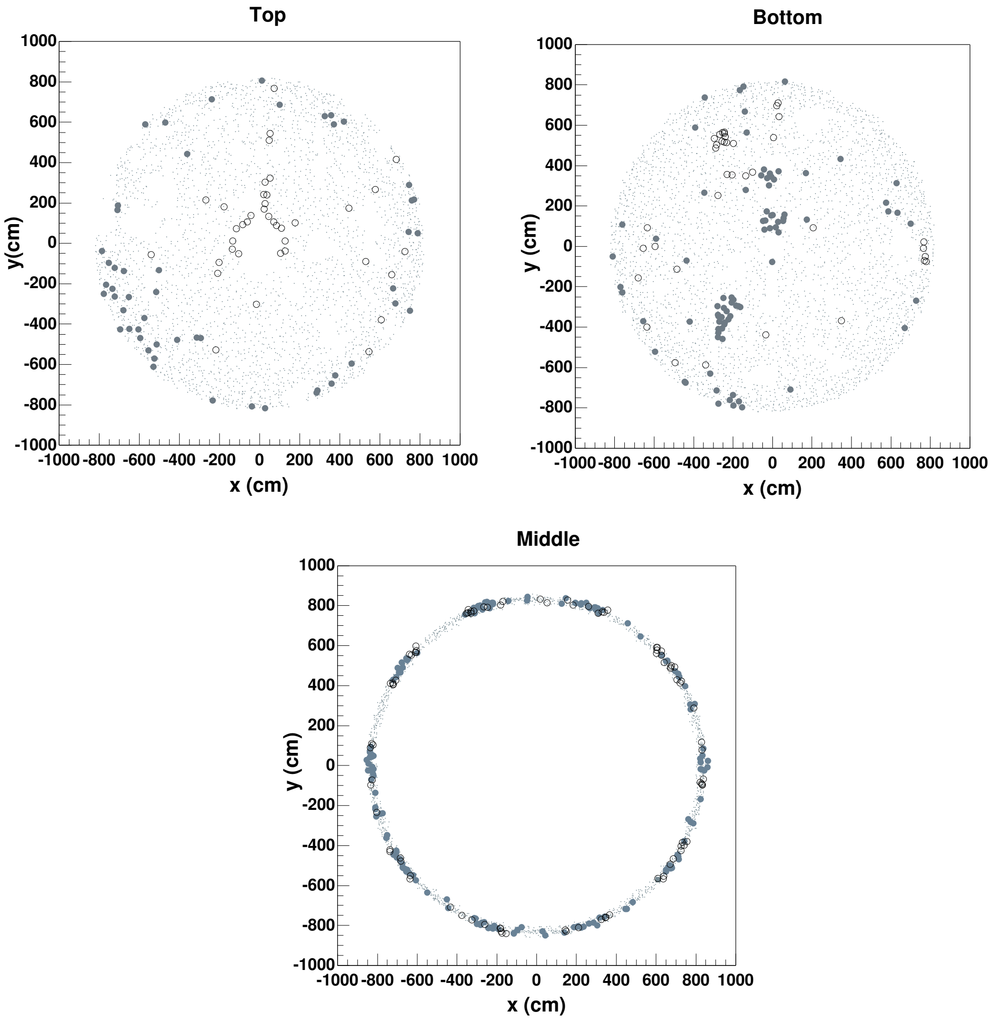

Figure 5.7: X-y scatter plots for PMTs in PSUP. The PSUP is split into 3 regions; $z > 200$ cm (upper left plot), $z < -200$ cm (upper right plot) and $-200cm > z > 200$ cm (lower plot). Each calibrated PMT is represented by a small dot. Those PMTs with Qhl slope>50 ADC counts/pe are shown as filled circles and those with slope<15 ADC count/pe are open circles.

high slopes at the bottom of the PSUP and both high and low values near the centre.

Figure 5.7 shows the slopes of PMTs at the top, bottom, and central parts of the PSUP. The upper left plot is a PMT x-y scatter plot for all PMTs that were calibrated for $z > 200$ cm. Each PMT is represented by a small dot. Those PMTs with Qhl slope>50 ADC counts/pe are shown as filled circles and those with slope<15 ADC count/pe are open circles. One can see a hole in the centre where there are no tubes present and this corresponds to the opening in the PSUP for the neck of the acrylic vessel. Around this opening there are several PMTs that have low slopes. This can presumably be attributed to these PMTs receiving lower light intensities due to either a shadow caused by the neck of the laser-ball or by reflections off the neck of the acrylic vessel.

The upper right plot of figure 5.7 shows PMTs for $z < -200$ cm. There are a few areas where the PMTs have either low or high gains. When the PMTs were installed in the PSUP and electronics crates they were placed in groups of PMTs with similar characteristics. A resistor was then placed on each FEC for the high voltage supplied to the PMTs so that PMTs on each FEC had approximately the same gain. Gain matching was then taken further by individual resistors for each PMT high voltage cable. If the resistor on the FEC is incorrect the gain will be higher or lower for all the PMTs on that FEC than the other PMTs in the detector. For $z < -200$ cm PMTs in crate 6, FEC 0 is the cause of most of the low gain tubes and PMTs in crate 4, FEC 1 and crate 11, FEC 1 have much higher gain than the others for both Qhl and Qhs.

The centre of the PSUP is displayed in the lower plot. There are 10 areas spaced quite regularly around the equator that have high and low slope values. The low slopes correspond to PMTs that are shaded by the 10 suspension ropes for the acrylic vessel. The ropes suspend the AV by passing though grooves in plates around the equator. The 10 plates are thicker than other sections of the AV and so are beveled to match the thinner pieces. This beveling results in optically focusing the light on some PMTs around the equator of the PSUP. This would explain the 10 regions of high slopes in the centre of the PSUP.

All PMTs used in the detector first went through single pe charge and time spectrum tests done at Queen's University [18]. The tests were done using a nitrogen dye laser system with light at a wavelength of 386 nm. A gain and pedestal measurement was done for the PMTs.

Several of these test spectra were selected and summed together after converting the data to units of photoelectrons. This is compared to the Qhl charge spectrum from figure 5.4 and is displayed in figure 5.8. The tests at Queen's University were done using a trigger created by the laser when it fired. This trigger fired the discriminator and since the PMT occupancy was about 3% for these tests most of the data in this histogram is a pedestal measurement. However in the detector the PMT discriminator settings were set at approximately 0.5 pe so most pulses with a pulse height below 0.5 pe are not included in the data. This explains the the difference between the two spectra below about 1/2 pe. Above 1 pe the charge spectra are quite similar, up to the limit of Queen's test apparatus of about 7.5 pe.

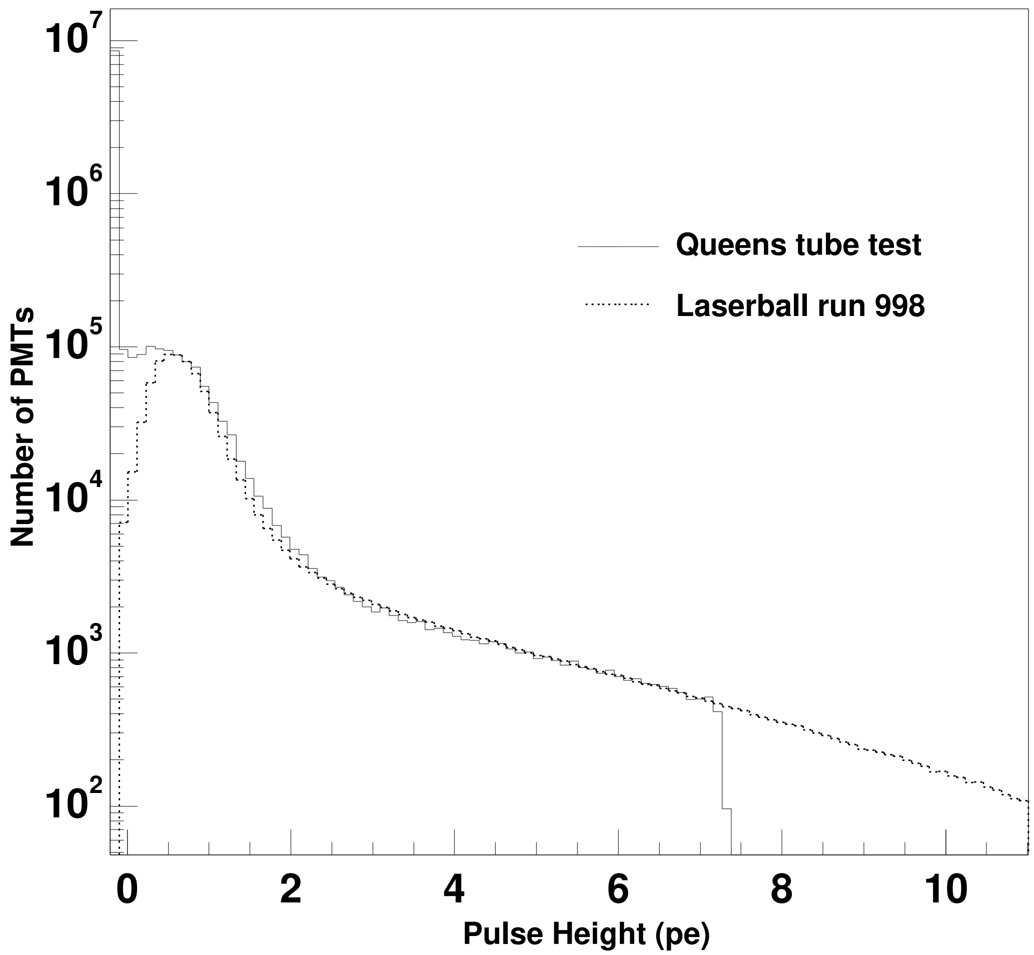

Figure 5.8: Comparison of tests done on SNO PMTs at Queen's University to the Qhl spectrum of the SNO detector.

6 Large PMT Pulse Events

In this chapter an analysis of events with large PMT pulse height are investigated, with the purpose of understanding how the SNO photo-multiplier tubes react to charged particles in the PMT glass envelope. This is done with the expectation that large PMT pulses will aid in identifying PMT $\beta\gamma$ events in the data.

6.1 Photo-Multiplier Tube Radiation

Although the PMTs, including the glass, have been made with materials containing low concentrations of radiation-producing elements, they are still expected to be the largest source of background inside the PSUP. Even at only $3 \cdot 10^{-8}$ grams of Uranium and Thorium per gram of glass, this is by several orders of magnitude the highest concentration of radiation source of any of the materials used to build the detector.

Many of the decays in the U and Th chains emit a β particle followed by the emission of high energy γ rays. To shield the heavy water, 2.5 m of light water separates the D_2O from the PMTs. The γ ray may enter the light water between the PSUP and AV where the γ ray has a mean path length of 25 cm before it interacts with a particle.

If the γ has a mean energy larger than the photo-disintegration of the deuteron, 2.2 MeV, a γ that enters the heavy water may produce a free neutron, as in the neutral current neutrino interaction.

If, however, the γ ray Compton scatters, the resulting electron can produce Cerenkov radiation similar to an electron in a charged current neutrino interaction. In order to identify these events in the neutrino data a fitter algorithm uses the PMT-s' location and the relative times that they fire to reconstruct where the event took place. Any events that reconstruct outside the AV are removed from the neutrino data as background radiation. However, there is an uncertainty in the reconstruction fitter due to such things as reflections and random PMT noise which may cause a small fraction of the γ rays to be reconstructed inside the AV.

Since these γ rays are below the expected threshold of the detector (about 5 MeV) it has been calculated that they will not be a background to the neutrino signal (see figure 3.5). However it has not been verified experimentally that the energy resolution of these background events does not have a tail that goes up to or higher than 5 MeV.

Due to the relatively high concentration of U/Th in the PMT glass, even a small fraction of mis-reconstructed PMT $\beta\gamma$ events, or PMT $\beta\gamma$ creating deuteron photo-disintegration, could potentially be a significant background to neutrino detection.

There may be a way to identify these background events. There have been Monte Carlo studies of charged particles in PMT glass that suggest that the PMT β particles can produce large pulses in the PMT. According to SNOMAN Monte Carlo simulations [19], no more than 0.0165% of 5 MeV electrons that were distributed evenly in the heavy water produced more than a 5 pe pulse in any PMT. A Monte Carlo simulation of PMT $\beta\gamma$ decays started in the PMT glass was also made. Of those that caused an event with Nhit greater than 10, 23% of the events produced a pulse height more than 5 pe in the source tube. This could potentially be a way to identify PMT $\beta\gamma$ events.

In previous chapters it has been shown that single photons may produce a very large PMT pulse. It must be found at precisely what pulse height it would be most efficient to identify PMT $\beta\gamma$ background radiation without affecting the neutrino data.

6.2 Background Radiation during Air-fill

A method of examining PMT pulse height is by using the PGT. This periodic trigger samples the detector at a set rate. A GT is sent out to the detector at a rate of 5 Hz. Before the detector was filled with water most of the data collected was from backgrounds; PMT noise, photons from α particles (from radon decay) scintillating in air, Compton scattered electrons in PMT glass, and PMT βs.

To compare the PGT data to Monte Carlo simulations the expected rates at which these background events occur must be determined. Since it is the PMT pulse height spectrum that we want to investigate, the types of interactions in the PMT can be split into two categories - those that create single pe pulses and those that create multi-pe pulses. We will start by discussing charged particles in glass that are expected to produce the large pulses.

PMT β Particles

High energy β particles are emitted in nuclear decays throughout the U and Th decay chain [31]. Only β particles which have energy endpoints greater than 200 keV will be discussed since we are only interested in relativistic charged particles that create Cerenkov radiation in glass. Below 200 keV the electron in glass does not create Cerenkov radiation. There are 3 high energy βs released in the ^{238}U chain with β energy endpoints as high as 3.26 MeV. A ^{232}Th atom produces 4 high energy βs throughout its decay chain with a maximum β endpoint of 2.25 MeV.

The glass envelope and neck have an average of 18.0 μg of each Th and U [16]. Taking into account the decay rates of U and Th, and assuming that they are in secular equilibrium, the number of decays for the respective chains are 17788 $(g\ U)^{-1}s^{-1}$ and 5879 $(g\ Th)^{-1}s^{-1}$. After including the number of high energy βs for the respective chains, this results in a high energy β emission rate of 1.38 $PMT^{-1}s^{-1}$ from the glass envelope.

Another source of radiation in the glass is the isotope ^{40}K. There is a low energy γ ray in 10% of the decays which is not expected to affect the neutrino signal. However in 90% of the decays a β with an endpoint energy of 1.35 MeV is emitted without a γ ray. The glass used to make the PMT envelope contains 2.8% potassium [23] and the ^{40}K isotope occurs naturally at an abundance of 0.117% [31]. This results in a β production rate of 662 $PMT^{-1}s^{-1}$, by far overshadowing any high energy particles in the glass contributed by the U & Th chains.

The pin-out glass was not made under the clean conditions of the glass envelope and so has a relatively higher amount of contamination. Since it is optically visible by the photo-cathode, βs in this glass must also be considered. Since Cerenkov photons from these βs will be partially blocked from the photo-cathode by the dynode, they must be considered separate events from the glass envelope β decays. However, a Monte Carlo of 100,000 ^{208}Tl $\beta\gamma$ decays started in the pin-out glass of a PMT resulted in the PMT firing from only 567 of these events, and the resulting spectrum was a single pe spectrum. Therefore pin-out βs can be dismissed as a negligible source of large pulse events in the PMTs.

Rock Wall γ Rays

During commissioning, before the detector was filled with water, the PMTs were exposed to the γ rays from the rock wall. The γ rays were able to interact with electrons in the PMT glass. Since the γ rays from the rock wall have a spectrum that extends above 8 MeV many will be able to produce Compton electrons in the PMT glass that are above the threshold of Cerenkov radiation emission. These electrons are expected to produce a PMT pulse similar to PMT βs.

Measurements of γ ray fluxes inside the cavity have been made [20]. The majority (99.8%) of γ rays from the rock wall are below 3 MeV. The high energy γ rays are mainly 1460 keV and 2614 keV from the Th chain and the 1764 keV from the U chain with a relative contribution of 84%, 11% and 5% respectively after the rock wall was covered with the waterproof Urylon coating.

A total of all fluxes below 6 MeV is shown in table 6.1.

Energy (keV)	Flux ($cm^{-2}h^{-1}$)	error ($cm^{-2}h^{-1}$)
0-1000	345.6	34.6
1000-2000	476.7	47.7
2000-3000	60.1	6.0
3000-4000	1.6	.1
4000-5000	0.011	0.001
5000-6000	0.0026	0.0004

Table 6.1: Gamma ray flux in the SNO cavity.

A calculation of the number of γ rays that interact in the PMT glass is necessary in order to compare with the number that is expected in the PGT. To find the rate of γ ray interactions in the glass:

$$R = I\sigma nt$$

where R is the rate of γ rays interactions, I is the flux of γ rays incident on the glass, σ is the cross section of the molecules in the glass, in this case primarily SiO_2, n is the density of atoms and t is the thickness of glass. From table 6.1, the γ ray flux is 538.4 $cm^{-1}h^{-1}$ for 1 to 6 MeV. This does not include the flux of γ rays below 1 MeV since below 1 MeV the γ ray flux is peaked below 200 keV so most of the Compton electrons would be below the Cerenkov threshold. The total flux incident on the PMT with a 10 cm radius is

$$I = 538.4\, h^{-1}cm^{-2} \cdot 4 \cdot \pi \cdot (10cm)^2 = 188\, PMT^{-1}s^{-1}$$

The density of glass is 2.33 $g\ cm^{-3}$ and the mass of a SiO_2 molecule is $9.96 \cdot 10^{-23}g$ therefore the numbers of molecules is

$$n = \frac{2.33g\ cm^{-3}}{9.9610^{-23}g} = 2.34 \cdot 10^{22}cm^{-3}.$$

The cross sections [22] for Si and O are 2.417 barns/atom and 1.378 barns/atom respectively for 1.460 MeV γ rays therefore this gives a total cross section per molecule (and similar calculations for the other two main energies of γ rays) of

$$\sigma_{1.460} = 5.173\ barns/molecule$$
$$\sigma_{1.764} = 4.817\ barns/molecule$$
$$\sigma_{2.614} = 4.023\ barns/molecule.$$

with an approximate average cross section, taking into account the relative fluxes of the γ rays with different energies, of 4.902 barns/molecule.

The average thickness of the glass envelope is 3mm. This results in a total rate of γ rays Compton scattering in PMT glass of

$$R = 6.4\, PMT^{-1} s^{-1}.$$

By using the differential cross section in energy-dependent form [24] the expected energy spectrum for Compton electrons has been made and is displayed in figure 6.1. Compton spectra for the three main γ ray energies from the rock wall are shown along with the total spectrum which has taken into account the relative γ ray fluxes and cross sections for these γ rays on SiO_2. From this plot a mean electron energy of 793 keV with the electron energy peaked at around 1.25 MeV is expected.

Alpha Scintillations

Radon decay has been calculated to be the largest source of background during air-fill [29]. Due to the large amount of radon in the detector the background is expected to be dominated by α particles (from radon decay) scintillating in air. During air fill 3 $pCi\ l^{-1}$ of radon was measured between the PMT support structure and the acrylic vessel. Inside the vessel the concentration of radon was lower by about 1/3. This is because prior to this measurement radon rich mine air had been circulated within the PSUP while the air inside the AV volume had been relatively undisturbed allowing a significant portion of the radon to decay away. Radon decays with 3 α particles in quick succession which would have resulted in $6.55 \cdot 10^5$ α particles per second emitted by radon decay inside the PSUP, each of which is expected to emit

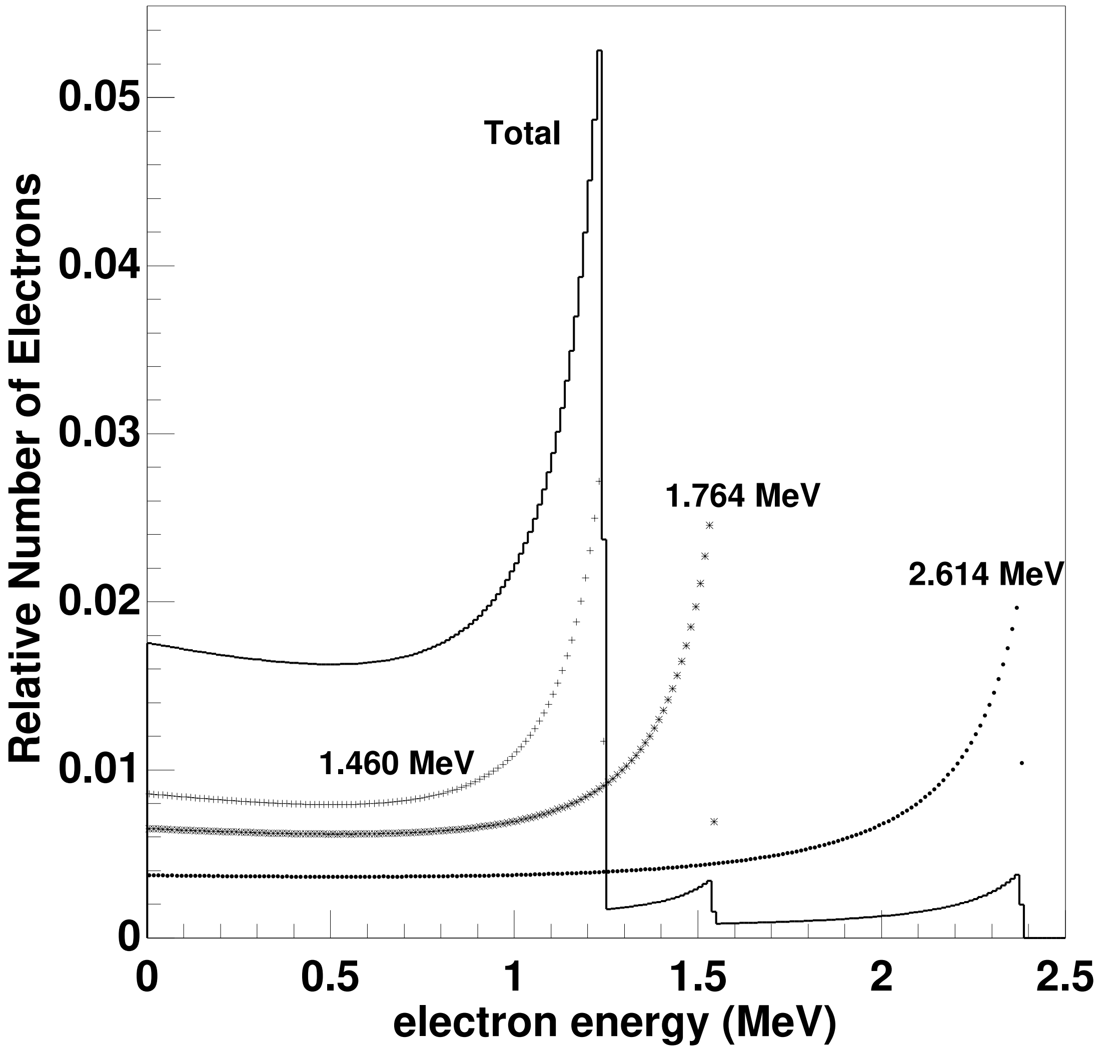

Figure 6.1: Spectra of electron kinetic energy from Compton scattering of 3 different incident γ ray energies. The total (thick line) is the electron energy from Compton scattering due to the main three γ ray energies with relative intensities in the SNO cavity and relative cross sections with SiO_2 taken into account.

an average of 230 photons α^{-1} from scintillation in air peaked at a wavelength of 350 nm [29].

One would expect that α particles scintillating in air near the PSUP may cause large pulse events in a single tube since multiple photons may be concentrated onto a single PMT. Using SNOMAN this possibility has been investigated by creating a Monte Carlo simulation of radon decay. The Monte Carlo consisted of a burst of 230 photons started at a point to simulate the alpha scintillating in air. This was done uniformly between the AV and the PSUP to simulate radon decay.

The results of this Monte Carlo are shown in figure 6.2 and are compared to a Monte Carlo of a single pe spectrum. It can be seen that the radon Monte Carlo follows the single pe spectrum very closely with no evidence that it would contribute multiple photons to the PGT spectrum. Therefore this source of background primarily contributes single photon pulses in the PMTs.

Dust

Another possible source of large pulse events is from mine dust deposited on the PMT glass. In this case it would not be expected to come from the γ rays from particle decays in dust producing Compton electrons in PMT glass since this contributes a negligible increase to the rock wall γ ray flux. However, as explained earlier, it is the high energy β that emits Cerenkov radiation near the photo-cathode that is predicted to be a source of the large pulse events in the Monte Carlo. So dust on the PMT glass may emit β particles which create large PMT pulses.

A measurement of dust on the PMT reflectors shows that there was 0.5 to 0.6 $\mu g\ cm^{-2}$ of mine dust. Assuming the same for PMT glass surface, there is approxi-

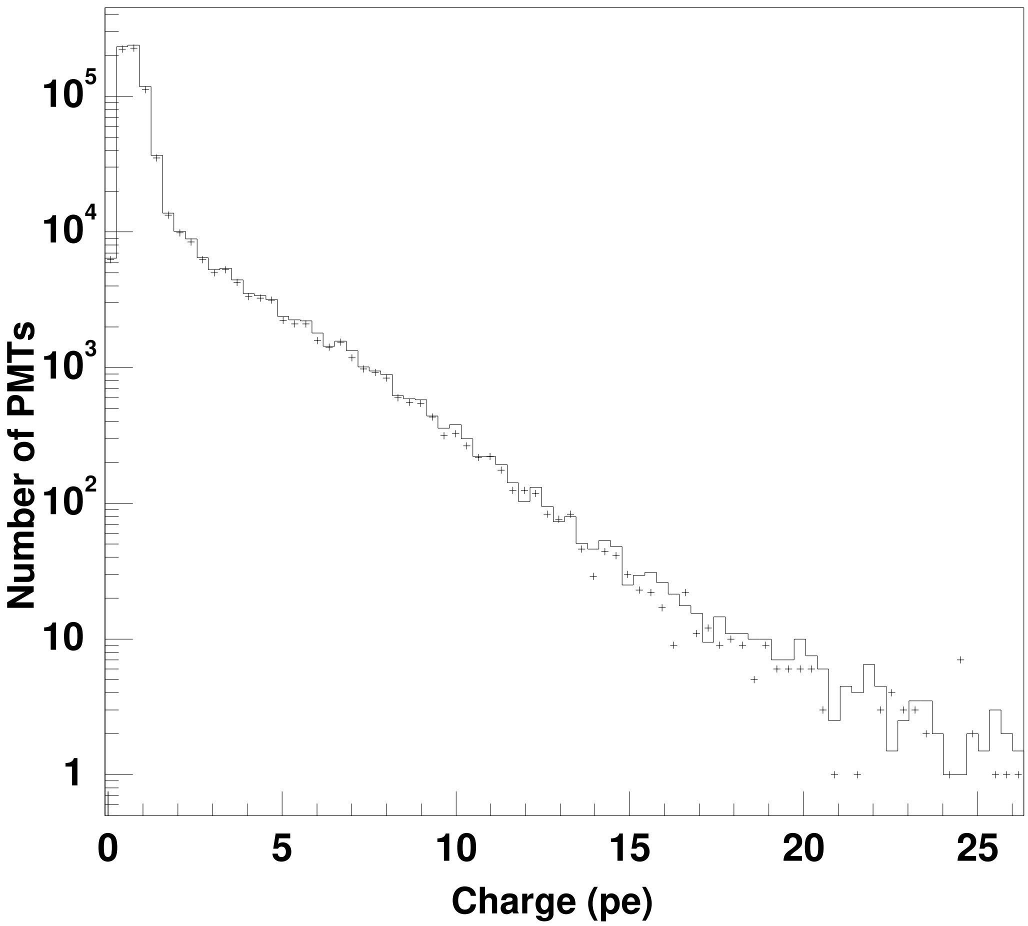

Figure 6.2: Monte Carlo of α particles between AV and PSUP (line), Monte Carlo of single photon spectrum (crosses) in air-fill.

mately 754 μg of mine dust per PMT. The concentrations of Th and U is, respectively, 3.3 and 1.2 μg per gram of mine dust [2]. Therefore there is approximately $3.4{\cdot}10^{-3}$ μg of uranium and thorium on the surface of each PMT. Comparing this to the 18 μg of U/Th expected to be in the glass envelope of each PMT, this is negligible.

6.3 Pulsed Global Trigger Events

PGT events from run 1029 taken on Aug 9, 1998 were analyzed. This included a total of 433094 PGT events or approximately of 0.165 s of integrated detector live time.

In figure 6.3 a direct comparison of the single photon PMT charge spectrum from laser-ball run 998 is made to the PGT spectrum from run 1029. The laser-ball spectrum was scaled so that the peaks matched and it can be seen that there are many more large PMT pulses in the PGT data than in the single photon data. This suggests that a larger portion of the PGT events create multiple photon hits in single PMTs.

Using the background rates calculated in section 6.2 the expected number of times a PMT fires from a single photon and particles which produce large pulses can be estimated. For the PGT run that was looked at there were 8500 PMTs on-line. Using this, and the fact that 0.165 s of detector time was analyzed, the total number of background events in the PGT can be estimated.

From the calculated rates, there are expected to be approximately 8750 electrons in the PMT glass from Compton scattered γ rays in this PGT sample. From decays inside the PMT glass 1930 βs from the U & Th chains and 92,6000 βs from the ^{40}K

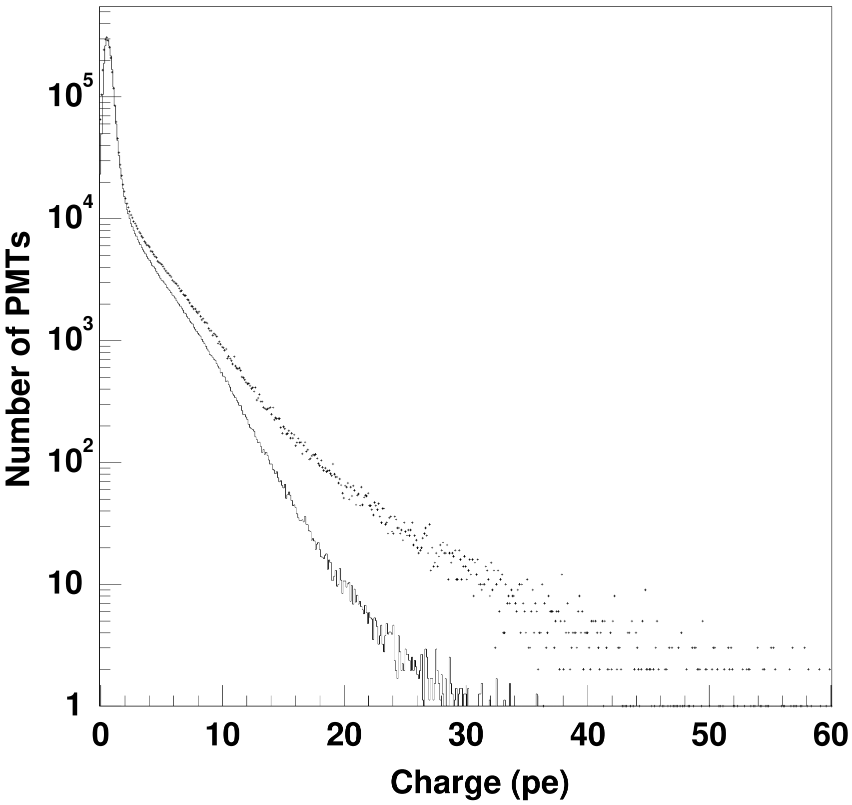

Figure 6.3: PMT Charge spectra of single photons (solid line) and PGT run 1029 (dots).

decays were emitted during the time period. This results in a total of 928000 βs with energy endpoints above 200 keV emitted inside the PMT glass.

The single photon events will have primarily been produced by radon decay in the air. A Monte Carlo simulation shows that photons have about a 7% chance of being detected by a PMT during air-fill. So for this data sample, one would expect approximately $1.72 \cdot 10^6$ single photons detected from radon decay.

Monte Carlo of PGT

All charge spectra presented here are histograms of the Qhl charge and are in the units of photoelectrons. The charge measurements for the data have been calibrated using the technique developed in chapter 5.

The PMT pulse height spectrum in the SNOMAN Monte Carlo was created using the PMT tests done at Queen's University, also discussed in the previous chapter. As was shown in figure 5.8 the spectrum from Queen's tests is significantly different from the single pe spectrum in the detector due to the relatively low cut off of the single pe tail in the test electronics. In order to do a direct comparison of Monte Carlo simulations to the charge spectrum of the SNO detector a realistic single photon spectrum must replace the current one. This is especially important since we are primarily interested in large pulse height events. The single photon spectrum from the laser-ball run 998 was used to make a new lookup table for SNOMAN simulations of the PMT pulse height. The resulting spectrum is compared to the single photon laser-ball charge spectrum in figure 6.4 as a double check that both SNOMAN and the lookup table now agree.

Using the new single pe spectrum in SNOMAN the different background sources

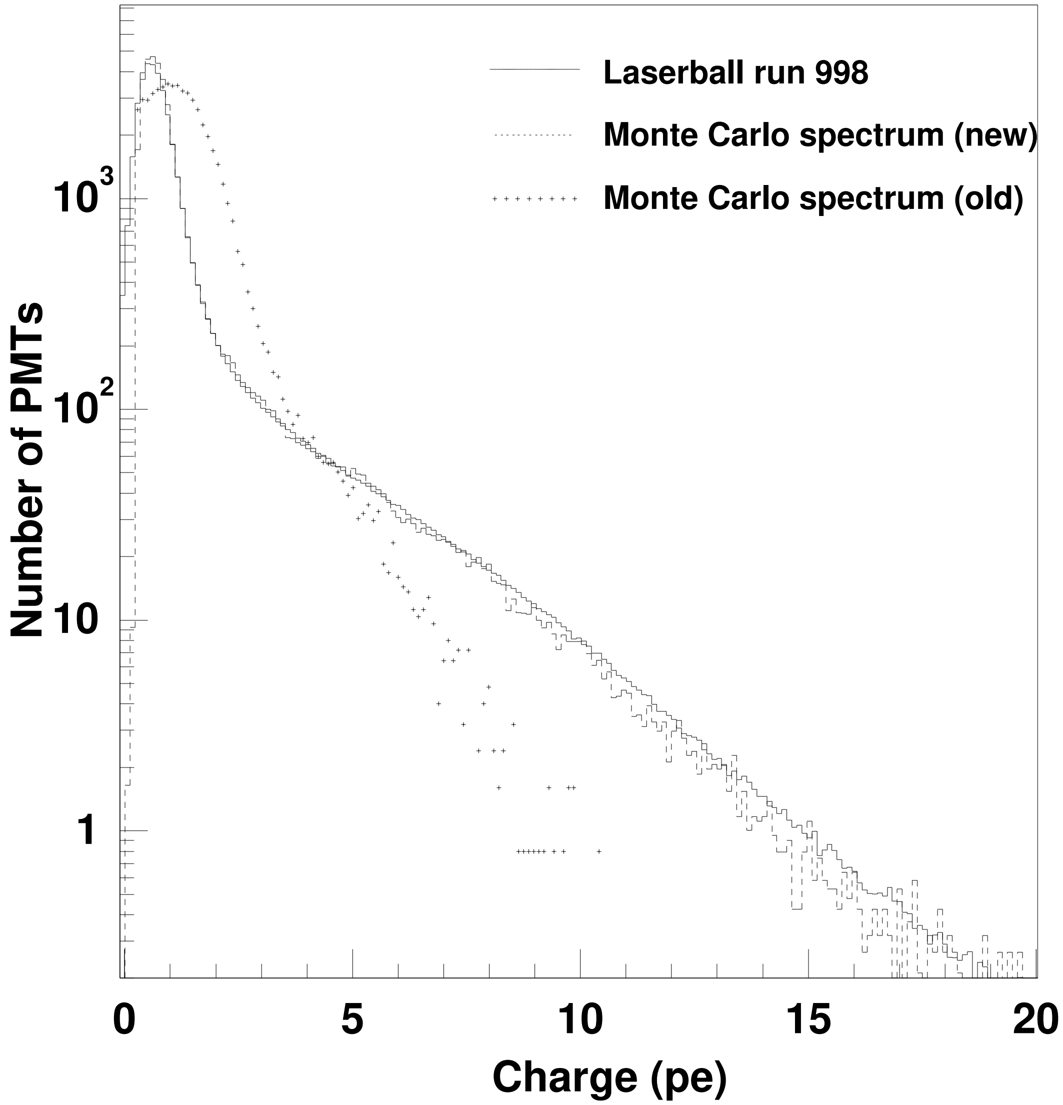

Figure 6.4: Comparison of a single photon laser-ball run pulse height spectrum to the old and the new SNOMAN Monte Carlo pulse height spectra.

expected in the PGT events were generated using Monte Carlo simulations. Single photon events were simulated by starting 1 million bursts of 10 photons emitted isotropically from the center of the detector to create a single photon spectrum with a negligible number of PMTs receiving multiple photons. One million ^{40}K β decays were started in a PMT glass envelope. To simulate the β particles produced from U & Th chains, 100,000 ^{208}Tl $\beta\gamma$ decays were started in a PMT glass envelope.

In order to simulate the Compton electrons several ranges of γ ray energy (1-2 MeV, 2-3 MeV, etc.) were simulated. For each range 10,000 electrons were started in the PMT glass envelope with a Gaussian energy range peaked at the midpoint for the range (i.e. 1.5 MeV electrons for 1-2 MeV γ ray range) with a sigma of 0.5. The spectra were then scaled relative to the flux reported in Table 6.1 and added together for γ rays from 1 to 6 MeV. This is an acceptable approximation since the ^{40}K βs will dominate Compton electrons by about two orders of magnitude. Once again the γ rays below 1 MeV were ignored since these γ rays peak at an energy well below 200 keV and we are only interested in electrons with enough energy to produce Cerenkov photons in glass, approximately 200 keV.

The total count for the 0.165s of live time is $1.71 \cdot 10^6$ single photons from α scintillations in air, 928000 βs from decays within the PMT, and 8750 electrons from Compton scattering. A Monte Carlo (solid line) with these numbers was created and is shown in the upper plot of figure 6.5 and compared to the PGT spectrum (dotted line). The lower plot shows the spectra of the 4 parts that make up the Monte Carlo of the PGT charge spectrum.

From these histograms it is apparent that there are events in the PGT data that create much larger pulses in the PMTs than the simulation. The first question is

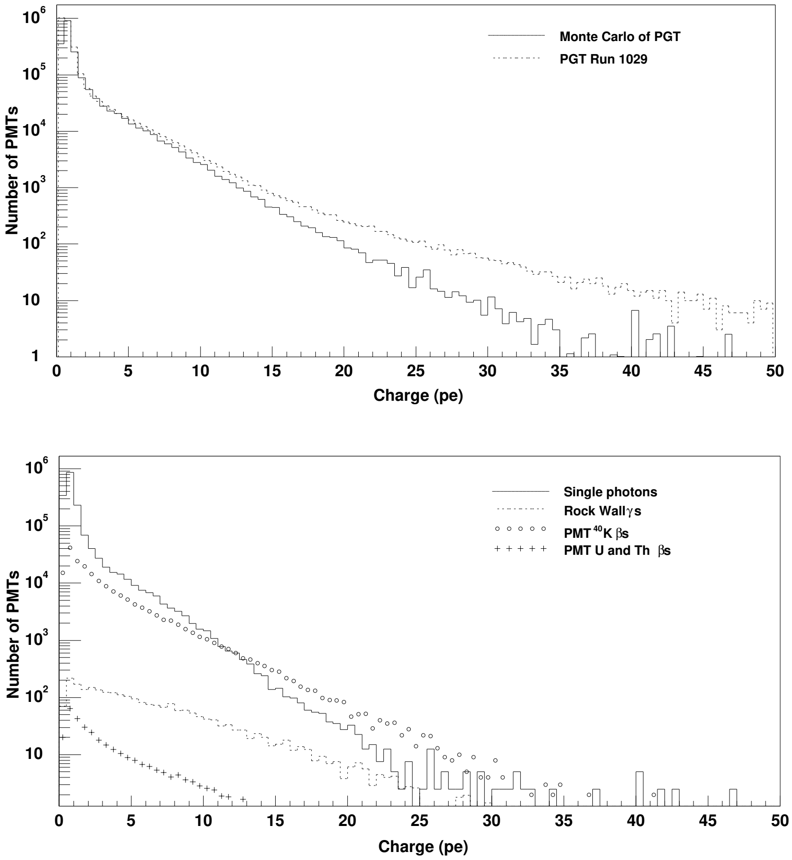

Figure 6.5: Observed and simulated charge spectra for PGT from run 1029. Lower plot displays the components of the Monte Carlo spectrum in the upper plot.

whether the background flux that produces large PMT pulses has been correctly estimated. However, it is not sufficient to just increase the number of Compton electrons or PMT βs in the Monte Carlo in order to explain the discrepancy. Doing this *will* allow the Monte Carlo spectrum above 20 pe or so to match the PGT spectrum, but the spectrum would then be distorted below 20 pe. Therefore one can not claim that this is merely a problem with incorrect background intensities.

The two probable reasons for this discrepancy are that there is an unaccounted background that produces large pulses in the PMTs or that the Compton electrons and β particles in PMT glass produce a larger pulse than the Monte Carlo simulations. If the pulses created by the charged particles in the glass are larger than expected the tail of the Monte Carlo would be much larger, matching the tail of the data.

Discussion of Monte Carlo of Charged Particles in Glass

To investigate the discrepancy found between the Monte Carlo of the PGT charge spectrum and the actual data we can start by looking at how the Monte Carlo handles charged particles in the PMT glass.

A Monte Carlo of 5000 electrons with 1 MeV of kinetic energy were started uniformly in a PMT glass envelope and the results are shown in figure 6.6. Of the 5000 electrons started, 2090 of these fired at least one PMT in the detector, and only those 2090 events are included in the analysis.

The upper left histogram shows the distance the electrons traveled while above the Cerenkov radiation production threshold, which has a mean distance of 0.19 cm. The number of Cerenkov photons created, displayed in the upper right histogram, has a mean value of 123 photons/electron.

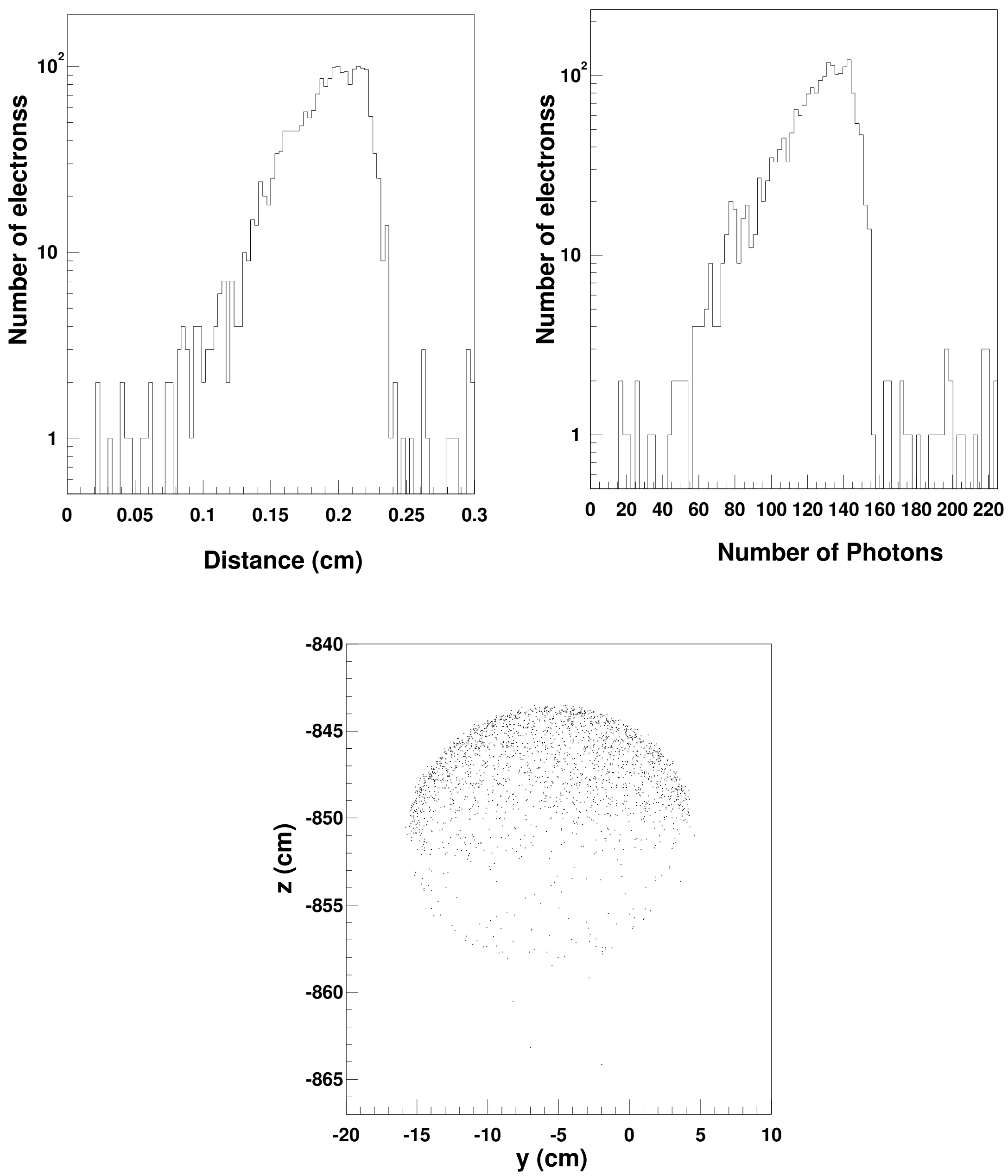

Figure 6.6: Results of Monte Carlo of 1 MeV electron in a PMT glass envelope. Upper left - distance electrons move while above Cerenkov threshold. Upper right - number of Cerenkov photons produced per electron. Lower plot - y vs. z cross section of PMT. Each dot indicates one bundle of Cerenkov photons created by the electrons.

The lower scatter plot in figure 6.6 is a y-z cross section of the PMT that displays a dot for each bundle of Cerenkov photons produced. From this one can make out quite clearly the PMT glass envelope as well as a few photons from interactions in the glass neck (below the envelope) and the PMT reflectors (above the envelope). It appears as if more Cerenkov photons are created on the upper hemisphere of the glass envelope. However an event has been included only if at least one photon strikes a photo-cathode in a PMT and produces a pulse above threshold. This is much more likely to occur if the electron is started in the upper hemisphere closer to the photo-cathode.

As a check of the Monte Carlo an estimate of the average number of Cerenkov photons created by a charged particle in glass can be made. The number of Cerenkov photons created by a charged particle [30] moving through a medium with index of refraction n (n=1.6 for glass), is

$$N = 2\pi\alpha l\left(\frac{1}{\lambda_2} - \frac{1}{\lambda_1}\right)sin^2\theta \qquad (6.1)$$

where α is the fine structure constant and l is the distance the charged particle travels while above the Cerenkov threshold. The values λ_1 and λ_2 are the wavelength limits of Cerenkov photon production, in the case of the SNOMAN Monte Carlo, $700 \cdot 10^{-7}$ cm and $200 \cdot 10^{-7}$ cm respectively. The value of θ is found by the index of refraction of the medium and the fraction of the speed of light that the electron is traveling ($\beta = v/c = .889$ for a 1 MeV electron):

$$\theta = cos^{-1}\left(\frac{1}{\beta n}\right). \tag{6.2}$$

From these values the expected number of Cerenkov photons created will be 134 photons/electron, slightly higher than the mean number 123 photons/electron produced in the Monte Carlo. This of course assumes that β is a constant. However β decreases as the particles moves through the matter losing kinetic energy to interactions. But this ideal case of a constant β gives a close approximation of the number of photons produced by the Monte Carlo simulation.

Therefore SNOMAN appears to be producing approximately the expected number of photons from Cerenkov radiation. However there are several explanations of why SNOMAN may be incorrectly simulating charged particles in PMT glass.

Tests of PMTs exposed to various types of radiation have been done [26] and were divided into two classes; those particles that were relativistic and those that were not. Alpha and β particles were exposed to the outer glass surface, neither of which had enough energy to penetrate all the way through the glass to the photocathode surface or create Cerenkov radiation. These sources produced less than 1 pe per incident particle, presumably through scintillations.

However charged particles with higher energies, such as cosmic rays or Compton electrons from ^{60}Co γ rays, create much larger pulses. Two processes were suggested to create these larger pulses. The particles were of relativistic energy so Cerenkov radiation could be emitted, therefore multiple photons may be detected creating a large pulse in the PMT, as has been discussed earlier. Also since these two types of radiation included charged particles that could interact near the inner surface of the glass, another possible method suggested was the production of δ rays. As a charged particle moves through matter energy is lost by interactions with electrons which create ion-electron pairs. These δ rays, or "knock-on electrons," are typically of energies less than 10 eV [27]. Since these electrons would be close to the energy of photo-electrons from the photo-cathode, any that are emitted from the inner surface of the glass may be focussed onto the dynode structure and can be detected as if it were a single pe from a photon.

Although charged particles in the SNOMAN Monte Carlo lose energy to these interactions, they are simply a method of energy loss as the particle moves through the medium and the actual δ rays are ignored. In the detector a charged particle passing near the inner surface of the PMT glass envelope may create δ rays that are detectable. This would not occur in SNOMAN since the only detection method is a photon interacting with the photo-cathode. In the Monte Carlo once the photon interacts with the photo-cathode there is a certain probability, dependent on the wavelength of the photon, that a pulse will be detected. So unlike in the actual detector, in the Monte Carlo δ rays would not be detectable.

The electron continues to creates δ rays as it passes through matter until its kinetic energy is below the work function of the electrons, a few eV. Unlike electrons that are only detectable if they are above the Cerenkov energy threshold, electrons of almost any energy may produce detectable δ rays, so low energy γ rays are able to contribute to the PMT background.

Not only is the production of δ rays a mode in which Compton electrons can produce detectable pulses, but the number of knock on electrons detected, and hence the PMT pulse height, may be very large. Electron ionization by incident electrons is precisely the process that a photo-electron goes through in the dynode chain. The yield rate (δ), the number of electrons emitted per incident electron, depends on the material. However there seems to be a significantly higher yield for charged particles incident onto insulators [28]. It has been reported that for graphite the maximum δ is 1.0 while for diamond, an insulating form of carbon, a δ of 84 was observed. It was also found that maximum δ yield occurred when the diamond was doped with a conductor, such as boron, to replenish the large number of electrons emitted (SNO PMT glass contains a total of about 7% B, 2% Al, and 2.8% K [23].) Therefore an insulator, such as the glass in the PMT envelope, may be a large source of knock-on electrons when exposed to energetic charged particles.

Another possible source of large pulse height events ignored until now is the photo-cathode. Decays in the photo-cathode may be responsible for some of the excess large pulse events in the PGT data. However the excess of events is approximately 54,000 events in 0.165 s of total detector time or an equivalent background of 39 Hz per PMT. Therefore there would need to be approximately 1 mg of U and Th and assuming the mass of the photo-cathode to be 30 mg this would mean the radioactivity of the photo-cathode would need to be approximately 3% or a factor of 10^6 times higher concentration than the glass. This is very unlikely and so can be dismissed as a significant source of these excess large PMT pulse events.

There exist several possible reasons why charged particles in the PMT glass may produce larger pulses than SNOMAN simulations. In order to verify this, the pulse height spectrum should be compared when one of the sources no longer contribute to the pulse height spectrum. This has been done using data after the detector had been filled with water, thereby shielding the PMTs from the rock wall γ rays.

6.4 Air Fill vs. Water Fill

After the light water had been filled in the detector, one of the sources of large pulses in the PMTs was shielded - Compton electrons from rock wall γ rays.

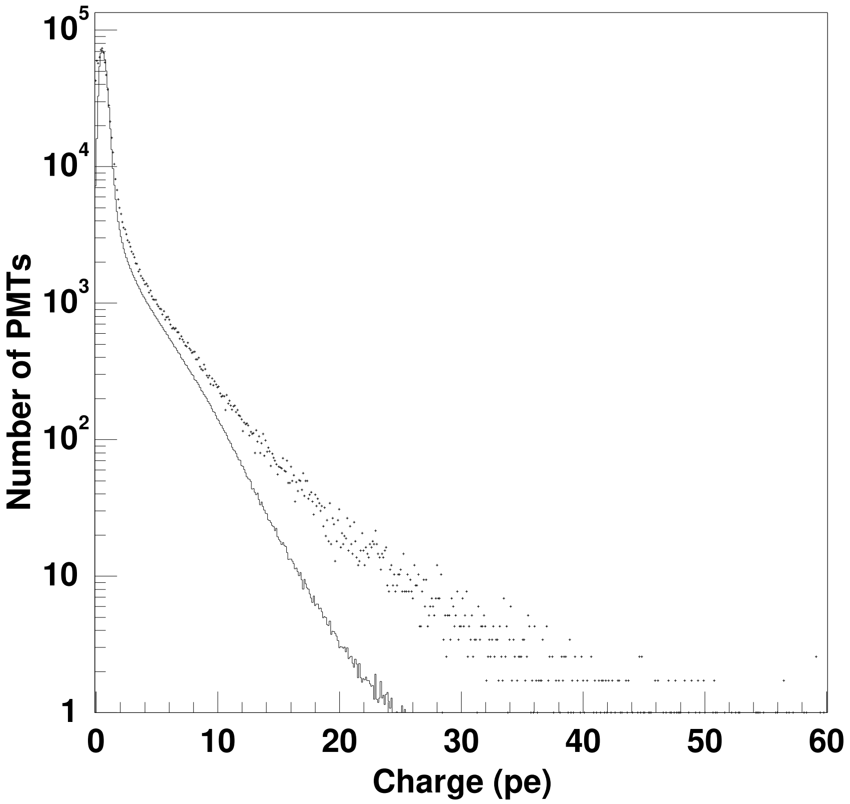

Figure 6.7: PMT Charge spectra of single photons (solid line) and PGT run 3564 (dots) after water-fill.

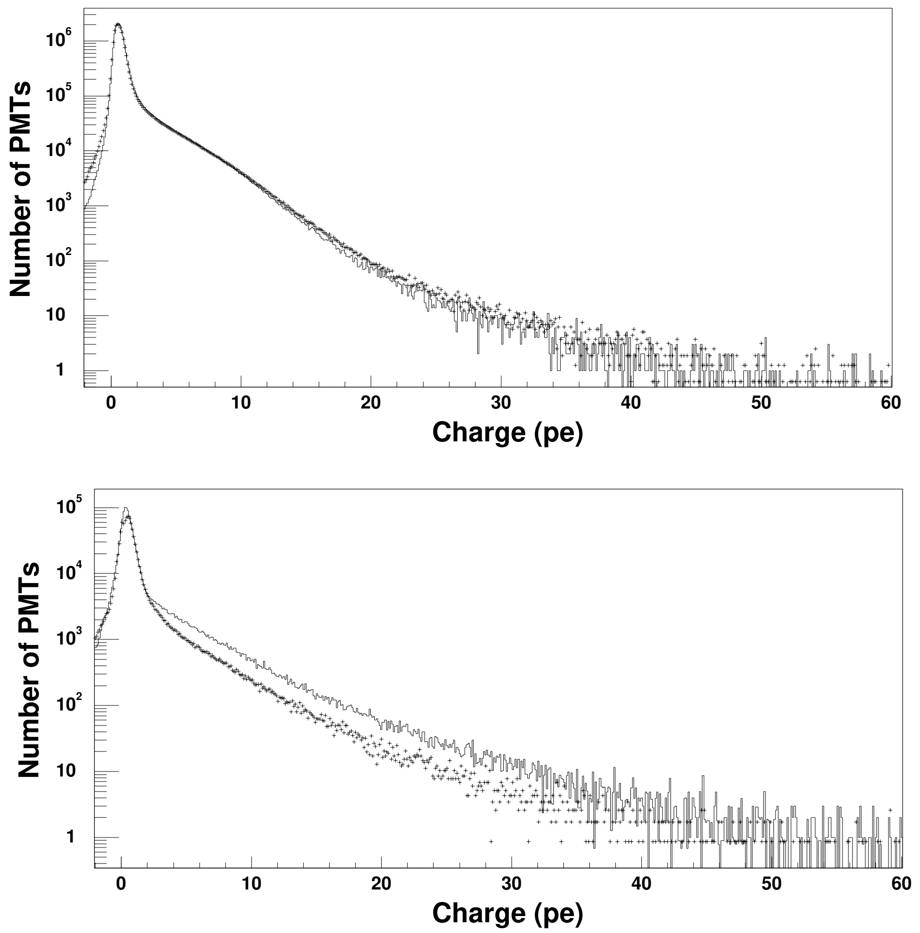

Figure 6.8: Comparison of Qhl charge spectra for air fill (solid line) and water fill (crosses). Top histograms compare the single photon laser spectra. The bottom spectra are PGT for air- and water-fill. The air-fill PGT spectrum has been corrected for α scintillations in air (see text).

Using laser-ball run 3467 for the single photon spectrum and the PGT from run 3564, figure 6.7 shows that there are still many more large PMT pulses in the PGT data than in the single photon spectrum. The charge spectra before and after the detector was filled were compared.

The histograms in figure 6.8 compare the Qhl charge spectra for air fill (solid line) and after water fill (crosses). The charge calibration for the water-fill data was done using laser-ball intensity runs taken after water-fill using the same technique as described in chapter 5.

The top histograms are laser-ball single photon runs taken in air- and water-fill. There is little difference in the two spectra. This indicates that the PMT characteristics, the electronics, and calibration method used are very stable, even in the very different environments of air- and water-fill and after numerous changes during the commissioning stage of the detector. Therefore a direct comparison of the PGT pulse height spectra for the two conditions is possible. The lower histograms compare the PGT in air fill discussed previously with the PGT from water-fill run 3564, taken on May 17, 1999. Both runs have the same number of PGT events and the PGT for water-fill has been scaled for having 9146 PMTs on-line (compared to 8500 during air-fill).

During water-fill there has been what is believed to be micro-breakdown events. These events occur in the PMT or connector and are best identified by adjacent PMT channels in the same card firing due to pickup from the large pulse. These breakdown events usually reoccur in the same tube at a high rate. One was found in the PGT data from crate 15, FEC 1. The charge spectrum of this type of event has been characterized and was not in the range of interest, mostly less than a single pe due to the pickup channels. So this micro-breakdown should not have any effect on the number of large PMT pulses in the PGT run.

Because of α scintillations in air-fill, the PGT taken during air-fill has many more single photon events than the water-fill data. The laser-ball single photon spectrum was scaled and subtracted from the air-fill data so that the single pe peaks of the two PGT runs match in order to remove this difference. The results of the two spectra are shown in the lower plots of figure 6.8. As expected there are fewer large PMT pulses in the water-fill data.

The difference in the number of events above 2 pe for the two spectra is about 60,000. If the difference in the spectra is due to the shielding of rock wall γ rays after water fill, the value can only be considered a lower approximation. This is because any information about the relative number of events that result in pulses below 2 pe has been removed from the spectra when the single pe spectrum was subtracted from the air-fill data so that the peaks matched. At this point it is unclear what fraction of the particles contributing to the large PMT pulses also contribute to the spectrum below 2 pe. However, even taking 60,000 as a lower limit, this is significantly higher than the expected number of Compton electrons from rock wall γ rays during the air fill run (calculated to be 8750). This suggests either that there were many more Compton electrons from the rock wall γ rays or that the water is now shielding another source of large PMT pulses.

However in the approximation of Compton electrons calculated, only those γ rays above 1 MeV which were expected to produce electrons that emit Cerenkov radiation where included. Almost all Compton electrons from any rock wall γ ray will create δ rays. The flux of rock wall γ rays below 1 MeV (from section 6.2) is 345.6 $cm^{-1}h^{-1}$

which are peaked well below 1 MeV. Approximating the mean to be about 200 keV, the cross section for Compton scattering is much larger, about 10 barns/atom which would result in a Compton scattering rate $R = 24.3\,PMT^{-1}s^{-1}$. So it is expected that in the PGT in air-fill there would be a total of 42800 electrons of any energy (0-6 MeV) from Compton scattering in the glass envelope.

This may account for some of the difference between air-fill and water-fill PGT spectra, but even if there was a 100% detection efficiency for these particles this does not account for all of the extra large pulse events. However, in glass electrons with low kinetic energy have a very short stopping range. As an example, take electrons with 200 keV of kinetic energy. The average range of these particles is about 0.2 mm or assuming they are evenly distributed in the glass envelope, 0.65% of these low energy electrons have enough energy to penetrate to the inner surface of the envelope where it is possible for δ rays to escape from the surface and be detected. So although it is possible for electrons below the Cerenkov threshold to be detected by the δ rays they create, this can not make up the difference in number of large pulses seen between air- and water-fill.

Finally, a Monte Carlo simulation of the water-fill PGT run similar to the air-fill simulation has been made. This time there were no Compton electrons from rock wall γ rays. Since the expected number of single photons (from background radiation and PMT noise) is unknown, the single photon spectrum was scaled and added to the Monte Carlo so that the single pe peak matched the PGT data. The results are shown in figure 6.9.

The spectrum is now dominated by ${}^{40}K$ β decays above 2 pe. But once again there is an excess of large PMT pulse events in the PGT data, above 15 pe. However,

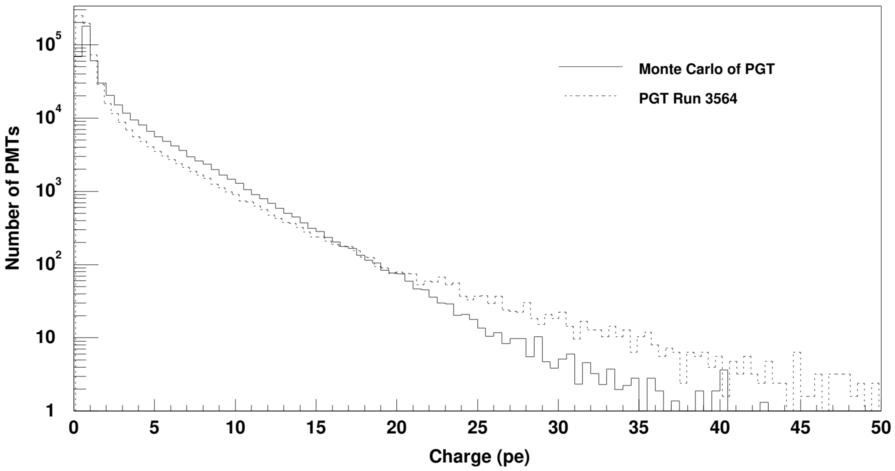

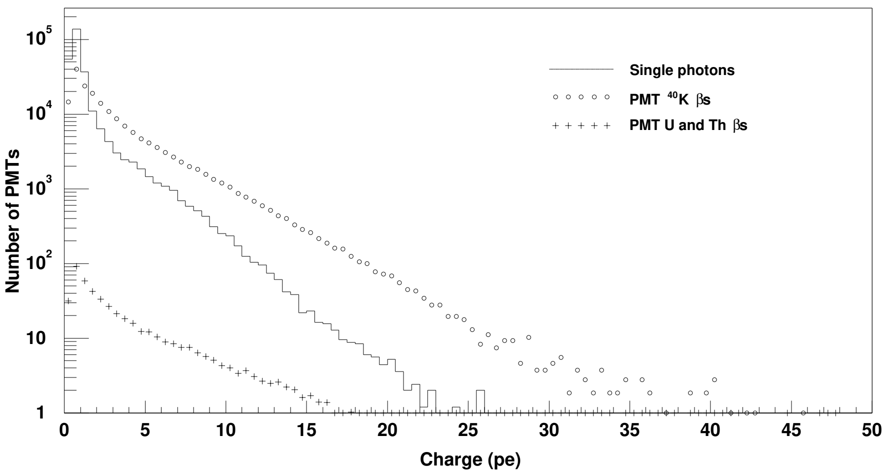

Figure 6.9: Observed and calculated charge spectra for run 3564. Lower plot displays the components of the Monte Carlo spectrum in the upper plot.

between 2 and 15 pe there is now an excess of events in the Monte Carlo simulation. Although this may only be a matter of an incorrect number of ^{40}K β decays creating an excess count between 2 and 15 pe, the discrepancy between the two spectra again suggests that the Monte Carlo may not be properly simulating the pulse height spectrum for charged particles in glass.

6.5 Summary

Two main results are found in this chapter. First it was discovered that the PGT has many more large PMT pulses than were expected. SNOMAN Monte Carlo simulations of the PGT show that the number of single photons from α scintillations in air match the data quite closely. However Monte Carlo simulations of large PMT pulse events, expected from relativistic charged particles in the PMT glass, were unable to reproduce the high charge tail of the PGT. Since increasing the number of this type of events in the Monte Carlo in order to compensate for the high charge discrepancies further distorts the charge spectrum, it is unlikely that this is merely a case of underestimating the known radiation backgrounds. Therefore it has been hypothesized that either the SNOMAN Monte Carlo is unable to properly simulate the results of this type of particle in the PMTs or another source of large PMT pulses has not been identified, or a combination of the two.

Also, light water shielding of the rock wall γ rays resulted in a decrease of the large pulses when comparing PGT in air-fill to water-fill. Although the Monte Carlo of this type of event suggests a maximum pulse height of about 15 pe or so for this run (see figure 6.5), the differences in the two spectra is evident up to at least 40 or

50 pe, suggesting a much larger pulse height from charged particles in glass.

Some of the difference between the two spectra can be attributed to attenuation of γ rays from the rock wall, but the much higher quantity of large PMT pulses in air-fill suggest that there may have been another source that has also been shielded by the water. There were about 60,000 more PMT pulses above 2 pe in the air-fill spectrum, while rock wall γ rays are calculated to contribute approximately 8750 events. Incidentally, the difference between the air-fill PGT pulse height spectrum and the Monte Carlo created to simulate the PGT also has a difference above 2 pe of about 52,000 events.

Finally a Monte Carlo simulation of the water-fill PGT was made and again there was an excess of large PMT pulse height events. However, now that the number of single photon events have decreased it is evident that there are too few PMT pulses between 2 and 15 pe in the PGT data compared to the Monte Carlo simulation.

Another source of large PMT pulses would explain the difference between the air- and water-fill spectra, as well as the difference between the two PGT and Monte Carlo spectra. But it is not evident where events that create such large pulses in the PMT would originate. nor why the source is attenuated, but not removed, after water-fill was completed.

7 Conclusion

7.1 Discussion of Results

In previous Monte Carlo analyses it has been shown that PMT $\beta\gamma$ decays may be identified by the large pulse created in the PMT by the β particle producing Cerenkov photons in close proximity to the photo-cathode. However in order to use this as an identification process the PMTs must have properly calibrated charge measurements.

In chapter 4 an analysis of current methods of charge calibration showed that there was a large discrepancy between the Qhl and Qhs charge measurements. On an event by event basis Qhs was larger than Qhl by a factor of 1.5 after calibration. This was the case of two separate sets of calibration codes. Each code used the same data to calibrate the PMTs with slightly different methods.

It is unclear at this time why this method produced calibration constants which resulted in such different charge spectra for the same PMT pulses, but the inconsistency appeared to have been introduced during the step where discrete amounts of charge are electronically injected onto the charge capacitor and the resulting measurements of charge values are recorded.

Since properly setting and using a cut on the amplitude of PMT pulse to identify

PMT $\beta\gamma$ decays relies heavily on the PMTs being correctly calibrated, an alternative charge measurement was proposed. In chapter 5 several laser-ball calibration runs of varying intensities were used to calibrate the PMT gains. Using Poisson statistics to calculate the mean number of photons received by each PMT and finding the average ADC count for each PMT, constants to calibrate from ADC to photo-electrons were found. Although this type of calibration method has its own systematics, such as shadows from the acrylic vessel ropes, it was able to produce much better agreement between the different types of charge measurements.

Finally, in chapter 6, an attempt was made to identify sources of large PMT pulses. The charge spectrum using the PGT data for a total detector live time of 0.165 s during air-fill was calibrated using the method from chapter 5. Several sources of PMT pulses were identified which included single photon pulses from α particles scintillating in air, large pulses from PMT β particles and Compton electrons from rock wall γ rays. These types of interactions were simulated using the SNOMAN Monte Carlo program and compared to data taken from the detector. It was found there was an excess of the number of pulses above a few pe (approximately 54,000) in the PGT data.

There were two possible explanations identified for the lack of large pulse events in the Monte Carlo simulations. The first is that there is an unaccounted source that produces large pulses in the PMTs. The second is that the pulses created by charged particles in the glass, the β particles and electrons, may be creating much larger pulses than the simulation. If this was true the large pulse tail of the Monte Carlo charge spectrum would be greater and would match the data. In the Monte Carlo large pulses are only created by multiple photons incident on the photo-cathode.

In a real PMT any electron can create or contribute to a pulse, including electrons created by the charged particles colliding with molecular electrons in the matter. These δ rays, which if close enough to the inner surface, may escape and be focused on the dynode structure as are photo-electrons. This, added to the pulse created by Cerenkov photons, may produce a much larger pulse than simulated in the Monte Carlo.

The final step was to compare the PGT spectrum with the same amount of detector live time after the detector was filled with water to the PGT spectrum in air-fill. Although the charge spectra between the two conditions for single photon events were very similar, there were many fewer large PMT pulses in the PGT after the detector was filled with water. After the single photon spectrum was subtracted from the air-fill PGT so that the single pe peak matched the water-fill PGT, above 2 pe there were approximately 60,000 more events in the air-fill. The only expected source of these events that was attenuated by the water came from the Compton scattering of rock wall γ rays, but this could account about 8750 electrons with enough energy to emit Cerenkov radiation. It was also found that there would have been as many as 42,800 electrons of any energy which could create large pulses by emitting δ rays from the inner surface of the PMT, but only a small fraction of these would be in range of the inner surface of the glass envelope in order to do so. So the air-fill PGT had an excess of at least 50,000 large PMT pulse events that could not be explained, or considering that the PGT had an integrated time of 0.165 s and 8500 PMTs on-line, and equivalent PMT background of 36 Hz.

7.2 Future Experiments

In order to help determine the source of these excess large PMT pulses in the PGT data it would be beneficial to recreate the conditions of air-fill as closely as possible. This could be done by making a test stand on the deck above the water to collect background PMT pulses. The rock wall radiation would be of the same energy spectrum and approximately the same flux. The PMT on the deck could be connected to a spare channel in the SNO electronics so that the electronics conditions are the same as those PMTs in the detector. Although this experiment would be limited to no more than a few PMTs, the PGT data was collected in a relatively short time, 8500 PMTs for 0.165 s of integrated detector time or an equivalent of about 23 minutes for a single PMT. Therefore the air-fill experiment could be reproduced in a relatively short period of time.

Although this would be a similar environment to the PMTs in the PSUP it would be impossible to exactly recreate the conditions before water-fill. There may be unknown conditions that affected the PGT pulse height. One possibility is static charge build-up in the PSUP. Although there is currently no evidence of this, it is possible that static build up on the ABS plastic of the PSUP or reflectors may have affected the PGT data and it is currently impossible to rule this out. If the excess of large PMT pulses are not observed in PMTs on the deck it would be evidence that the pulses originated from some unknown condition of being in the PSUP during air-fill. Also, other tests may be performed such as warming and cooling the PMTs to match the temperature difference before and after water-fill. These experiments may be able to produce evidence or rule out that being in the PSUP environment was the cause of the excess large PMT pulses.

The next step in looking for PMT $\beta\gamma$ decays is using the data to look for the pattern of PMTs expected from a β decay in glass. This would be a single PMT with a large charge and other PMTs triggering from light due to the γ ray. This has the advantage of being done using current detector data without having to change any of the detector configuration.

This experiment would have the disadvantage of the PMT being in the PSUP and therefore a difficulty of determining whether the PMT emitted the light or was one of many receiving light. The reconstruction algorithm has a much larger error for events further from the center of the detector. One way to improve the efficiency of fitting PMT $\beta\gamma$ decays would be to lower a PMT into the D_2O volume and use the signal from this PMT to create a global trigger. Only those events which emit light and reconstruct to the position of the source PMT would be identified as PMT $\beta\gamma$ events. This experiment could be repeated with the PMT at different heights and the results could be extrapolated to the distance of a PMT in the PSUP.

One of the main concerns of lowering calibration sources into the D_2O is the rate at which they introduce contaminants to the heavy water. Even a well cleaned device may leach U and Th rich materials into the water. This could be important since at a PMT $\beta\gamma$ rate of 0.36 Hz there would only be about 31,000 decays per day. Experiments of Schott glass used to make the PMTs found that leaching rates were 50 $ng\ d^{-1}\ cm^{-2}$ [32]. For a PMT this would mean about 62.8 $\mu g\ d^{-1}$ of glass or $1.89 \cdot 10^{-12}\ \ g\ d^{-1}$ of U and Th introduced into the heavy water. This is negligible when compared to the amount of U and Th expected in the heavy water, which is about 10^{-5} g.

This experiment would result in two determinations. The first would be the β spectrum of the source PMT. A charge spectrum would be produced and compared to a single photon spectrum which would identify a proper cut and efficiency for removing PMT $\beta\gamma$ decays from data. The second is determination of the energy resolution of the PMT $\beta\gamma$ decays. Using the PMT and the β particle as a trigger the response of the rest of the detector to the decay can be measured, both the energy response and fitter algorithm to determine what fraction of PMT $\beta\gamma$ decay events would reconstruct inside the D_2O volume.

Bibliography

[1] F. Reines & C.L. Cowan, Jr., "Detection of the Free Neutrino," Phys Rev, **92**, 830 (1953).

[2] SNO Collaboration, "Sudbury Neutrino Observatory Proposal", SNO-87-12 (1987).

[3] John N. Bahcall, "Solar Neutrinos: Where We Are, Where We Are Going," The Astrophysical Journal, **467**, 475-484 (1996)

[4] John N. Bahcall, "Neutrino Astrophysics," Cambridge University Press (1989).

[5] E. N. Adams, "Limits on mass of the neutrino, Physical Review D **37**, 2047 (1988).

[6] R.J. Ford, "SNO N_2 / Dye Laser System Manual," SNO-STR-96-056 (1996).

[7] K. Lande, et al., "Solar Neutino Observation with the Homestake ^{37}Cl Detector," AIP Conference Proceedings 243, 1122, AIP (1992).

[8] J.N. Abdurashitov, et al., "Results from SAGE (The Russion-American Gallium solar neutrino Experiment)," Phys Let B, **328**, 234 (1994).

[9] GALLEX Collaboration, "GALLEX solar neutrino observations: Results from GALLEX III," Phys Let B, **388**, 394 (1996).

[10] Y. Koshio, "Study of Solar Neutrinos at Super Kamiokande," University of Tokyo, 99, (1998).

[11] J.D. Jackson, "Classical Electrodynamics, 2nd Ed.," John Wiley & Sons, (1962).

[12] The SNO Collaboration, "The Sudbury Neutrino Observatory," to be submitted to NIM.

[13] J. Klein, et al., "The SNO Trigger System," SNO-STR-97-035.

[14] W.R. Nelson, et al., "The EGS4 code system," SLAC report 265 (1985).

[15] R. Brun & F. Rademakers, "ROOT - An Object Oriented Data Analysis Framework, Proceedings AIHENP'96 Workshop, Lausanne, Sep. 1996," Nucl. Inst. & Meth. in Phys. Res. A, **389**, 81-86, (1997).

[16] P. Skensved & B.C. Robertson, "Summary of Backgroundsin SNO," SNO-STR-94-13 (1994).

[17] R.Ford, "Calibration of SNO for the Detection of ^8B Neutrinos," PhD. Thesis, Queen's University, (1998).

[18] C.J.Jillings et al., "The photomultiplier tube testing facility for the Sudbury Neutrino Observatory," NIM A, **373**, 421-429, (1996).

[19] D.S. Haslip, "An Examination of PMT $\beta\gamma$ Background in the SNO Detector," Queen's University, (1996).

[20] M.C. Perillo Isaac et al., "Gamma-Ray Background Measurements in the SNO Laboratory," Elsevier Preprint, (1999).

[21] M.C. Perill Isaac et al., "High Energy Gamma-Rays measurements in the SNO Cavity," SNO-STR-97-009 (1997).

[22] J.H. Hubbell et al., "Pair, Triplet, and Total Atomic Cross Sections (and Mass Attenuation Coefficients) for 1 MeV-100 GeV Photons in Elements Z = 1 to 100", J. Phys. Chem. Ref. Data, **9**, 1023-1147, (1980).

[23] R.K. Heaton, "Neutron Shielding Calculations for SNO Detector," Queen's Unniversity, (1988).

[24] R.R. Roy & R.D. Reed, "Interactions of Photons and Leptons with Matter," Academic Press, (1968).

[25] W. Frati & R.G. Van de Water, "Experimental Observations of U/Th Decays in Glass," SNO-STR-96-063 (1996).

[26] R.L. Jerde, L.E. Peterson, & W. Stein, "Effects of High Energy Radiations on Noise Pulses from Photomultiplier Tubes," Rev. of Sc. Inst., **38** (1967), 1387-1395.

[27] H.S.W. Massey & E.H.S. Burhop, "Electronic and Ionic Impact Phenomena," Oxford University Press, (1952).

[28] A. Shih, et al., "Secondary electron emission from diamond surfaces," J. Appl. Phys., **82**, 1860, (1997).

[29] S.D. Biller, M.E. Moorhead, & D.L. Wark, "Addendum to: Simulations of SNO during Air or Partial Fill," SNO-STR-97-011-A (1997)

[30] J.V. Jelley, "Cerenkov Radiation & its Applications," Pergamon Press Inc., (1958).

[31] C.M Lederer & V.S. Shirley (editors), "Table of Isotopes," John Wiley & Sons, Inc., (1978).

[32] P. Trent, "Oxford work on leaching," SNO-STR-90-127, (1990).

Vita

Name: Edward Perry Korpach

Place and Year of Birth: Carrot River, Saskatchewan, 1974

Education: B.Sc. (Phys), University of Saskatchewan, 1992-1996

Experience: Research Assistant, Sudbury Neutrino Observatory, 1997-1999

Teaching Assistant, Queen's University, 1997-1999

Publications: The SNO Collaboration, "The Sudbury Neutrino Observatory," to be submitted to NIM.